University of Alberta

Lateral resolution in laser induced forward transfer

by

Qing Wang

A thesis submitted to the Faculty of Graduate Studies and Research
in partial fulfillment of the requirements for the degree of

Master of Science

Department of Electrical and Computer Engineering

Fall 2009
Edmonton, Alberta

Examining Committee

Dr. Ying Y. Tsui, Electrical and Computer Engineering

Dr. Robert Fedosejevs, Electrical and Computer Engineering

Dr. Alidad Amirfazli, Mechanical Engineering

Abstract

In this thesis the lateral resolution limits of the Laser Induced Forward Transfer (LIFT) technique are being investigated. LIFT is a laser direct write process with micron and below resolution and is suitable for modifying, repairing and prototyping micro-devices. Single laser pulses with wavelength of 800 nm and duration of 130 fs from a Ti:Sapphire laser system were focused onto a transparent donor substrate coated with thin film to transfer the thin film material in the form of micro-disks through a small air gap onto an acceptor substrate. In this thesis, donor glass substrate coated with 80nm continuous Cr film and also Cr disks array patterned by photolithography or e-beam lithography were used as targets. The ablation threshold and transfer threshold were determined experimentally and compared to results from two-temperature model (TTM) simulations and reasonably agreement was obtained. For the continuous film target, the size of the LIFT disks depend on the laser fluences and the smallest sizes of around 700 nm were obtained near the transfer threshold. For the pre-patterned disks array targets, initially 1.3μm Cr disks were fabricated on the donor substrates by photolithography. Small focused, larger defocused and large top-hat laser beams were used to transfer the pre-patterned Cr disks. The morphology of the transferred material and reliability of transfer were studied. It was found that the large top-hat beam gave the most reliable and high quality transfer results, resulting in mostly

intact LIFT disks on the acceptor substrate. To push the resolution limit further, 500nm Cr disks fabricated on the donor substrate by e-beam lithography were used. The successful transfer of these 500 nm Cr disks gives a positive indication that LIFT can potentially be extended further to the nano-scale regime (usually defined as having sub-100 nm resolution).

Acknowledgements

I would like to thank all the people that helped me over the years with regard to my education and research.

I would like to express my sincere appreciation to my supervisor, Dr. Ying Tsui for his guidance and valuable advice throughout my research and for his help and support over the course of this thesis.

I would especially like to thank Dr. Robert Fedosejevs for his kindness and continuous support during my study at this university.

I would like to thank all the colleagues in the Laser Plasma Group for their help and sharing the experience with me.

Thanks to Blair Harwood and Steve Drake for their assistance to help me solve the technique problems and thanks to Vincent Sauer for his help in solving problems in e-beam lithography.

Thanks to the staff in NanoFab for their training of nanofabrication, allowing me to prepare my samples by nanotechnology.

I would like to acknowledge the financial support from the Canadian Institute for Photonic Innovations (CIPI) and the Natural Sciences and Engineering Research Council of Canada (NSERC), and I am grateful to iCORE for providing a graduate scholarship.

Lastly, I would like to express my biggest gratitude to my parents for their support and understanding. Their love will always encourage me to go further on.

Contents

List of Tables

List of Figures

Chapter 1

Introduction

1.1 Introduction to Laser Induced Forward Transfer (LIFT)

In microelectronics industry, lithography is now the mature mass production technique to fabricate micro-nano structures. However, for many new applications which require only a few devices or require to modify or to repair existing devices, lithography may not be the best technique to be adopted. One way to rapid prototype new micro devices and to repair existing micro devices is to use computer aided design (CAD) technique with laser micro-processing.

Since the advent of laser system, a lot of attention has been paid to the interaction between laser pulse and materials. Laser direct-write (LDW) processes, which can modify, add and subtract materials for a wide variety of systems, have developed to be an important complement in the micro and nanofabrication area. According to Alberto Piqué's group, LDW processes are categorized in three main

classes [1]: laser direct-write subtraction (LDW-); laser direct-write modification (LDWM); and laser direct-write addition (LDW+). LDW-, the most common laser direct-write technique, applies the laser to react with materials directly, leading to the photochemical, photothermal, or photophysical ablation on the substrate. It can be used in laser cutting, drilling, etching and laser cleaning [2] as well. LDWM utilizes a moderate laser energy, which is not high enough to result in ablation, to cause a permanent structural or chemical change in the material. A typical application is the rewritable compact disc, whose phase is transited between crystalline and amorphous material [3] when illuminated by a diode laser. LDW+, using laser-induced process to add material onto a substrate, is a relatively new technique compared with the other two. One typical example is laser chemical vapor deposition (LCVD), utilizing pyrolytic or photolytic decomposition in liquids or gases to produce patterns on the substrate [4] [5]. By using this technique, Cr lines were deposited on the surface of BK7 glass as $Cr(CO)_6$ gas was decomposed by femtosecond laser [6]. However, due to its slow deposition rate, narrow choice of materials because of the need for an organometallic precursor, and operation requirement of vacuum environment, LCVD has limited applications mainly for repairing high value-added parts [7]. Laser induced forward transfer (LIFT) is another LDW+ process, in which a portion of thin film is transferred in the form of micro-dots from a transparent donor substrate onto an acceptor substrate nearby by pulsed lasers. This technique was first demonstrated by Bohandy et al. [8] to produce direct writing of

50-μm-wide Cu lines on Si and fused silica substrates by using single ns excimer laser pulses (193nm) under high vacuum (10^{-6} mbar). It was then demonstrated that this process can be carried out under atmospheric conditions without the requirement of vacuum by the same group in 1988 [9]. Compared with LCVD technique, LIFT is much simpler, without the need for vacuum system and chemical decomposition. It can be potentially applied in various areas requiring the addition of a certain material. Thus, a lot of effort has been put to make the progress with regard to the LIFT technique recently.

Figure 1-1 shows the typical LIFT process. A continuous thin film is first deposited onto a substrate which is transparent to the laser. The film is usually between a few ten's of nm and a few hundred's of nm thick and this coated substrate is called the ribbon or donor substrate. An acceptor substrate is placed underneath, in close proximity to the film on the donor substrate. The laser is focused onto the film through the donor substrate, causing formation of vapor at the interface. The force tears out a portion of the film causing it to eject from the donor substrate at high speed. The ejected film travels through the gap between the donor and acceptor substrates. It subsequently strikes and bonds with the acceptor substrate.

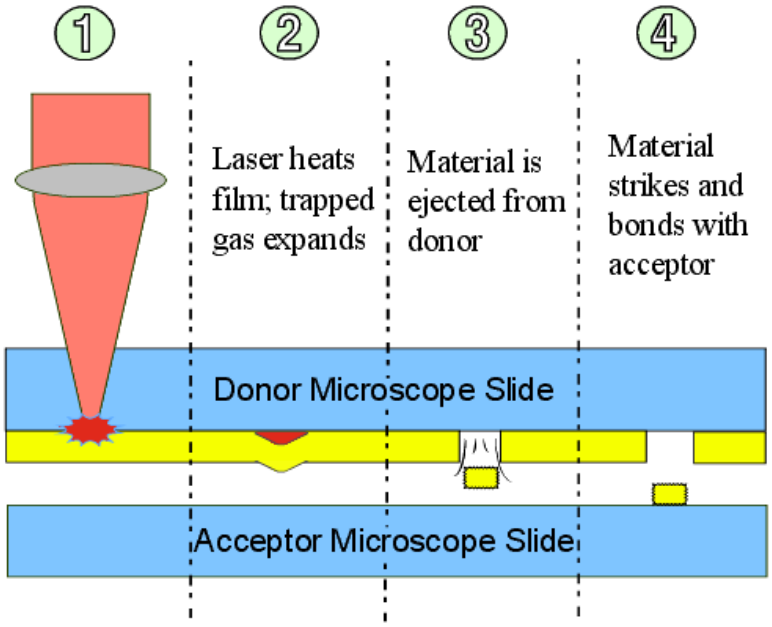

Figure 1-1 LIFT process with continuous film

Comparing with other laser-assisted deposition techniques producing small metal features involving either photolytic or pyrolytic decomposition of molecules in the gas, solid and liquid phases [10-15], the LIFT process has the advantage of no dependence on the vacuum operational environment, and the elimination of contamination problems caused by the organometallic precursors [8]. Because of the cleanliness and programmability, the LIFT process is ideal for the applications in prototyping and custom device fabrication, as well as in the modification and repair of existing devices or surfaces whose topography or chemistry make traditional micro-patterning techniques difficult. When LIFT is combined with laser micromachining, the combined technique can be used to add material or remove it from micro-devices as needed.

1.2 Review on the progress of the development of LIFT

Since the LIFT process was first proposed in 1986, a variety of metals have been demonstrated to be transferable by LIFT, including Al [16], Au [17-19], W [20][21], Cr [22], Cu [8] and Ag [9][23]. Other inorganic and organic materials such as In_2O_3 [22], Al_2O_3 [24], high temperature superconductors (YBCO and BiSrCaCuO) [25], peptides [26], proteins [27], living cells [28] [29] and even lambda phage DNA microarrays [30] were reported to be transferred by LIFT. In early days, the metal material transferred from a continuous film by LIFT had several shortcomings, such as poor film quality due to the energy deposition leading to crack and debris around the transferred spot, and oxidation of metal and delamination of the transferred layers because of the melting and solidification during transfer process. Various methods have been developed to attempt to overcome these shortcomings.

One method is to use ultrashort sub-picosecond laser pulses instead of the longer nanosecond laser pulses used in the LIFT process earlier [22] [31-33]. Since the pulse duration of a nanosecond laser pulse is much longer than the lattice heating time and electron cooling time, the energy will diffuse over the whole film thickness to gradually increase its temperature, leading to melting and other thermo problems. The ultrashort femtosecond laser pulse, however, allows the energy to be locked in the electrons without much of the electron-ion (lattice) energy transfer during the pulse duration [34] [35], because the pulse duration is less than the electron-ion (lattice) energy exchange time and heat conduction time

[36], the heat-affected zone is consequently reduced. Besides, the ejected Cr material by an ultrashort 500fs laser pulse is highly forward directed, with a narrow angle divergence on the order of 3º, while the ejected material from a 30 nanosecond laser pulse has a hemispherical shape, with a high divergence on the order of 50º [33]. Both the remelting reduction and narrow angular divergence allow ultrashort laser to better control the structure and contour of the transferred metal materials.

Besides adopting femtosecond laser, improvements have been made with regard to the target material. Employing multilayered films into LIFT was first applied by Tolbert, called laser ablation transfer [37]. In this method, a thin intermediate layer consisting of laser absorption materials is first deposited on the transparent donor substrate. The target material which is going to be transferred is then deposited on top of this laser absorption material. During LIFT process, the incident laser pulse interacts with the absorption layer, resulting in vaporization, which will then force the target material that is in contact with the absorption layer to be removed and transferred towards the acceptor substrate. This approach will reduce the damage of the target material since laser energy mainly reacts with the intermediate layer and makes the transfer of materials that would otherwise not absorbed the laser radiation possible. By using this approach, phosphor powders (Y_2O_3:Eu and Zn_2SiO_4:Mn) [38], biomolecule miroarrays [39-41], peptides [26], proteins [27] and living cells [28] were successfully transferred with application of either Au or Ti as the absorption layer (several tens of nanometers thick).

Triazene polymer [29], instead of conventional metal materials, was also used as the absorption layer and it is found that it can reduce the incident fluence required for transfer by 50%.

A. Piqué's group in Naval Research Laboratory proposed a new approach, MAPLE DW (matrix-assisted pulsed laser evaporation direct write), combining the advantages of both laser-induced forward transfer (LIFT) and matrix-assisted pulsed laser evaporation (MAPLE) [42]. This approach employs the mixture of soluble material to be deposited and a solvent phase which is usually pre-cooled to low temperature as the target material on donor substrate. When the target is irradiated by laser pulse, the solvent is rapidly vaporized and pumped away, propelling the solute toward to the acceptor substrate to form a highly uniform thin film with minimal decomposition. This approach has been applied to transfer metals, ceramics and polymeric materials such as Ag, Au, BaTiO3 and BTO [43] [44]. Various types of physical and chemical sensor devices and microbatteries were also prototyped by this approach [45].

More recently, an approach named Laser Decal Transfer was proposed by the same A. Piqué's group [46]. This approach uses viscous nanoparticle suspensions (Ag in their case) as inks for the target material. It was found that the viscosity of the suspension plays an important role in the ability to perform the decal transfers. When the viscosity was low (<100 cP), the transferred material showed a high degree of spattering with significant surrounding debris. However, when high viscosity (≈100,000 cP) was applied, the breakup of the transferred material was

prevented. Patterns with sharp shapes but no debris, while maintaining excellent conductivity and adhesion were achieved on the acceptor substrate. By using this technique, 5 μm wide and several hundred nm thick lines with very nice contour profiles were fabricated [47].

By using the LIFT technique, various applications have been realized, in addition to directly transferring metal and other inorganic and organic materials, complicated patterns can be printed to substrates by building up LIFT micro-dots by moving the acceptor substrate with a computer controlled translation stage. For example LIFT has been used to print holographic diffraction patterns on glass [22] and to print electrodes for microfluidic devices [19]. Sensors, microbatteries, interconnects, antenna and solar cells were also fabricated by LIFT [45] [48-50]. By combining the LIFT technique with other laser direct writing techniques such as laser micromachining, even embedded electronic devices and circuits were reported to be fabricated [51] [52].

Several groups have investigated the dynamics of the LIFT technique. Lift off film's velocity up to 0.75 Mach was reported by Lee et al. [53] by using time resolved optical microscopy and a Nd:YAG laser (1.064 μm, 250 ns). Young et al. [54] also applied ultrafast microscopy and a 355nm frequency-tripled Nd:YAG laser (150 ns pulse width) and a 500nm N_2/dye strobe laser (600 ps pulse width) to measure the ejected plume velocity from barium-zirconium titanate/α-terpineol layer, which was reported to be 0.2 km/s. The dynamic behavior of the gold atoms and emissive particles by LIFT were investigated by the microscopic

two-dimensional laser induced fluorescence (2D-LIF), reported by Nakata and Okada (dye transfer laser 440nm, 9 ns) [55]. According to the schlieren imaging measurement by I. Zergioti et al. [33], the velocity of ejected Cr material by a hybrid distributed feedback dye laser/KrF excimer laser (248 nm, 500 fs) was 460±6 m/s and the velocity by a KrF excimer laser (248 nm, 30 ns) was ~350m/s.

Typically, the spatial resolution of the conventional LIFT is several microns or more. Recently, a minimum achievable spatial resolution of transferred Cr material around 330nm was reported by using Ti:sapphire laser (800 nm, 110 fs) pulses [56]. In that study, the film on the donor substrate was very thin (30 nm) so that the laser would melt all the way through the thickness of the film and cause a molten Cr droplet to deposit on the acceptor substrate.

1.3 LIFT using donor substrate with pre-patterned Cr micro-disks

The resolution of the LIFT process depends on the size of the dots that can be transferred. Typically the disk shaped LIFT dots have diameters from several μm to few tens of μm, depending on the laser fluences. The size of a LIFT dot is often difficult to control because the fluctuation in laser energy and the spatial non-uniformity of target film can lead to size variation of the LIFT dot. In addition debris is often results as the material are being tore apart from the target film during the LIFT process. In order to extend the conventional LIFT to produce

smaller micro-dots and to improve the size uniformity of the transferred dots, as shown in Figure 1.2, small material dots patterned on a transparent substrate using lithography process are used as the donor substrate. The pulsed lasers are then focused on top of these pre-patterned dots and transfer them onto the acceptor substrate. Since these small dots are isolated from each other, unlike the conventional LIFT process, they will not be affected by the surrounding material. The size of the transferred dot is thus expected to be similar to the one on the donor substrate and the quality of the transferred material is expected be improved too, with less debris around it compared to the one transferred from traditional continuous film.

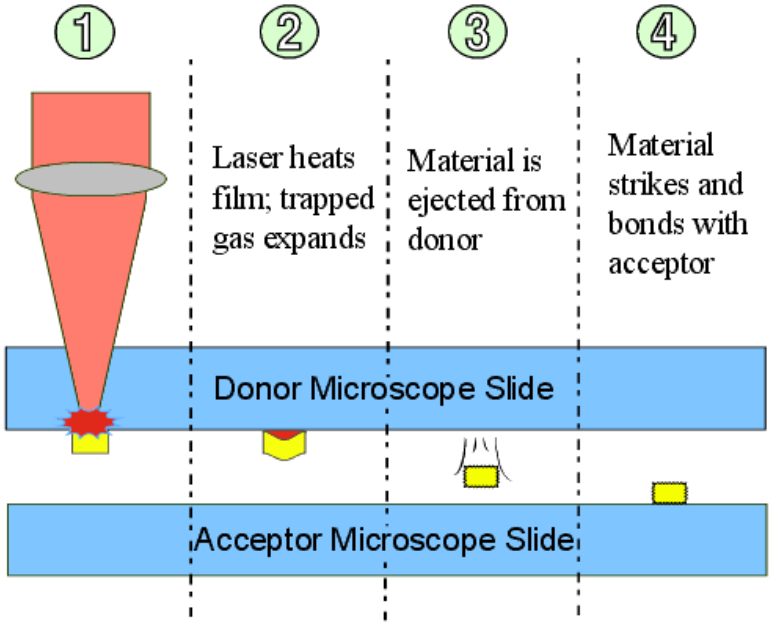

Figure 1-2 LIFT process with patterned donor substrate

1.4 Outline of this thesis

This thesis is divided into five chapters. Chapter 1 is Introduction, with brief description of LIFT process and literature review of the progress of LIFT. Chapter 2 is Experiment Setup and Experiment Methods, discussing the laser system used in experiment, the LIFT setup and experimental techniques with regard to laser alignment, pulse fluence measurement, morphology measurement and so on. Chapter 3 is Sample Preparation, describing how the pre-patterned donor substrate was fabricated by photolithography and e-beam lithography. Chapter 4 is results and discussion, and the last chapter is conclusion and future work.

Chapter 2

Experiment setup and experiment methods

2.1 Laser system and target material

2.1.1 Laser system

Since the Laser Induced Forward Transfer (LIFT) process was first proposed by Bohandy et al. [8] in 1986, nanosecond laser pulses have been widely used as the light source. Although the LIFT process can be completed successfully, the quality of the transferred dot on the acceptor substrate and the resolution were limited. Usually there was significant debris around the transferred dot. When ultrashort sub-picosecond laser systems became available, they were adopted as light system sources for LIFT. The advantages of ultrashort pulse lasers over traditional nanosecond pulse lasers include: (a) the creation of vapor and plasma phases occurs after the ultrashort laser pulse has ended and thus there are no interactions between the ultrashort laser pulse and the vapor/plasma; (b) the

illuminated material has negligible heat-affected zones, therefore precise structures and contours can be achieved; (c) the damage threshold of long pulse lasers (longer than hundreds picoseconds) was found to be strongly dependent on the pulse duration τ with a scaling of $\tau^{1/2}$ [57], while that of ultrashort pulse laser was observed to be pulse-duration independent [58] and (d) the ejected material from a femtosecond laser pulse is highly forward directed, with a narrower angular divergence compared with the nanosecond laser pulse. As a result, the quality of the transferred material is improved and the resolution is decreased. By using femtosecond lasers, dots under 1μm were successfully transferred from a 30nm thin Cr film onto a silicon wafer [56] [59]. In our experiment, 130fs, 800nm Ti:Sapphire laser was chosen as the light source to conduct the LIFT process. Details of the laser system will be discussed in the following sections. Since LIFT is basically a laser matter interaction process, the fundamental mechanism will be discussed first.

2.1.1.1 Laser pulse interaction with metals

The laser heating mechanisms are slightly different when laser interacts with different materials, such as semiconductors, dielectric materials and metals. Nonlinear process such as multiphoton and tunneling absorptions will happen when a high intensity ultrashort laser pulse interacts with transparent materials, leading to the energy absorption by free electrons generated from the nonlinear

processes. It is then followed by energy transfer to the lattice afterwards.

When a laser pulse irradiates a metal surface, the energy transmission happens within 4 steps. First, the energy is absorbed by conduction electrons, due to the inverse Bremsstrahlung. Then because of the collision between electrons and ions, thermalization within the electron subsystem will happen. After that, the energy will be transferred to the lattice. Finally, the energy dissipates due to the electron heat transport into the target.

1) Inverse Bremsstrahlung [60]

When a conduction electron interacts with the electric field of the laser, it will simply wiggle and when the conduction electron collides with the bound electrons and the lattice, the material will absorb laser energy through dephasing. This is called Joule heating process, also known as inverse Bremsstrahlung.

2) Energy transfer process

There are two parameters playing an important role in energy transfer process during the laser metal interaction. The first is the absorption or penetration skin depth $l_s = 1/\alpha$, where α is the absorption coefficient, which is determined by the material itself. The other one is the heat diffusion depth $l_d = \sqrt{D\tau_l}$ [60], where D is the heat diffusion coefficient and τ_l is the laser pulse width. l_d indicates the heat penetration depth due to thermal conduction.

For long pulse, the heat diffusion depth l_d is larger than the penetration skin depth l_s. The temperature is determined by the heat diffusion length, which is changing as a function of pulse duration. Since the pulse duration is larger than the

electron cooling time, the whole energy transfer process, that is, energy transfer from photons to electrons and then to lattices, will be completed within the laser pulse. When the temperature reaches the melting point, as a result of the energy deposition, the ablation and material removal will happen through the melt expulsion which is driven by the vapor pressure and the recoil of the light pressure. Since the metal conductivity is large, the temperature can be transferred to the ambient materials around the ablation patterns, which cause damage and irregular shapes.

For femtosecond pulses, the heat diffusion depth l_d is smaller than the penetration skin depth l_s. The deposited laser energy is limited in a layer with thickness l_s. In this case, the pulse duration is far less than the lattice heating time. Thus the high energy is "locked" in the electrons and the electron-lattice energy transfer will not happen during the pulse duration. The localized energy heats material quickly past the liquid phase to the vapor phase and the material is removed away from the surface directly by vaporization. Since most of the energy is taken away by the vaporization, the heat diffusion to material outside the laser heated zone is small.

3) Two-temperature equation

Two-temperature model (TTM) is commonly used to model the heat transfer inside a metal heated by a laser pulse with duration less than a picosecond. On a femtosecond time scale, the energy absorbed by the electron will not be

completely transferred to the lattice. Thus, it is not an electron-lattice equilibrium system. The electrons and lattice subsystems are considered separately in TTM. By using the expressions for the temperature of electron and ion, T_e and T_i, the two-temperature equation can be expressed as [61]

$$C_e \frac{\partial T_e}{\partial t} = -\frac{\partial Q(z)}{\partial z} - g(T_e - T_i) + S \qquad 2\text{-}1$$

$$C_i \frac{\partial T_i}{\partial t} = g(T_e - T_i) \qquad 2\text{-}2$$

$$Q(z) = -\kappa_e \partial T_e / \partial z \quad , \quad S = I(t) A\alpha \exp(-\alpha z) \qquad 2\text{-}3$$

where z is the direction perpendicular to the target surface, $Q(z)$ is the heat flux, I is the laser intensity, $A=1-R$ and α are the surface absorptance and the material absorption coefficient respectively, C_e and C_i are the heat capacities of the electron and lattice subsystems, T_e and T_i are the electron temperature and lattice temperature respectively, g is the parameter characterizing the electron-lattice coupling, κ_e is the electron thermal conductivity.

Initially, Drude's free electron model was proposed to a present the free electron capacity C_e, by assuming that the electron velocities follow the Maxwell-Boltzmann distribution. Sommerfeld, later on, corrected the model by using Fermi-Dirac distribution instead, giving [62]

$$C_e = \left(\frac{\partial u}{\partial T}\right) = \frac{\pi^2}{2} n k_B \frac{T_e}{T_F} = \gamma T_e \qquad 2\text{-}4$$

where γ (J/[m^{3}k^2]) is the constant of electron heat capacity.

The Sommerfeld's model also gave an expression for the electron thermal conductivity κ_e. By using eqn. 2-4, a simplified equation can be presented as

$$\kappa_e = \kappa_0 \frac{T_e}{T_i} \qquad 2\text{-}5$$

where κ_0 is the conventional equilibrium thermal conductivity of a metal.

A more general expression for the electron thermal conductivity κ_e was given by Anisimov [63]:

$$\kappa_e = \chi \frac{\left(\theta_e^2 + 0.16\right)^{5/4}\left(\theta_e^2 + 0.44\right)\theta_e}{\left(\theta_e^2 + 0.092\right)^{1/2}\left(\theta_e^2 + \eta\theta_L\right)} \qquad 2\text{-}6$$

where $\theta_e = T_e / T_F$ and $\theta_L = T_i / T_F$. T_e, T_i and T_F are electron temperature, lattice temperature and Fermi temperature respectively. χ and η are material parameters that can be extracted from low temperature expression of electronic heat conductivity.

By applying different boundary conditions, problems associated with laser ablation can be modeled using equation 2-1 to 2-3. According to the heat transfer process, three characteristic time scales can be obtained, which are τ_e, τ_i, and τ_L. $\tau_e = C_e / g$ stands for the electron cooling time, $\tau_i = C_i / g$ stands for the lattice heating time and τ_L is the duration of the laser pulse. Based on the time scale, the laser-metal interaction can be divided into three regimes:

a). Femtosecond time scale. In this scale, the laser pulse duration is shorter than the electron cooling time, $\tau_L < \tau_e$. As a result, the electron-lattice coupling can be neglected, as described previously. The ablation can be considered as a direct solid-vapor transition which allows very precise micro-structure fabrication to be realized.

b). Picosecond time scale. In this scale, the laser pulse duration is larger than

the electron cooling time but smaller than the lattice heating time, $\tau_e < \tau_L < \tau_i$. When the laser ablation takes place, the electron heat conduction and formation of a melted zone inside the target also happen at the same time. The ablation on the surface can also be considered as a direct solid-vapor transition. However, inside the target, the liquid phase will present and reduce the precision of laser processing.

c). Nanosecond time scale. In this scale, the laser pulse duration is larger than the lattice heating time and also the electron cooling time, $\tau_i < \tau_L$. Because the pulse duration is long enough for the thermal wave to propagate into the target, a relatively large amount of material will be melted. Thus the evaporation occurs from the liquid metal, which will also reduce the fabrication precision.

In the LIFT process, the donor-film interface is melted and ablated by laser pulses (Figure 2-1), leading to a forward force to propel a section of material to the acceptor substrate. By using ultrashort laser pulses, the ablated material is confined to the laser heating zone, without heating and causing expansion of ambient material, as longer laser pulses would do. As a result, smaller and more precise transferred patterns can be achieved.

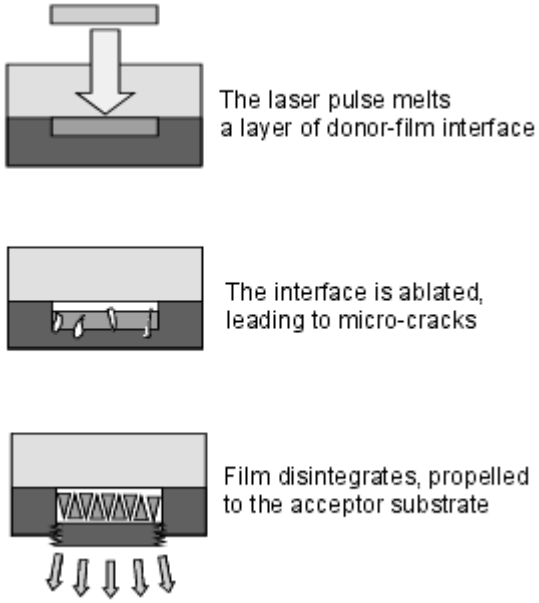

Figure 2-1 Donor-film interface ablation caused by laser pulses

2.1.1.2 Hurricane laser system

A Spectra Physics Ti:Sapphire laser system (Hurricane) which can emit 130fs pulses at 800nm with a maximum repetition rate of 1kHz was utilized in LIFT experiments. It uses the chirped pulse amplification (CPA) [64] [65] technique to amplify ultrashort pulses to the milli-joule level. Figure 2-2 shows the schematic diagram of a typical CPA system, which, generally speaking, includes four parts: seed laser, stretcher, power amplifier, and compressor [66]. The fundamental working mechanism of CPA is as follows. An initial short pulse produced by the seed laser is first sent to an optical pulse stretches. After being stretched, the pulse is much longer with much lower peak power, which then passes through a power amplifier to get a higher energy pulse. The amplified pulse

will then be recompressed by an optical pulse compressor to get a resulting high energy ultrashort pulse.

The Hurricane laser amplifier includes a seed laser (Mai Tai), a pump laser (Evolution), an optical pulse stretcher, a regenerative amplifier, and an optical pulse compressor, as shown in Figure 2-3.

The Mai Tai comprises a cw diode-pumped laser and a mode-locked Ti:Sapphire pulsed laser. In the first cw pump chamber, Nd^{3+} ions doped in a yttrium vanadate crystal ($Nd:YVO_4$) was pumped by laser diodes to produce 1064nm output, which is subsequently converted to 532nm through a frequency doubling crystal lithium triborate (LBO). The output is then sent to the seed laser chamber which contains a mode-locked Ti:sapphire cavity. The Ti:sapphire

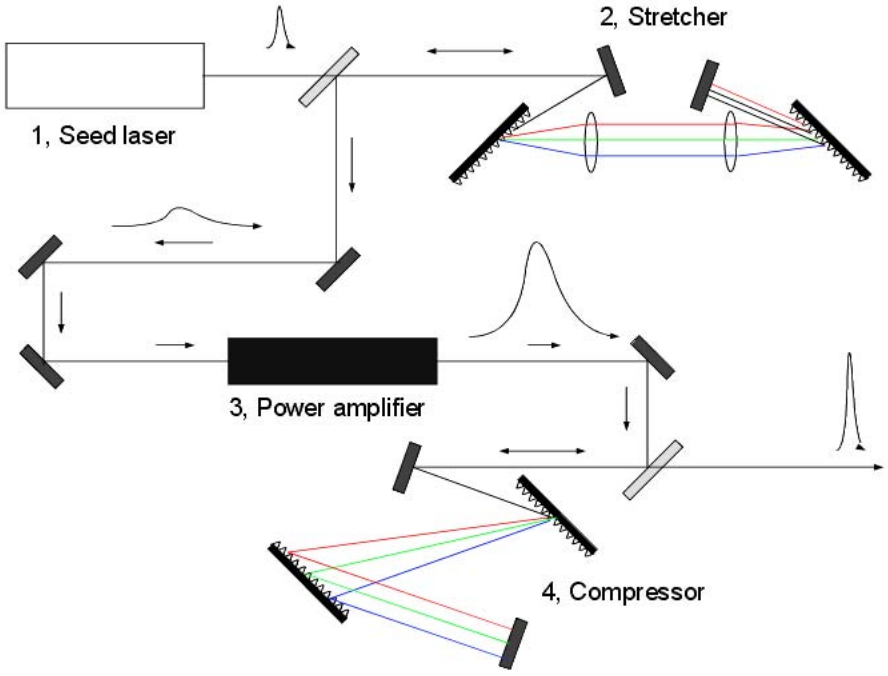

Figure 2-2 A typical chirped pulse amplification system

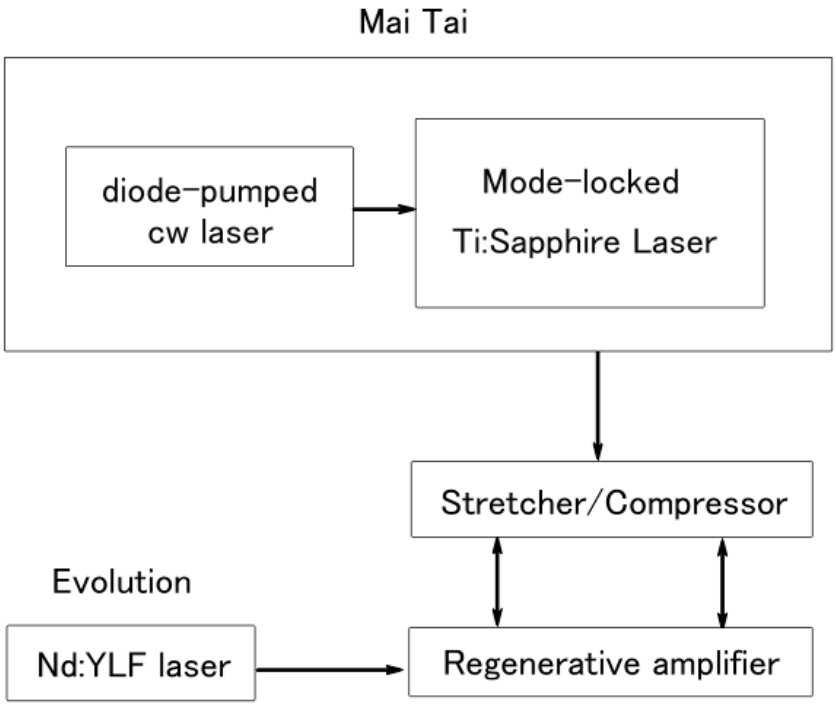

Figure 2-3 Hurricane laser system

is a crystalline material produced by introducing Ti_2O_3 into Al_2O_3 crystal, which has a peak absorption bands in the blue and green (Figure 2-4). Consequently, the 532nm output from cw pump oscillator is an ideal source for the lasing pump of the mode-locked Ti:Sapphire pulsed laser. The final output from the Mai Tai is 100 fs pulses at 800 nm with normal pulse energy of 9 nJ.

The optical pulse stretcher comprises of diffraction gratings. When the input beam is incident on a diffraction grating, the different frequencies will disperse, resulting in the bluer frequency components traveling further through the stretcher than the redder components. As a result, the redder frequency components exit the stretcher first and the pulse is stretched. The stretched pulse is then amplified by the regenerative amplifier, in which the Ti:sapphire laser rod is pumped by an

Nd:YLF laser. Normally, the overall amplification is greater than 10^6 and a few nano-joules input pulse can be amplified to around an mJ.

Finally, the amplified pulse passes through the compressor, where the redder frequency components travel further than the bluer frequency components, which is essentially the reverse of pulse stretching. Thus, the pulse is compressed to nearly its original duration.

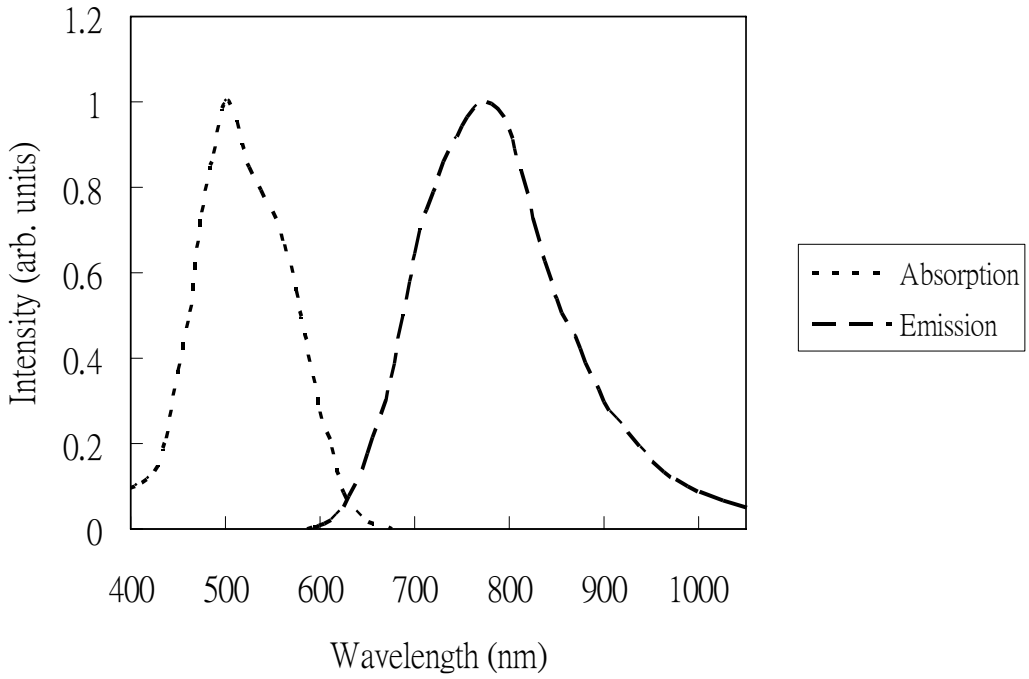

Figure 2-4 Absorption and emission spectra for Ti:sapphire [67]

2.1.1.3 Pulse duration measurement: Autocorrelator

The autocorrelator was used for measuring the pulse by means of an interferometric technique. As shown in Figure 2-5, the input laser pulse is split by a 50/50 beam splitter into two pulses of equal intensity. These two pulses are

then sent to two independent paths. One has fixed optical parts and the other has a delay stage generating an adjustable time delay into one of the pulses. The two pulses then noncollinearly combine within a nonlinear crystal to generate a second harmonic pulse. By changing the delay of one beam, the degree of pulse overlap within the crystal will be changed, which proportionally changes the efficiency of the second harmonic pulse generated from the interaction of the two beams. By monitoring the intensity of violet generation (around 400nm) as a function of position, the autocorrelation duration can be determined. The laser pulse duration can be deduced from the autocorrelation duration by assuming the laser pulse has a Gaussian or a $Sech^2$ profile. Typically a Gaussian profile was assumed in our measurements.

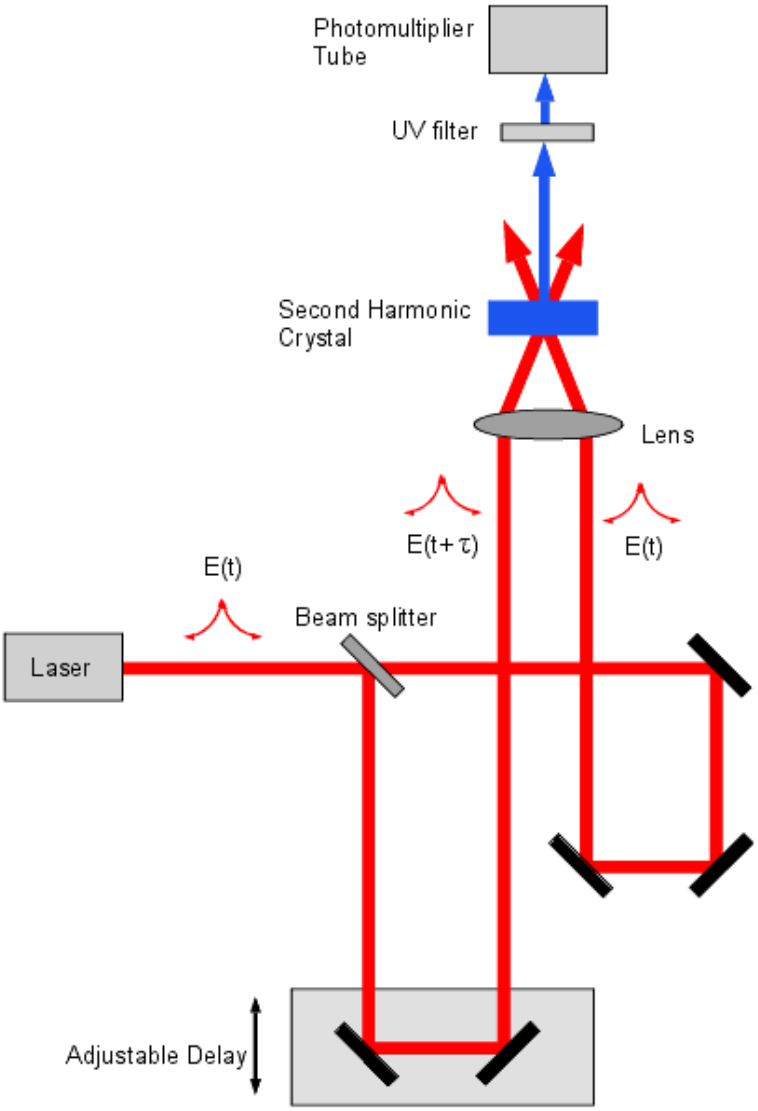

Figure 2-5 Schematic of the optical autocorrelation

2.1.2 Substrate

The donor substrate has to be transparent to laser pulse. Glass microscope slides deposited with target material were used as the donor substrates. The Fisherbrand microscope slides distributed by Fisher Scientific were chosen to be used for both the donor and acceptor substrates. These slides were either 25×75×1.0mm or 50×75×1.0mm. Details of substrate preparation, including

Piranha cleaning and target material deposition will be discussed in Chapter 3.

2.1.3 Target material

Various kinds of target material have been reported to be transferred by LIFT technique, including metals, compounds, organic materials and viscous nanoparticle suspensions. Compared with other material, metal is easy to be deposited and patterned on the donor substrate, thus it is chosen as the target material in our experiment.

Table 2-1 and 2-2 list the thermal properties and optical properties of metals that have been reported to be transferred by LIFT technique. Compared with other metals, Cr has a similar boiling temperature but a much higher melting temperature. When transferred, the material will tend to keep solid phase instead of liquid phase. At 800nm wavelength, Cr has a larger skin depth than other metals listed. Thus a thicker layer can be deposited on the donor glass substrate. The normal incident reflectivity of Cr is the lowest among the metals in Table 2-2 thus more energy will be absorbed by Cr. As a result, the laser pulse works efficiently and it is easier to reach the threshold fluence. Cr is commonly used as an adhesion layer for other metals for bonding to glass substrate. Thus, it is expected Cr can be directly deposited on the glass substrate with good adhesion. Due to the reasons mentioned above, Cr was chosen as the target material in our case. Details of the sample preparation will be discussed in Chapter 3.

Metal	Atomic weight (amu)	T_{melt} (°C)	T_{boil} (°C)	ρ (g/cm^3)	γ ($J/[m^3K^2]$)	κ_0 (W/[mK])	C_i ($10^6 J/m^3K$)	T_F ($10^4 K$)	E_F (eV)
Ag	107.87	961.78	2162	10.5	65.1	429	2.47	6.38	5.49
Al	26.98	660.37	2519	2.7	135	237	2.42	13.6	11.70
Au	196.97	1064.2	2856	19.3	71.4	317	2.49	6.42	5.53
Cr	51.996	1907	2671	7.15	194	94	3.24	8.01	6.89
Cu	63.55	1084.6	2562	8.96	94.3	401	3.44	8.16	7.00

Table 2-1 Thermal properties of metals at room temperature. T_{melt} is the melting temperature, T_{boil} is the boiling temperature, ρ is the density, γ is the constant of electron heat capacity, κ_0 is the constant of electron thermal conductivity, C_i is the lattice volumetric heat capacity, T_F is the Fermi temperature and E_F is the Fermi energy [62][68-70]

Metal	Refraction index n	Extinction coefficient k	Normal incidence reflection R	Absorption coefficient α $[m^{-1}]\times10^7$	Skin depth δ (nm)
Ag	0.27	5.79	0.969	9.09	11.0
Al	2.75	8.31	0.868	13.05	7.7
Au	0.08	4.56	0.986	7.16	14.0
Cr	4.19	4.34	0.634	6.80	24.0
Cu	0.26	5.26	0.965	8.26	12.1

Table 2-2 Optical properties of metals at wavelength 800 nm [69][71]

2.2 Experimental techniques

2.2.1 Experimental setup

A schematic diagram for the LIFT setup is shown in Figure 2-6. 130fs pulses at 800nm with a maximum repetition rate of 1 kHz were emitted by the Hurricane laser system, which was described in section 2.1.1.2. Typically single shot mode was used in the LIFT experiment and the typical maximum output energy was ~500μJ per pulse. The single pulse mode was achievable by either reducing the frequency to 1Hz or using a hand pulser to trigger the Hurricane one shot at a time. This output pulse was reflected by the dielectric mirror 1 (M1) to pass through the first adjustable aperture (A1), which together with the second adjustable aperture (A2) placed at the end of the optical table, were used to align the laser beam on the main beam path. When aperture A1 was reduced to a very small hole (~1 mm), a diffraction pattern formed. By centering this pattern to the second aperture A2, the laser beam was aligned. Aperture A2 was monitored by CCD camera C2 and the image of aperture can be viewed on a TV screen. The half-wave plate (H) and GLAN polarizer (G) were located after aperture A1, for varying pulse energy (Figure 2-7). The half wave plate is an optical device that can rotate the polarization state of a plane-polarized light travelling though it, by retarding the ordinary ray which is perpendicular to the optic axis by half a wavelength, or 180 degrees, without changing the extraordinary ray which is parallel to the optic axis. As shown in Figure 2-7, a plane-polarized wave is normally incident on a half

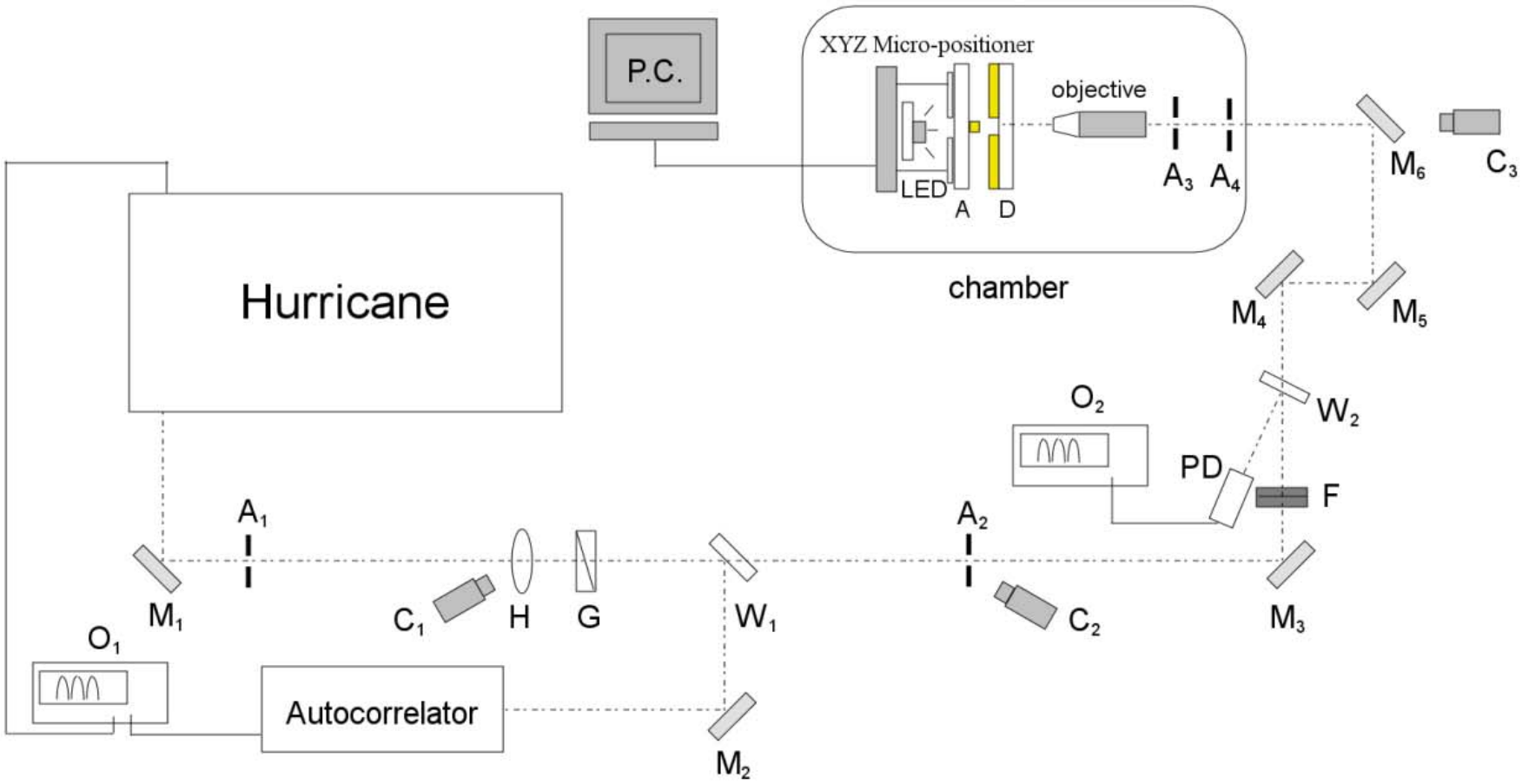

Figure 2-6 Schematic of setup. M_1, M_2, M_3, M_4, M_5 & M_6: dielectric mirrors coated for 800 nm 45° angle of incidence; A_1,A_2, A_3 & A_4: apertures; C_1, C_2 & C_3: CCD camera; H: half wave plate; G: GLAN polarizer; W_1 & W_2: dielectric wedge; F: ND filters; O_1 & O_2: Tektronix TDS 360 oscilloscope; PD: photodiode

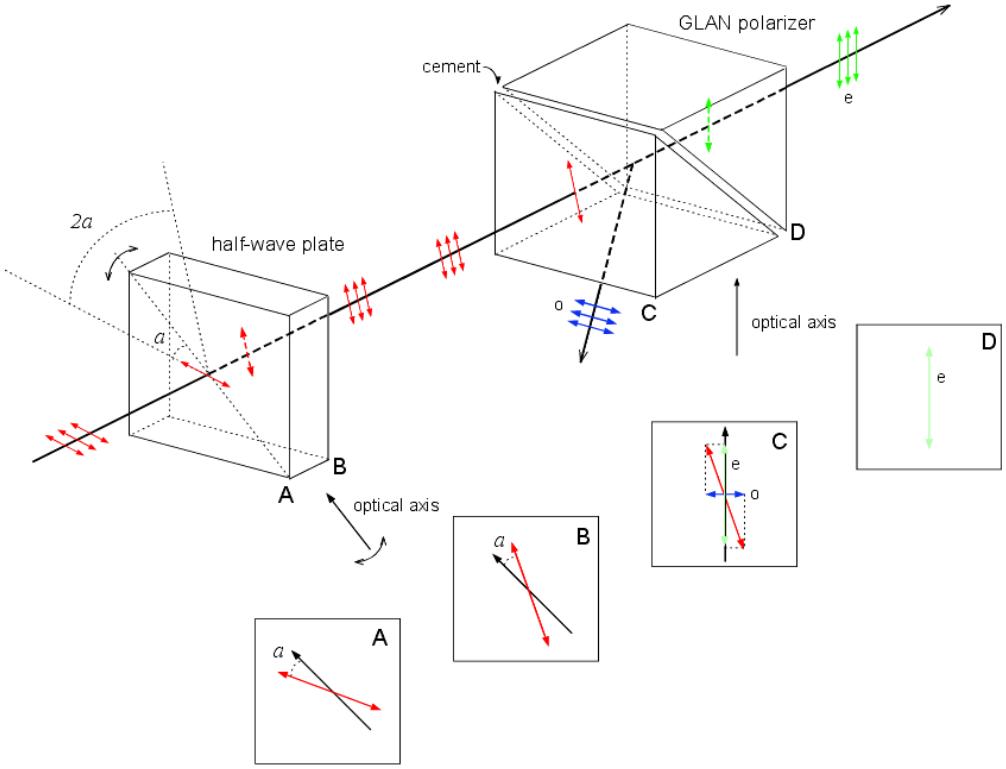

Figure 2-7 Half-wave plate and GLAN polarizer

wave plate. If the angle between the plane of polarization and the optical axis is *a*, after passing through the plate, the original plane wave is rotated through an angle 2 *a*. This rotated beam is then incident on the GLAN polarizer, which is a type of polarizing prism consisting of two right-angled calcite prisms that are cemented together by their long faces. Due to birefringence, the beam is decomposed into two rays with different refraction indices. The ordinary ray is totally internally reflected from the calcite-cement interface, while the extraordinary ray is allowed to pass through the GLAN polarizer. The half-wave plate in our system can be rotated on the beam path. As a result, the plane of polarization can be rotated by any angle after it passes the half-wave plate. The GLAN polarizer is fixed, thus

the amplitude of extraordinary ray component can be varied as the incident beam is rotated by a certain angle by the half-wave plate. Consequently, the energy of the beam is adjustable.

After being reflected by the dielectric mirror M3, the beam energy was reduced by several calibrated Schott ND filters to obtain energies of 10nJ - 10μJ pulse energies required in the experiments. A dielectric wedge was located right behind M3, which reflected a small portion of light to the photodiode PD, letting the rest pass through the wedge. The pulse detected by PD was measured on a Tektronix TDS 360 digitally oscilloscope with a 10X attenuator. The beam was then reflected by dielectric mirrors M4, M5 and M6 to be guided into the chamber. Apertures A2 and A3 were used to align the light, making sure it is normally incident on the 10X microscope objective, with NA=0.25. The transmission of the microscope objective was measured to be 0.735, as seen in Figure 2-8. The laser pulse was then focused onto the thin film, through the donor glass substrate to transfer the material onto the acceptor substrate. The transmission of the donor glass substrate was measured to be around 0.9, as shown in Figure 2-9. The donor substrate and acceptor substrate were located underneath the microscope objective, both of which were held by the XYZ micro-positioner. These two substrates were first cleaned by Piranha solution (mixture of Sulphuric Acid and Hydrogen Peroxide on the scale of 3:1) in a clean room and transported to the LIFT set up in a clean container and then they were put in contact during the experiment. However, there may still be dust on the substrates and the substrates my not be

perfectly flat thus we expect the gap would be on the order of a few microns. This whole plate can be moved by a PC, with a control system designed in Labview software. A CCD camera connected with a TV screen was applied to monitor the focusing condition and the transfer process. A LED was placed underneath the acceptor substrate, providing back illumination to the surface of the acceptor substrate. The brightness of the LED was adjustable.

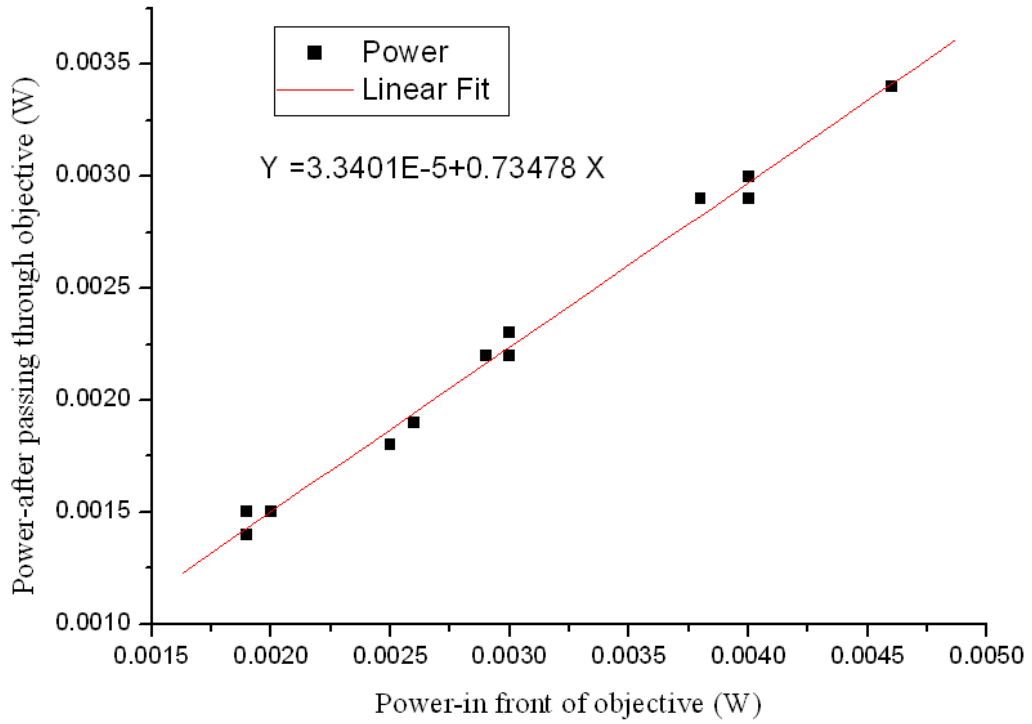

Figure 2-8 Transmission of microscope objective measurement

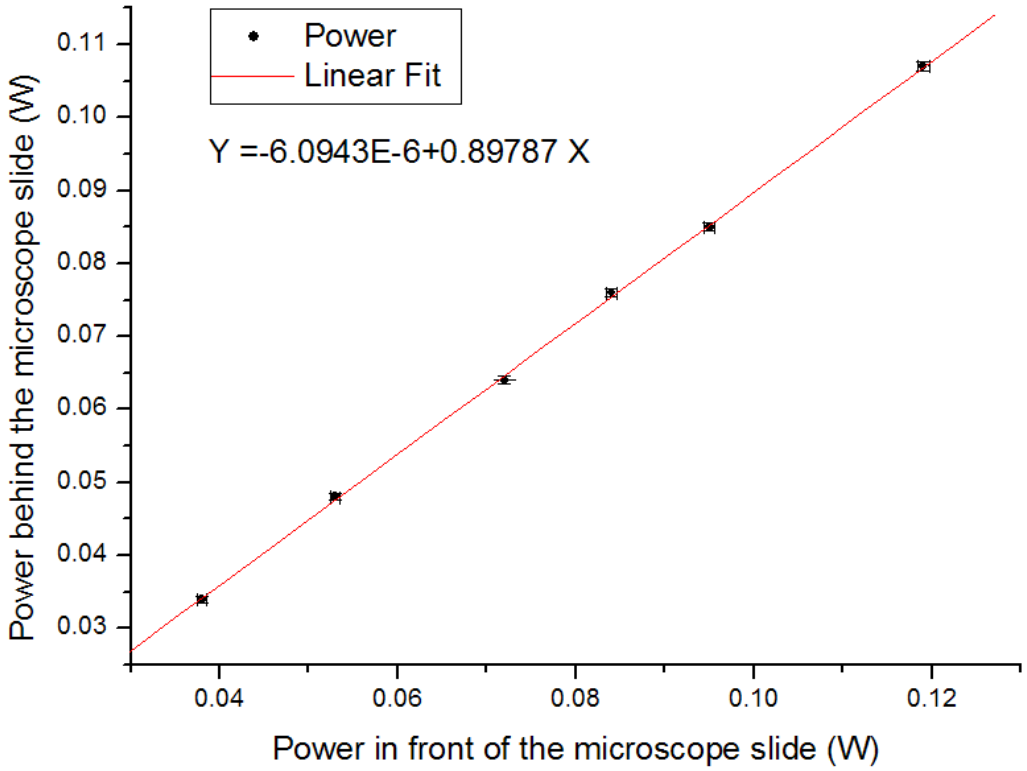

Figure 2-9 Transmission of donor glass substrate measurement

2.2.2 Pulse energy measurement and photodiode calibration

The photodiode connected with the Tektronix TDS 360 digital oscilloscope was used to measure pulse energy as a real time monitor. This photodiode had to be calibrated first to obtain the laser power as a function of photodiode voltage. By simply reading the voltage on the panel of oscilloscope, the laser power can be calculated from the relationship.

Figure 2-10 shows the schematic diagram of the calibration process. A Spectra-physics Model 407A power meter was used to calibrate the photodiode.

During the calibration, the microscope objective was moved away. Instead the power meter was located right above the XYZ micro-positioner. The laser power was read from the panel of the power meter with accuracy of 10 mW, 5 mW, 1 mW, and 0.5 mW for the meter range of 1 W, 300 mW, 100 mW, and 30 mW respectively. The small portion of light collected by the photodiode was converted into current, which was sent to the oscilloscope through a 10X attenuator afterwards to display a relative voltage on the panel. Figure 2-11 shows the calibration curve. A linear fit was plotted, giving a relationship between laser power and photodiode voltage. In the experiment, the laser power measured from this equation had to be multiplied by the transmission ratio of the microscope objective and the transmission ratio of the donor microscope slide to obtain the final energy arriving at the donor substrate.

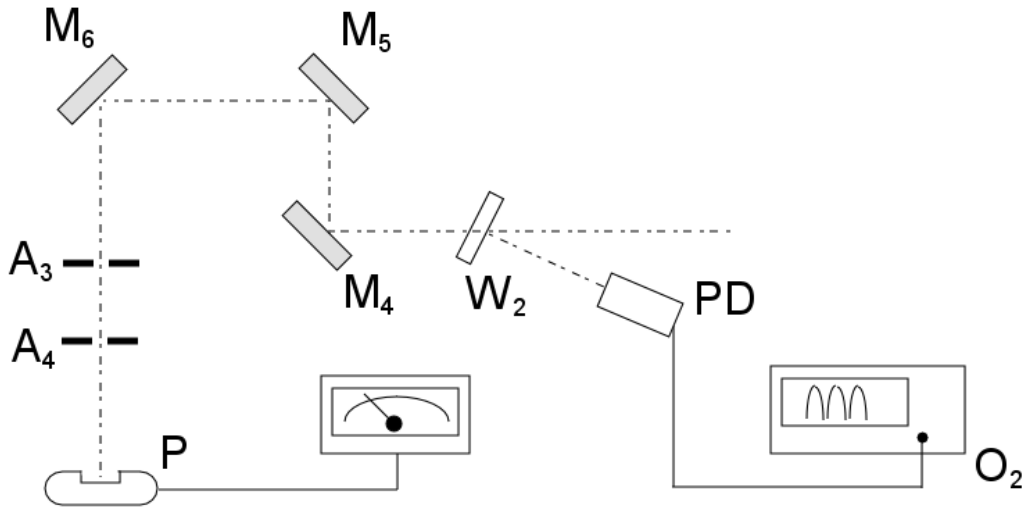

Figure 2-10 Photodiode calibration. M_4, M_5 & M_6: dielectric mirrors coated for 800 nm 45° angle of incidence; A_3 & A_4: apertures; W_2: dielectric wedge; O_2: Tektronix TDS 360 oscilloscope; PD: photodiode; P: Spectra-physics 407A power meter.

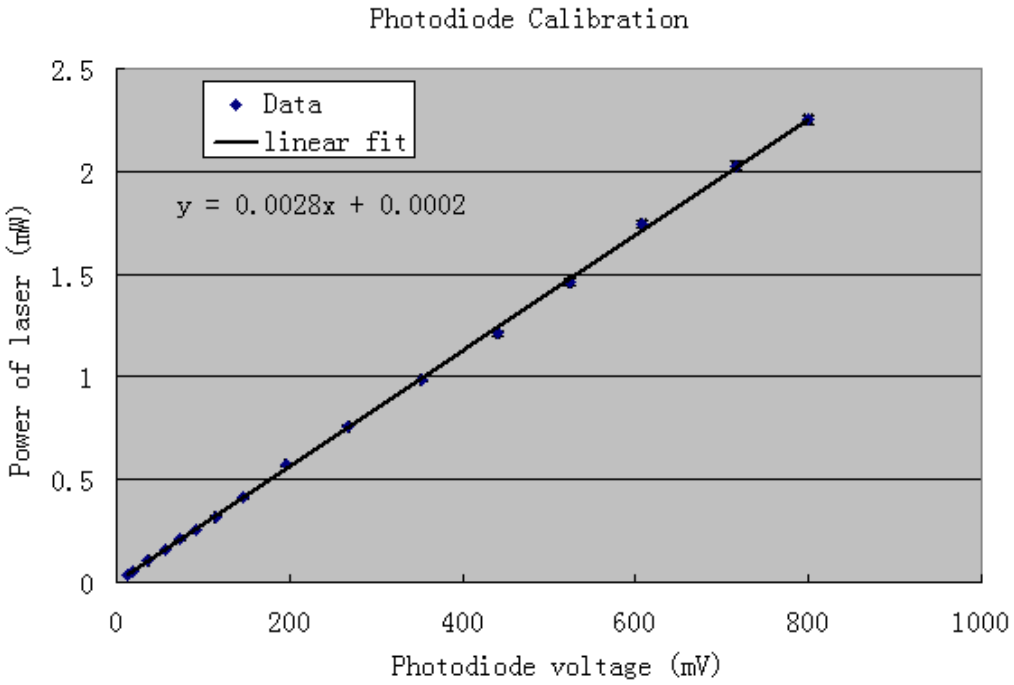

Figure 2-11 Photodiode calibration curve

2.2.3 Focal spot size measurement

In order to measure laser fluence, the focal spot size had to be determined first. In our experiment, the Gaussian beam limiting technique (GBLT) [72] was applied for *in situ* measurements of pulsed Gaussian-beam focused on the donor film. This technique is briefly discussed as follows.

The electric field distribution of a Gaussian beam spatial profile is given by:

$$E(r,z) = E_0 \frac{w_0}{w(z)} \exp\left(-\frac{r^2}{w^2(z)}\right) \exp\left(-j\left(kz - \varphi(z) - \frac{kr^2}{2R(z)}\right)\right) \qquad 2\text{-}7$$

where E_0 is the peak electric filed amplitude; r is the radial spatial distance from the center axis of the beam; z is the direction along the optical axis; $w(z)$ is the radius at which the field amplitude drops to 1/e of it peak value on the axis;

$w_0=w(0)$ is the minimum beam waist; $\varphi(z)$ is the Guoy phase shift; $R(z)$ is the phase front curvature, and k is the propagation wave vector.

If only the amplitude part is considered, eqn. 2-7 can be simplified as:

$$E(r,z) = E_0 \frac{w_0}{w(z)} \exp\left(-\frac{r^2}{w^2(z)}\right) \qquad 2\text{-}8$$

In a medium with impedance η, the corresponding time averaged intensity distribution in the radial direction becomes:

$$I(r) = \frac{E(r)E^*(r)}{2\eta} = \frac{E_0^2}{2\eta}\frac{w_0^2}{w^2(z)}\exp\left(-2\frac{r^2}{w^2(z)}\right) = I_0(z)\exp\left(-2\frac{r^2}{w^2(z)}\right) \qquad 2\text{-}9$$

Where $I_0(z)$ is the group of constants, indicating the peak intensity. At a certain position $z=z_0$, the beam waist can be written as w_0 (now the 2 e-folding intensity beam waist). By multiplying the intensity in eqn. 2-9 by the pulse width τ, the radial distribution of fluence that is incident on the sample is derived as

$$\phi(r) = \phi_0 \exp\left(-2\frac{r^2}{w_0^2}\right) \qquad 2\text{-}10$$

By equating $2r$ by damage spot diameter D and defining the fluence at this radius as the ablation threshold, eqn. 2-10 can be rewritten as:

$$\phi_{th} = \phi_0 \exp\left(-2\frac{(D/2)^2}{w_0^2}\right) \qquad 2\text{-}11$$

Thus

$$D^2 = 2w_0^2 \ln\left(\frac{\phi_0}{\phi_{th}}\right) \qquad 2\text{-}12$$

The peak fluence ϕ_0 in eqn. 2-12 can be derived from the total pulse energy:

$$E_{pulse} = \int \phi(r) dA = \int_0^{\infty}\int_0^{2\pi} \phi_0 \exp\left(-2\frac{r^2}{w_0^2}\right) r dr d\phi$$

$$= 2\pi\phi_0 \int_0^\infty r \exp\left(-2\frac{r^2}{w_0^2}\right) dr = 2\pi\phi_0 \left(-\frac{w_0^2}{4}\right) \exp\left(-2\frac{r^2}{w_0^2}\right)\Bigg|_0^\infty$$

$$= \frac{\pi w_0^2 \phi_0}{2} \qquad 2\text{-}13$$

Thus $$\phi_0 = \frac{2E_{pulse}}{\pi w_0^2} \qquad 2\text{-}14$$

Substituting eqn. 2-14 into 2-12, the equation is derived as:

$$D = 2w_0^2 \left(\ln\left(E_{pulse}\right) - \ln\left(\frac{\pi w_0^2 \phi_{th}}{2}\right)\right) \qquad 2\text{-}15$$

E_{pulse} and D can be measured in the experiment. Thus there are two unknowns in eqn. 2-15, w_0 and ϕ_{th}. The 2 e-folding intensity beam waist radius w_0 can be calculated from the slope of the regression line of the semi-logarithmic plot of E_{pulse} and D^2. Similar to eqn. 2-14, E_{th} can be defined. So eqn. 2-15 becomes:

$$D = 2w_0^2 \left(\ln\left(E_{pulse}\right) - \ln\left(E_{th}\right)\right) \qquad 2\text{-}16$$

By making a semi-logarithmic plot of E_{pulse} and D^2, the energy threshold value can be obtained from the intersection of the plot with the horizontal axis. The results calculated by this technique will be presented in Chapter 4.

2.2.4 Thickness measurement-Profilometer

Profilometer is an instrument used to measure a surface's profile and quantify its roughness, by using a diamond-tipped stylus to contact directly and scan across the surface. The resolution typically depends on the radius of the stylus and the geometries of the features. In our case, the Alpha Step 200 Profilometer in

NanoFab was used to measure the Cr film's profile and thickness. The radius of the stylus is 12.5 microns and the theoretical resolution is 5 nm. After scanning, the sample leveling can be automatically computed and the scan area is displayed.

2.2.5 Morphology-Scanning electron microscope (SEM)

The surface morphology of the ablated spots on donor substrate and the transferred material on acceptor substrate was characterized by the scanning electron microscope. The Zeiss Leo 1340 in NanoFab and JEOL JSM6301FXV in Geology department were used in the project. The electrons are emitted from cathode and then accelerated by a high voltage (5-20 kV). The accelerated electrons are then focused into a vey fine spot size (~1nm) to strike the sample, generating secondary electrons from the material at the depth of ~50 Å. By detecting the secondary electrons generated by the bombardment of the incident electron beam, SEM image is formed.

Chapter 3

Sample preparation

3.1 Continuous Cr film

All the sample preparation procedures were conducted in NanoFab at University of Alberta. Since the cleanliness and smoothness of a substrate may critically affect nucleation and crystal growth, as well as affecting impurity concentration, the donor substrate had to be cleaned before a thin metal film was deposited on it. The acceptor substrate needed to be carefully cleaned before the LIFT process too, in order to ensure the quality of transferred material.

The Piranha solution, which was prepared by mixing Sulphuric Acid and Hydrogen Peroxide on the scale of 3:1, was applied for solvent cleaning of glass substrates. The substrates were first immersed in Piranha solution for 15 minutes and then rinsed by de-ionized (DI) water for 5 full cycles in the dump rinser. Once DI water rinse step was finished, the substrates were dried by nitrogen gun.

The sputtering, a process whereby material is dislodged and ejected from the surface of a solid due to the momentum exchange associated with surface bombardment by energetic particles [73-76], was applied to deposit Cr thin film on donor substrate. Figure 3-1 illustrates a DC plasma sputtering system, where a high voltage is applied across a low-pressure inert gas (usually Argon at about 1-100 mTorr), making the target a cathode (-200 V to -5 kV). The free electrons

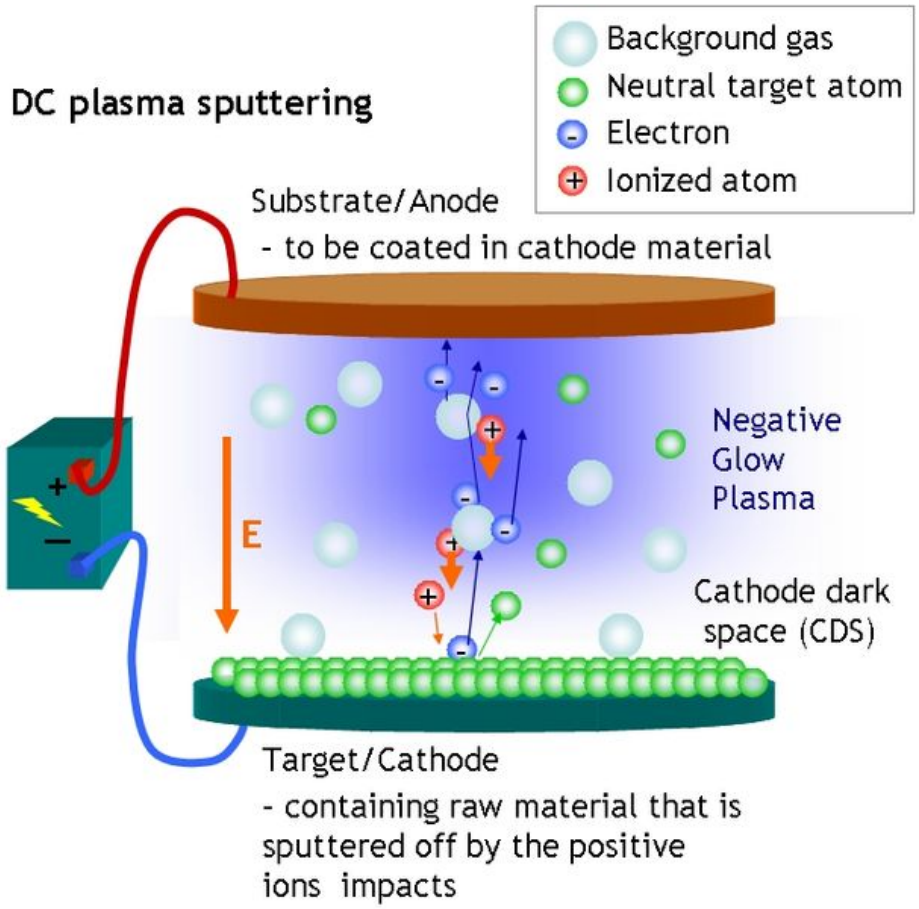

Figure 3-1 DC Plasma Sputtering [77]

from low pressure gas discharge of Argon are accelerated away from the negatively charged target. They will collide with Argon gas atoms in their path,

making them positively charged ions (Ar^+). These positive Ar^+ ions are accelerated into the negatively charged target, striking the target, and causing atoms from the target to be ejected with enough energy to travel to and bond with the substrate. More electrons will also be generated during this striking process, which will feed the formation of ions and the continuation of the plasma. However, this diode sputtering has two major problems. One is the inefficient deposition rate caused by poor ionization efficiency, and the other one is the overheating and possible film damage because some energetic electrons have the potential to reach the substrate. A more useful system called magnetron sputtering [78] [79] can deal with both of these issues (Figure 3-2). Magnets are placed behind the cathode, causing formation of magnetic field above the target surface. Energetic electrons emitted from the cathode are constrained, moving in a helical trajectory around the

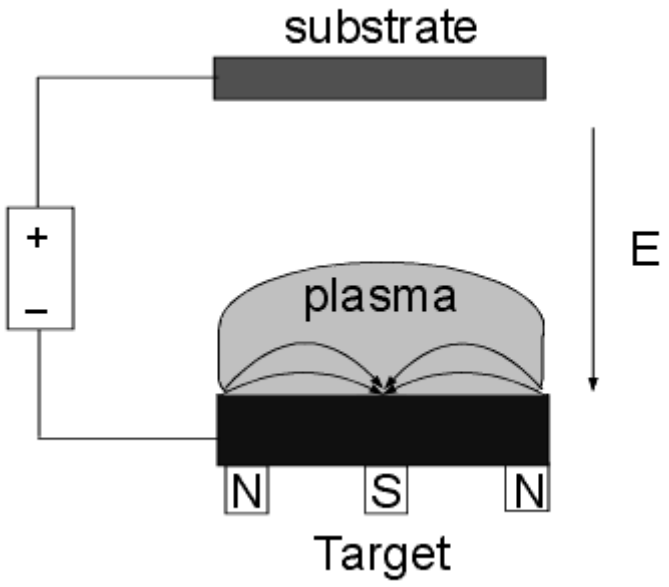

Figure 3-2 DC Plasma Sputtering

magnetic field lines, with a imposed drift know as the E×B drift. As a result, these electrons are no longer free to bombard the substrate to the same extent as with diode sputtering. At the same time the extensive, circuitous path carved by these same electrons when trapped in the magnetic field, enhances their probability of ionizing a neutral gas molecule by several orders of magnitude. This high ionization efficiency will significantly increase the sputter rate.

The sputtering system used in NanoFab is named “Bob”, which is a planar magnetron sputter system. Cr target was placed as a cathode. The major parameters are listed in table 3-1. After deposition for 6 minutes, the final thickness of the Cr film was ~85nm, measured by Alphastep profilometer (Figure 3-3).

	Bob sputtering system
Discharge voltage [V]	~ 340
Base pressure [Torr]	2.5×10^{-8}
Leak rate [Torr 1s/-1]	1×10^{-10}
Argon pressure [Torr]	7×10^{-3}
Cr deposition rate [nm/min]	~ 13.7

Table 3-1 Characteristics of Bob sputtering system

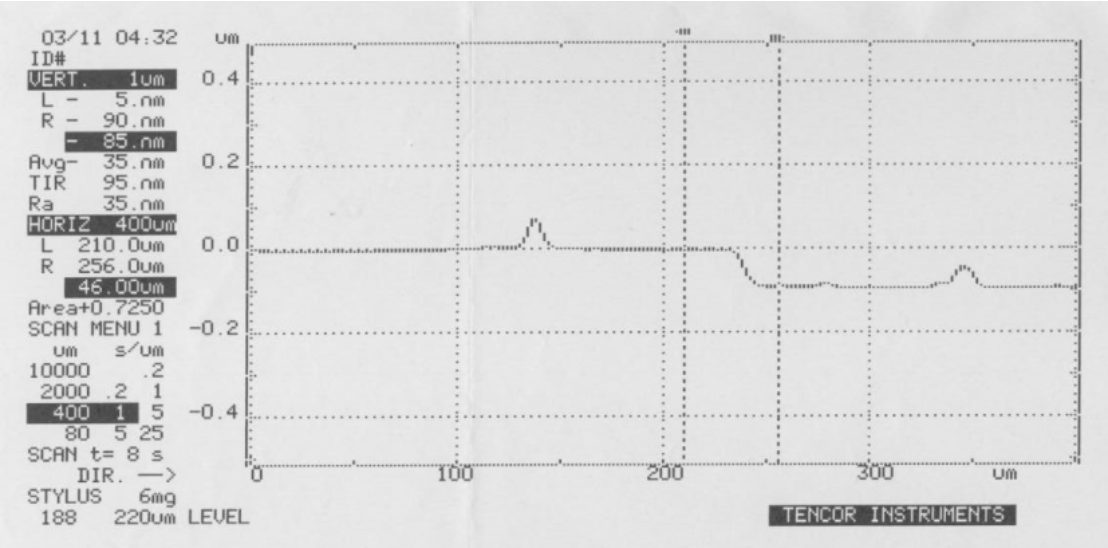

Figure 3-3 Thickness of Cr film measured by Alphastep Profilometer

3.2 Pre-patterned Cr micro-disks fabricated by photolithography

Photolithography, a process by using light to transfer geometric shapes from a photomask to a light sensitive polymer called a photoresist, is applied in microfabrication. After the photoresist is exposed and developed, the material underneath is eroded either by wet etching or by plasma etching [80, 81]. The general sequence of processing steps includes: substrate preparation, photoresist spin coat, prebake, exposure, postexposure bake, development, postbake and photoresist strip, which is shown schematically in Figure 3-4 [82]. The resolution limit of optical lithography is given by the equation

$$W = k_1 \cdot \frac{\lambda}{NA} \qquad 3\text{-}1$$

where W is the resolution. λ and NA are the exposure wavelength and numerical aperture of the optical lithography tool, and k_1 is a constant for a specific

lithographic process, which practically depends on lens aberrations, illumination conditions, mask, geometrical shapes, exposure tool conditions, resists, process, and operator [83]. According to this equation, the resolution limit is greatly affected by the exposure wavelength and *NA*. By decreasing the wavelength, and increasing the *NA*, that is making lenses larger and bringing them closer to the wafer, the minimum feature sizes can be decreased. However, another major limitation named the depth of focus (DOF) is also a concern:

$$DOF = k_2 \cdot \frac{\lambda}{NA^2} \qquad 3\text{-}2$$

where k_2 is a constant for a specific lithographic process. Though the use of high

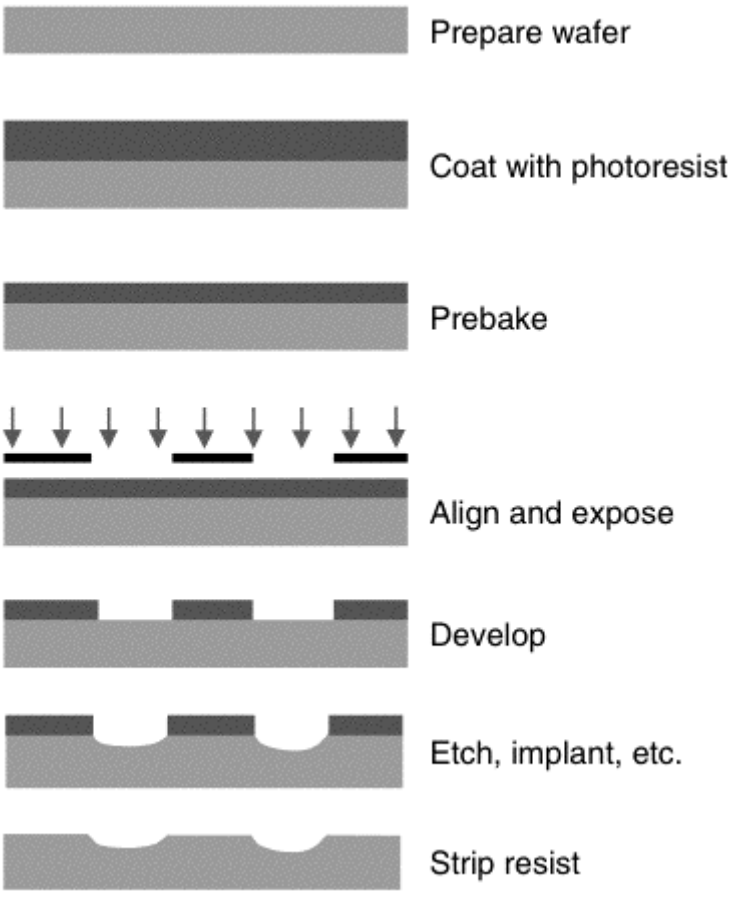

Figure 3-4 Example of a typical sequence of lithographic processing steps for a positive resist

NA tools can increase resolution, the depth of focus will decrease dramatically due to *NA* squared, which even can drop down to less than 1μm [84]. Consequently, the thickness of the photoresist and the depth of the topography on the wafer are restricted when high *NA* tools are used.

The purple ultraviolet light originally used in photolithography were 436nm (Hg G-line), 405nm (Hg H-line) [85] and 365nm (Hg I-line), which were filtered from Hg gas-discharge lamps to select a single spectral line. In 1980s, the next technology transition occurred by using the deep ultraviolet (DUV) 248nm wavelength, which was produced by KrF excimer lasers. In 1990s, the shift to a new wavelength of 193 nm produced by ArF excimer laser occurred [86-88]. This light source, together with the liquid immersion lithography, which was first proposed by Takanashi *et al.* in 1984 [89] and by Tabarelli and Lobach in 1985 [90] by introducing a liquid medium that has a refractive index greater than one between the final lens and the wafer surface, helps improve the resolution under 100nm [91]. Photolithography using 157 nm DUV is being developed too. In our case, the photolithography system uses 405nm and 365nm. It is difficult to produce a pattern under 1μm.

3.2.1 Photomask fabrication

A photomask, from which the pattern is transferred to another substrate, typically is fabricated at the first step in the microfabrication process. Figure 3-5 summarizes the mask making procedures in NanoFab at University of Alberta.

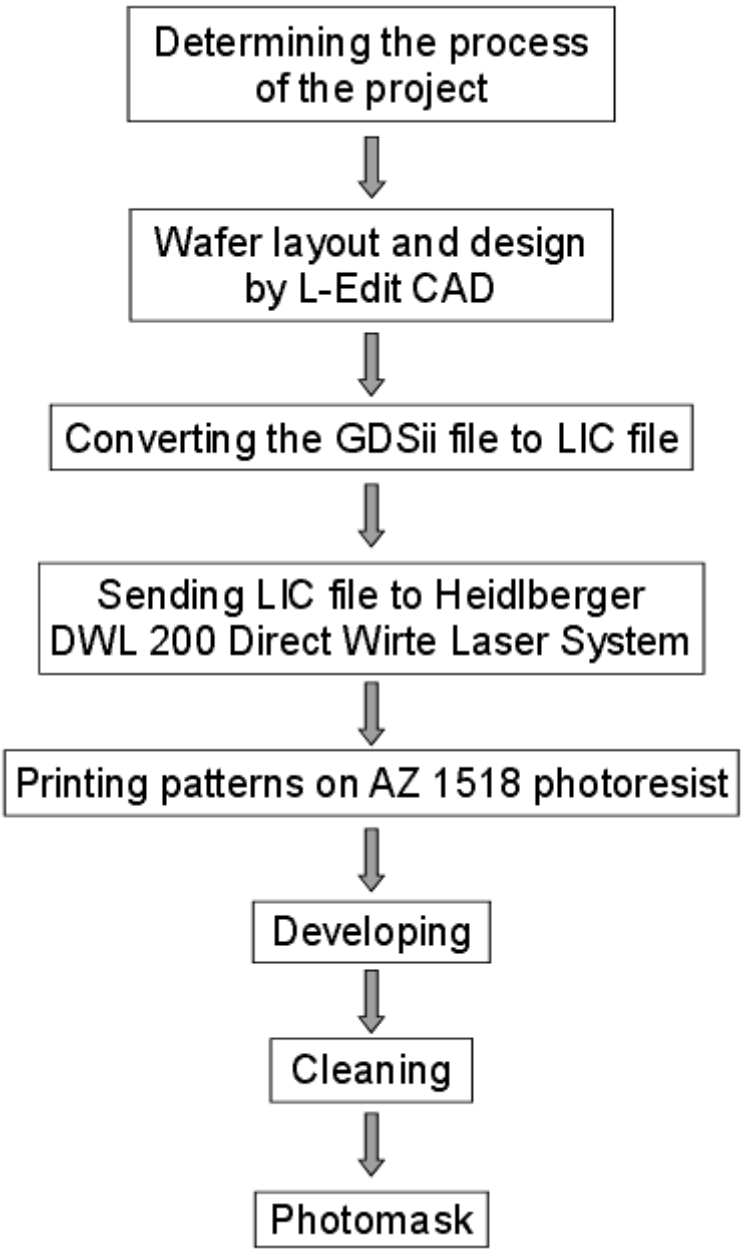

Figure 3-5 Procedures of photomask fabrication

Due to the limitation of the photolithography system, the smallest feature we intended to fabricate on the photomask was 1μm. The L-Edit CAD program by MEMSPro was used at NanoFab to do the wafer design. In L-Edit, the final complex device design is combined by simple shapes such as squares and circles, and a file is typically composed of any number of cells which are hierarchically related. Figure3-6 shows the interface of L-Edit, including three important sections, which are toolbars, sidebar and drawing area. Figure3-7 shows the overview of the photomask design. Since the photomask uses a 5 inches lime glass square with a thickness of 0.09 inches, the design on L-Edit is also a 5×5 inches square, fitting the size of the glass square. In this pattern, the red will be chrome

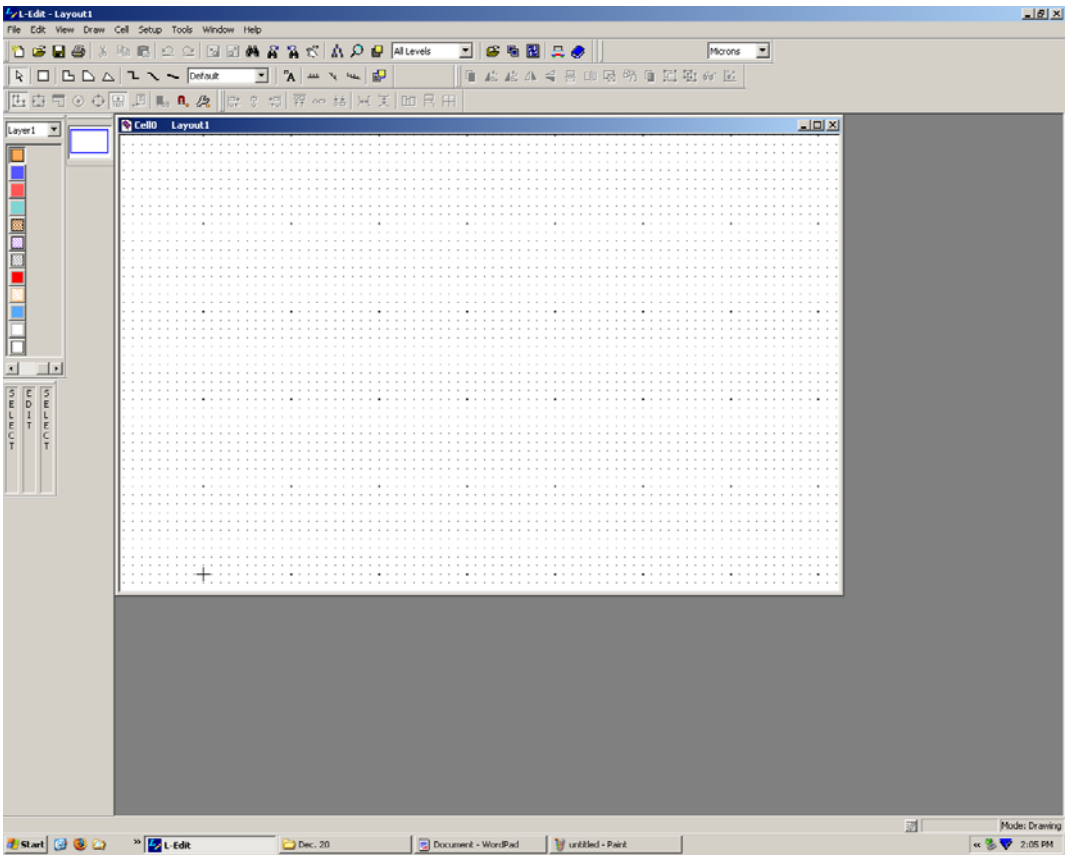

Figure 3-6 L-Edit Interface (Three main sections: toolbars, sidebar and drawing area)

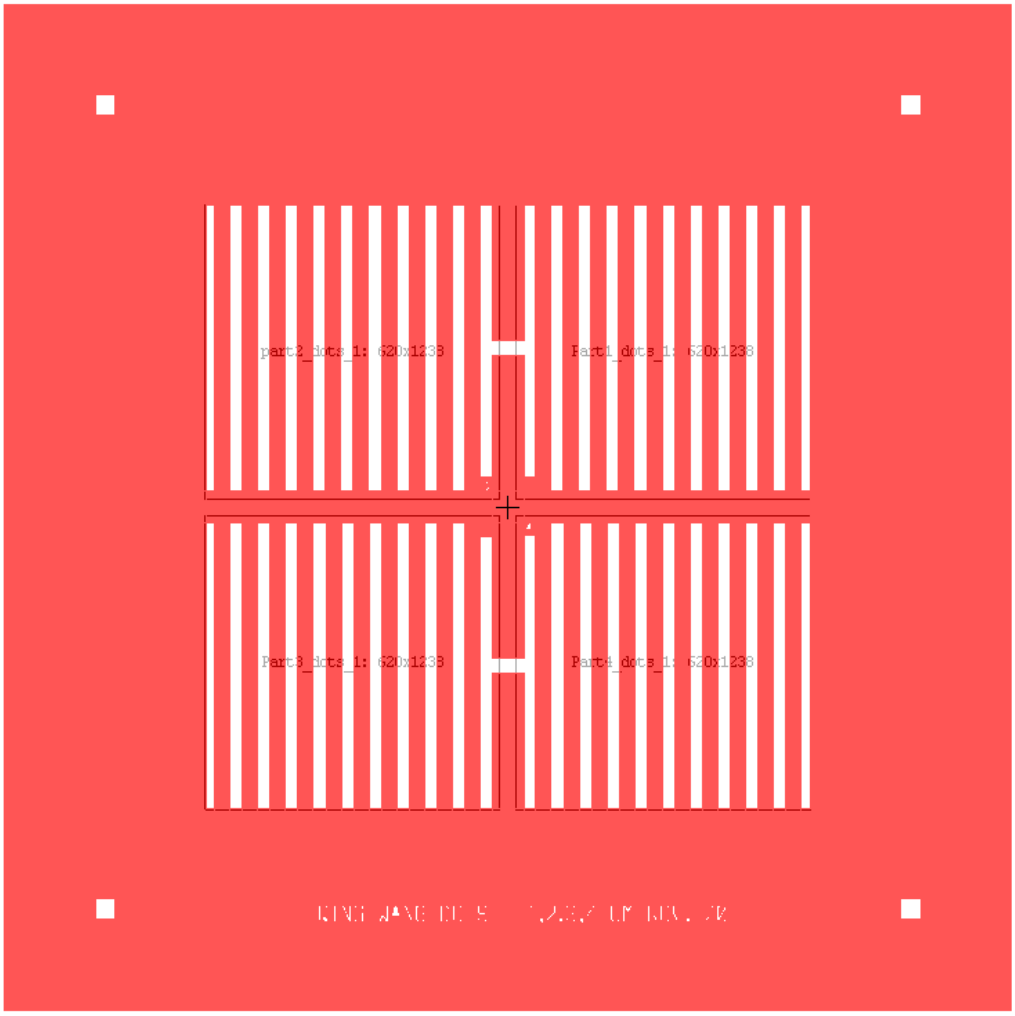

Figure 3-7 Overview of the photomask design (a: region 1, top right, the smallest feature is 1μm disk; b: region 2, top left, the smallest feature is 2μm disk; c: region 3, down left, the smallest feature is 3μm disk; d: region 4, down right, smallest feature is 3μm disk)

coating on the photomask, and the white will be non-coated glass surface on the mask. The center square was designed to be 3×3 inches, so it would fit the size of the donor substrate. This square was divided into 4 equal quarter regions, each of which contained the smallest disk in different sizes, from 1μm to 4μm. This is because the isotropic chemistry will occur during developing and etching. So the real pattern on the photomask and the final donor substrate is not the same size as that on the L-Edit design (usually around ±0.7μm). The variation on the 4 quarter

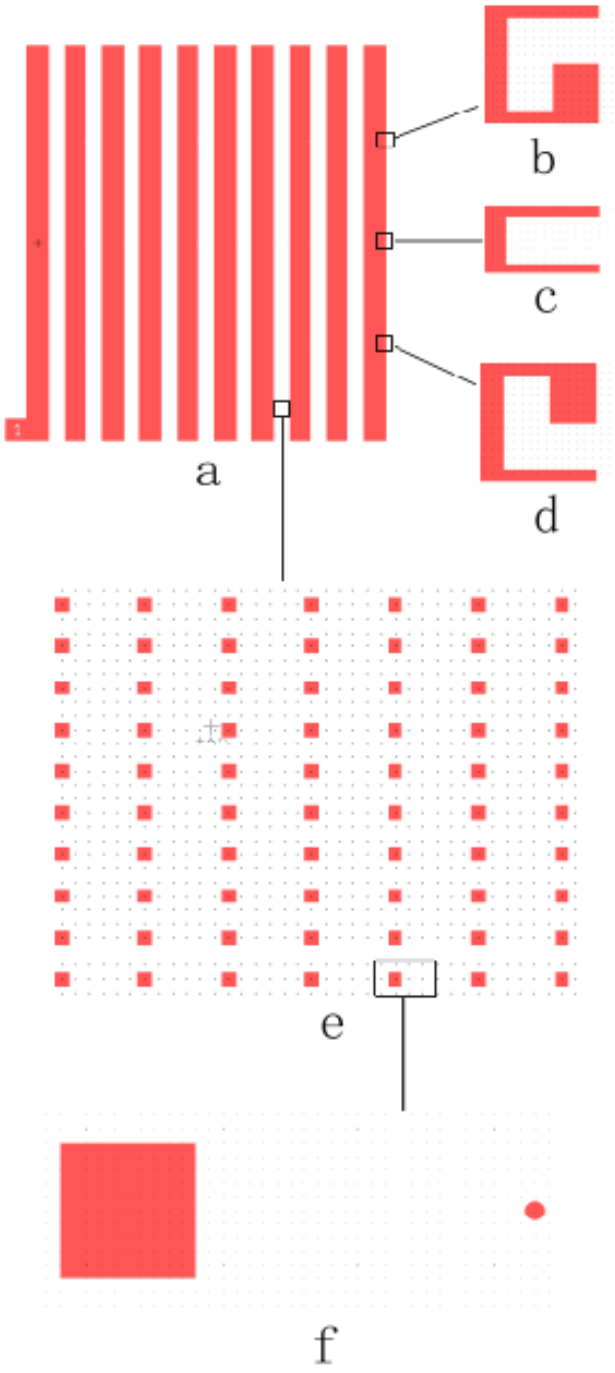

Figure 3-8 Details of the design in portion 1

regions would ensure that we could finally get some tiny structures on the donor substrate. Figure 3-8 shows the details of the design in region 1. This part was divided by several lines of continuous film, between which were patterns of small disks and 10μm squares. A single line of continuous film was 1.5 inches long and 2mm wide. This continuous film was used to determine the optimum focal position before the laser was illuminated onto the small disks during experiment. Since the small disks were only tens to hundreds μm next to the continuous film line, when laser was horizontally moved from the continuous film line onto the small disks, the focal condition should almost be the same. The notches b, c and d were designed at 1/4, 1/2, and 3/4 along the continuous film line, giving us some hints about where we were when the donor substrate was inspected under the CCD camera. Figure 3-8 (f) illustrates a basic cell in the disk pattern area, where a 1μm disk was deigned 30μm away from the 10×10μm square. Because the 1μm disk was too small to be seen by the alignment system, the 10×10μm square was designed as a marker which can be easily seen by the CCD camera. By focusing the laser on the big square and moving the substrate 30μm afterwards, the laser spot can focus on the 1μm disk readily. This basic cell was repeatedly designed to form a whole pattern between each continuous line, as shown in Figure 3-8 (e). The sections 2, 3 and 4 had the same pattern as section 1, except 1μm disk was replaced by 2μm, 3μm and 4μm disks respectively.

When the design was completed, the GDSii file saved in L-Edit was converted and compiled into LIC file that enabled DWL 200 to control laser movement. The

following printing, developing and cleaning procedures were done by NanoFab staff. Briefly, the mask, a 5 inches soda lime glass square with a thickness of 0.09 inches, was coated with chrome and 530nm of AZ 1518 photoresist first. Then the Heidelberg DWL 200 Direct Write Laser System, a highly precise, accurate, and resolved instrument, used 413nm radiation produced by a Krypton-Ion laser to write patterns by raster scanning the blank mask plate. Afterwards, chemical developing, etching and cleaning processes were applied to make the final photomask. Figure 3-9 shows the microscope image of the 1μm disk pattern on the photomask.

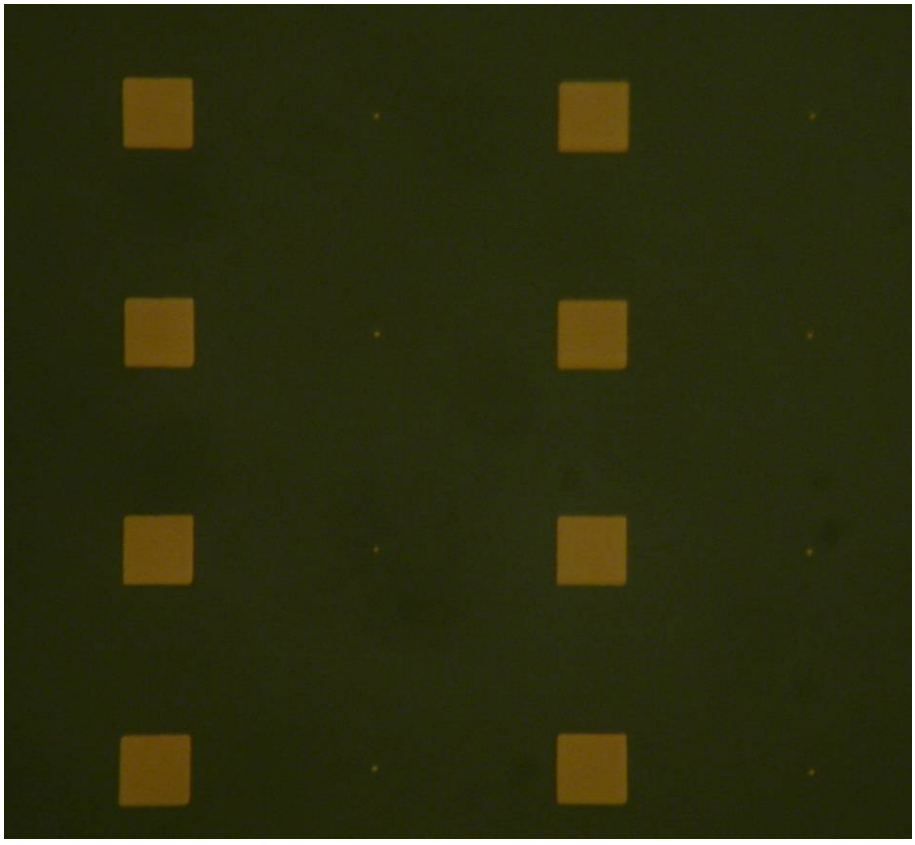

Figure 3-9 Microscope image of the photomask (1μm disk)

3.2.2 Substrate preparation

The microscope slide was cleaned by Piranha solution first and then was covered by a thin Cr film by the Bob sputtering system, as described in section 3.1. The thickness of the Cr film was ~80nm.

3.2.3 Photoresist coating

Photoresist is a light-sensitive material that can form a relief image after it is exposed and developed. Usually, a photoresist contains an organic resin to help form very uniform films and good thermal, mechanical and etch stability. Other components have to undergo chemical changes under exposure, making sure that the exposed areas turn either more soluble or less soluble than the unexposed areas [92]. The photoresist in which the area becomes more soluble when it is exposed to light is called positive photoresist. The relief image formed at the wafer level will be the same as the one in the mask. The photoresist in which the area becomes less soluble when it is exposed to light is called negative photoresist, and the relief image is complementary.

In the NanoFab, there are three types of photoresist: HPR 504, HPR 506, and AZ P4620. When it is coated on the substrate, the photoresist film thickness is typically 1-1.5μm, 2μm and 12μm respectively. HPR 504, which can produce the thinnest film among the three, is desirable in the process to fabricate a pattern as

Component	CAS-No.	Concentration
Ethyl Lactate	97-64-3	61-90%
Novolak resin	27029-76-1	10-29%
Naphthoquinone diazide esters	68510-93-0	1-11%

Table 3-2 Components of HPR 504

small as 1μm. Table 3-2 [93] lists the chemical components of HPR 504 used in NanoFab, which was manufactured by Arch Chemicals, Inc.. HPR 504 was coated on the substrate by Solitec spinner using parameters as follows:

a. Spread 500rpm: time = 10 s

b. Spin 4000rpm: time = 40 s

The final thickness of the photoresist HPR 504 thin film was about 1.1μm, measured by Alphastep profilometer (Figure 3-10).

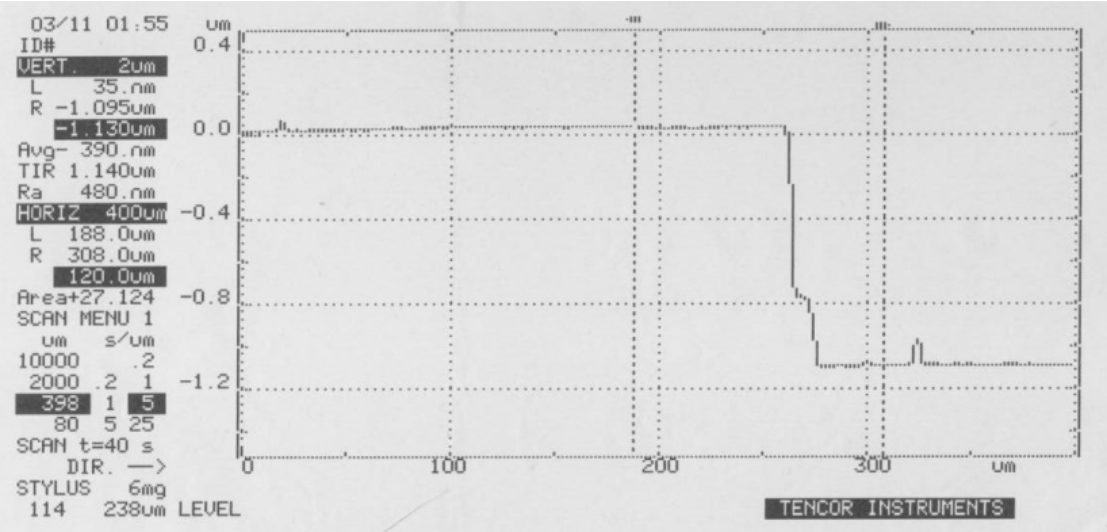

Figure 3-10 Thickness of HPR 504 film measured by Alphastep Profilometer

3.2.4 Prebake

The purpose of prebake is to reduce the solvent percentage in the resist film, typically from 20 to 40 percent down to 8 to 30 percent [82]. Generally speaking, after prebaking, the film thickness will be reduced and the adhesion property will be improved. In our case, substrates were baked in the oven for 30 minutes and the temperature was set to be 115ºC. After prebaking, the substrates were left on the cooling rack for 15 minutes, in order to let them cool down.

3.2.5 Exposure

Usually there are three types of lithographic printing methods: contact printing, proximity printing and projection printing. Contact printing makes the photomask directly contact the photoresist, offering a resolution down to about the wavelength of the radiation. Proximity printing keeps the photomask several tens of microns above the substrate to reduce mask damage, but resolution limit will be increased to several microns. Projection printing, commonly used today, places a lens between the photomask and substrate to project the image onto the photoresist. The resolution of this method follows the equation 3-1.

In NanoFab, the lithographic printing system uses the contact printing method, with UV illumination of 405 and 365 nm. Generally speaking, the resolution is limited to larger than 1μm. The exposure time we used was 2.4 seconds, which gave the smallest pattern in our case.

3.2.6 Development

When the substrate is exposed under UV illumination, the photoresist has to be developed to form a relief image. This development process is one of the most critical steps in the photolithography process. It has to be carefully controlled because both over-development and under-development may occur during the process. The relief image may be distorted, either larger or smaller than the one on the photomask. In the NanoFab, the developer used for HPR 504 is Microposit(TM) 354 developer, which is manufactured by Rohm and Haas Electronic Materials LLC. Table 3-3 lists the components of this developer. It was found that developing the HPR 504 photoresist for 17 seconds can get the best result in regard to the relief image.

Component	CAS-No.	Concentration
Water	7732-18-5	95.0-99.0 %
Sodium tetraborate decahydrate	1303-96-4	1.0-5.0 %
Sodium hydroxide	1310-73-2	0.1-1.0 %
Borate salt		0.0-1.0 %

Table 3-3 Components of Microposit(TM) 354 Developer

3.2.7 Wet etch

During the wet etch process, the etchant, a liquid chemical mixture, removes the part of the underneath film which are exposed to the etchant by chemical reaction, while the other part which are protected by the photoresist will remain intact. The pattern is consequently transferred from the photoresist to the thin film. However, one disadvantage for the wet etch is that it is an isotropic process. Since the etch rate is equal in all direction, undercutting of the etched film is unavoidable (Figure 3-11) and the thickness of the film being etched will be comparable to the lateral pattern dimension. Therefore, it is almost impossible to get a feature in sub-μm range by wet etch. In our case, the etch process was carefully controlled by putting the substrate into Cr etchant for 16 seconds and then washing it by DI water.

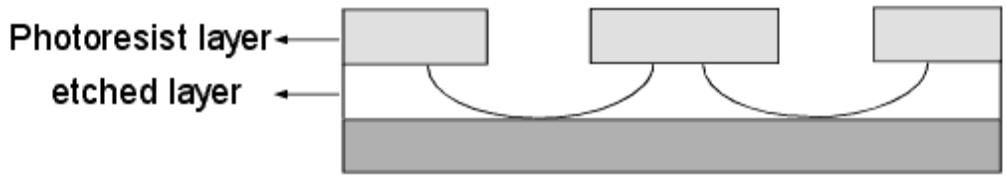

Figure 3-11 Isotropic etching leads to undercutting underneath the photoresist layer

3.2.8 Cleaning

This is the last step in photolithography process. First acetone and then isopropyl alcohol (IPA) were applied to remove the residue of the photoresist. The substrate was then washed by DI water and dried by nitrogen gun. By investigating the final substrate, it was found that the “1μm” pattern on the photomask was not successfully transferred to the donor substrate. However, the “2μm” pattern was successfully transferred, ending up as a 1.3μm disk on the donor substrate (Figure 3-12). The reduction of the size is due to the isotropic chemistry which occurred during developing and wet etching. Table 3-4 shows the summary of fabricating pre-patterned Cr micro-disks by photolithography, listing the parameters in each step during the whole process.

Procedure	Chemical	Equipment	Comment
Substrate cleaning	Piranha solution (mixture of Sulphuric Acid and Hydrogen Peroxide on the scale of 3:1)	Beaker, Teflon carrier	Piranha clean for 15 minutes
Sputtering	Chrome target	Bob Sputtering (a planar magnetron sputter system)	Deposited for 6 minutes to get a Cr film of ~80nm
Photoresist coating	HPR 504	Solitec spinner	Spread at 500rpm for 10 seconds and then spin at 4000rpm for 40 seconds to get a photoresist film of ~1μm
Prebake		Oven	Prebake at 115 ºC for 15 minutes
Exposure		Oscar mask Aligner (a standard contact mode mask aligner using UV illumination at 405 and 365 nm)	Expose for 2.4 seconds
Development	Microposit(TM) 354 developer	Container, Teflon tweezer	Develop for 17 seconds
Wet etch	Cr etchant	Beaker, Teflon tweezer	Wet etch for 16 seconds
Cleaning	acetone and isopropyl alcohol (IPA)	Teflon tweezer	Remove the photoresist residue

Table 3-4 Summary of pre-patterned Cr micro-disks fabricated by photolithography

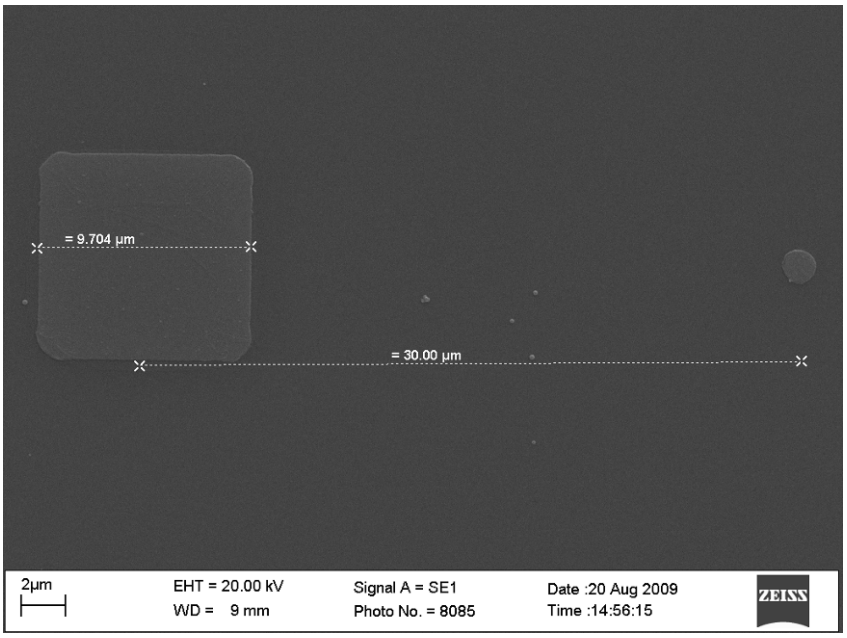

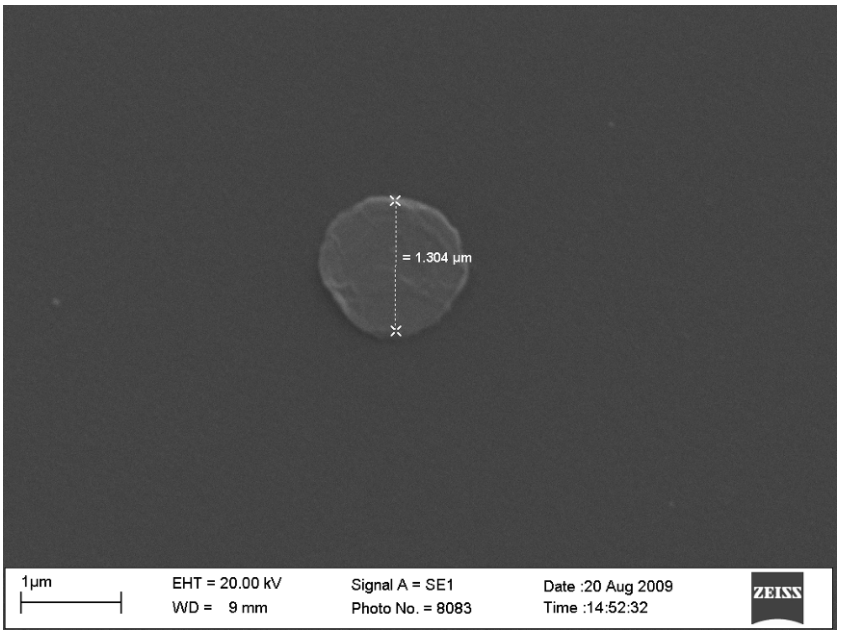

Figure 3-12 SEM image of the final donor substrate

3.3 Pre-patterned Cr sub-micron disks fabricated by E-beam lithography

3.3.1 Overview of e-beam lithography

The electron beam lithography, similar to photolithography, uses electrons instead of UV light to expose the resist and form a relief image on it. Given by the de Broglie equation, the wavelength of an electron is

$$\lambda = \frac{h}{p} = \frac{h}{\sqrt{2m_0 eU}} \qquad 3\text{-}3$$

where h is Plank's constant; p is the momentum of the electron; m_0 is the mass of the electron; e is the elementary charge and U is the electric potential. In e-beam lithography system, the electric potential is usually several thousands volts. Considering the relativistic effects, equation 3-3 becomes

$$\lambda = \frac{h}{\sqrt{2m_0 eU}} \frac{1}{\sqrt{1 + \frac{eU}{2m_0 c^2}}} \qquad 3\text{-}4$$

For a 20 kV electric potential, the wavelength of a single electron is 8.6×10^{-12} m (8.2 pm), which is thousands times smaller than that of the UV light used in photolithography. Therefore, the resolution limits of a single electron will be greatly improved based on equation 3-1. However, the scanning electron beam contains many electrons which would repulse each other. The balance of repulsion force between electrons and the focus ability of lenses results in features in the nanometer regime.

Though the structure of an e-beam lithography system is complex, it can be

classified into four parts in general: the electron optical column, mechanical systems, the computer and "control electronics", and software [92]. Electron optical column typically is the most important part, where the beam of electrons is focused by a set of electromagnetic lenses into a nanometer diameter spot, and it can be quickly steered by electromagnetic deflectors. In our case, the system used was Raith 150 EBL System, which is located in NanoFab at University of Alberta. The pre-patterned donor substrate fabrication by e-beam lithography was accomplished with the assistance of another graduate student Vince Sauer.

3.3.2 Lift-off technique

Lift-off technique was applied in e-beam lithography to produce the pre-patterned donor substrate with sub-micron patterns on it. Figure 3-13 illustrates the lift-off process steps. Resist PMMA 495 A6 was first spun on a cleaned glass substrate and resist PMMA 950 A2 was then spun on the first resist layer. Since PMMA 495 A6 is more sensitive to the electron beam, when the electron beam was scanning across the substrate, a larger portion of PMMA 495 A6 will be exposed than that of PMMA 950 A2. As the exposed resist was selectively removed by developer, an inverse T shape was formed along the two resist layers. When thermal evaporation was applied to conduct the deposition process, only a portion of material that was comparable to the size of the notch on PMMA 495 A6 can be deposited directly on the glass substrate. This deposition

was smaller than the notch in PMMA 950 A2 layer, making sure that when the resist was washed away, it would not affect the deposition and peel off the deposited material. Only the target material covering the residue resist will be washed out, leaving the material that was in the hole in contact with the donor glass substrate directly.

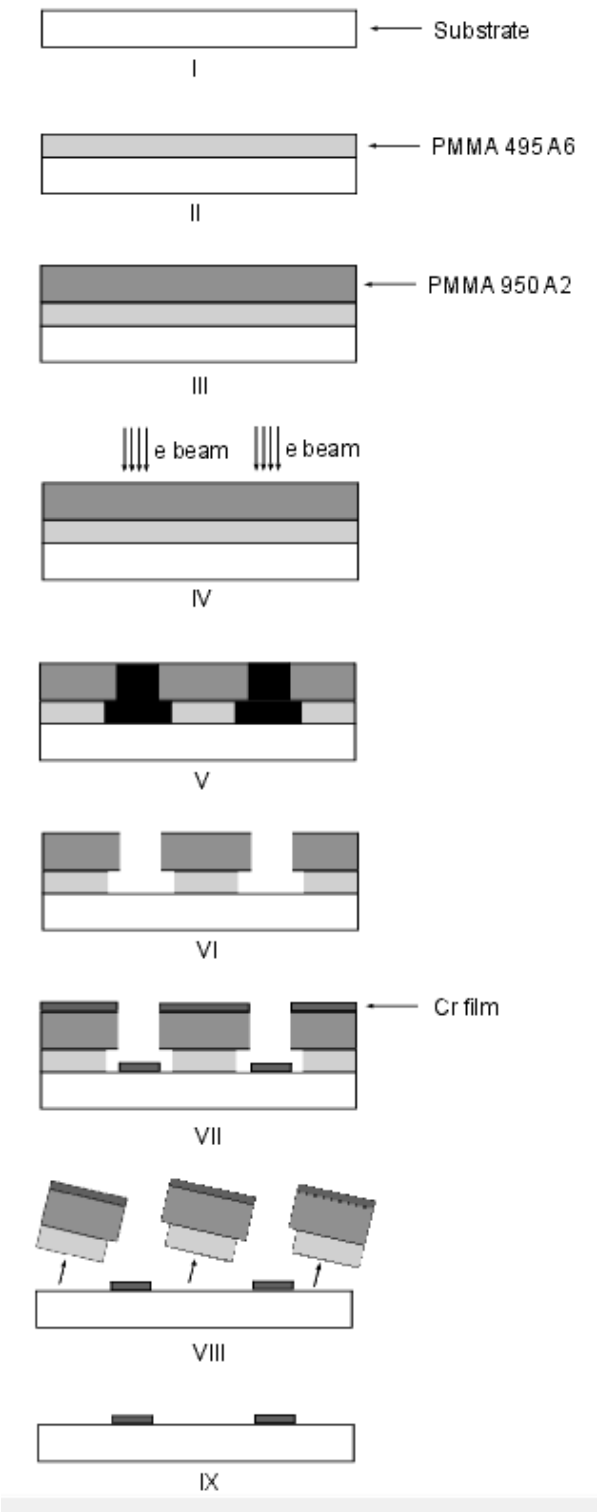

Figure 3-13 Lift-off process steps in e-beam lithography (I. Substrate preparation; II. PMMA 495 A6 resist coating; III. PMMA 950 A 2 resist coating; IV. Electron beam exposure; V. Creating inverse T shape; VI. Development; VII. Deposition; VIII. Washing out the residue resist; IX. Final pattern)

3.3.3 Pattern design and recipe

The pattern was generated by Raith EBL software, which can be directly transferred to Raith 150 EBL System to perform the e-beam lithography process. Figure 3-14, 3-15 and 3-16 show the details of the Cr pattern, where the big 10μm disk was still designed to be the marker and 0.5μm disk is the one that will be transferred during the LIFT process.

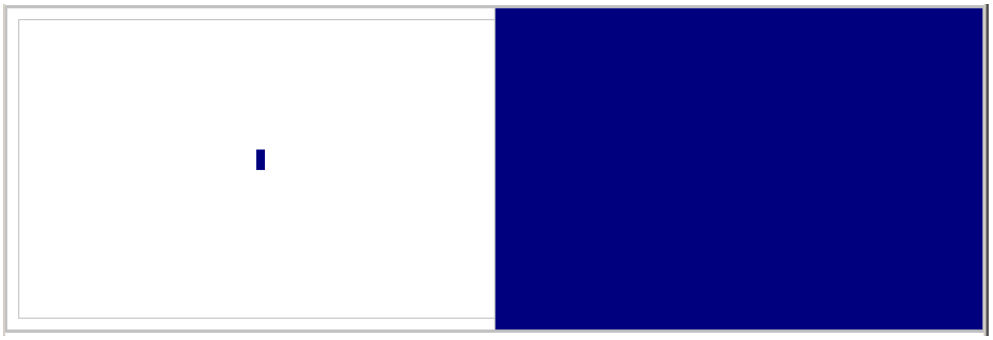

Figure 3-14 Overall view of 1"x3" microscope slide. Dark area is Cr

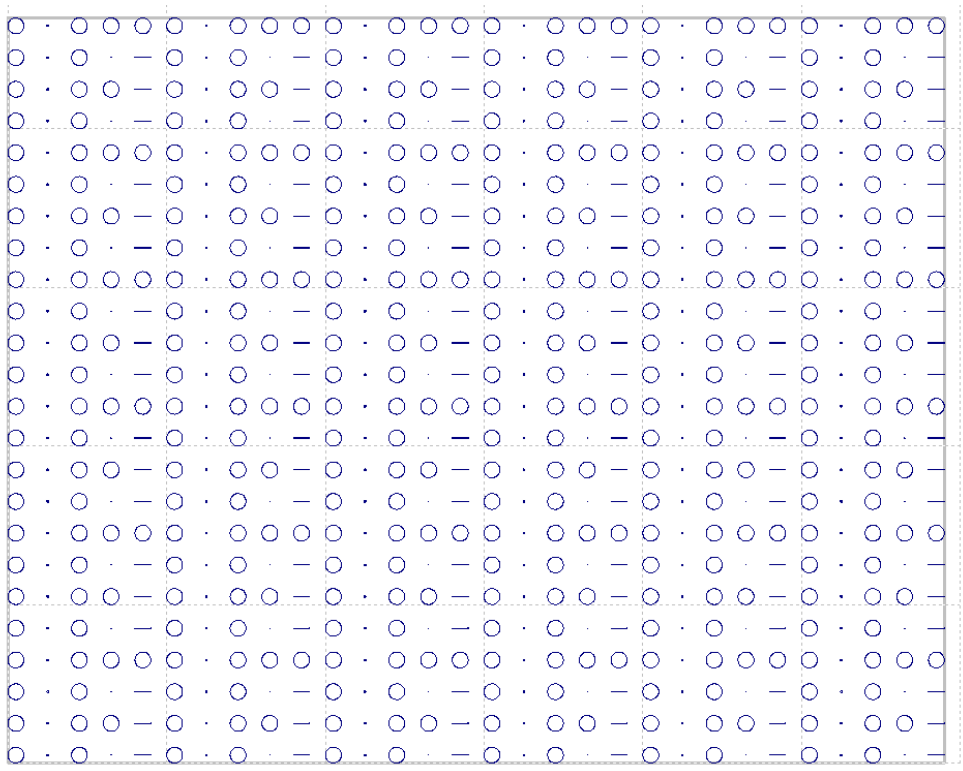

Figure 3-15 Zoomed view of Cr pattern

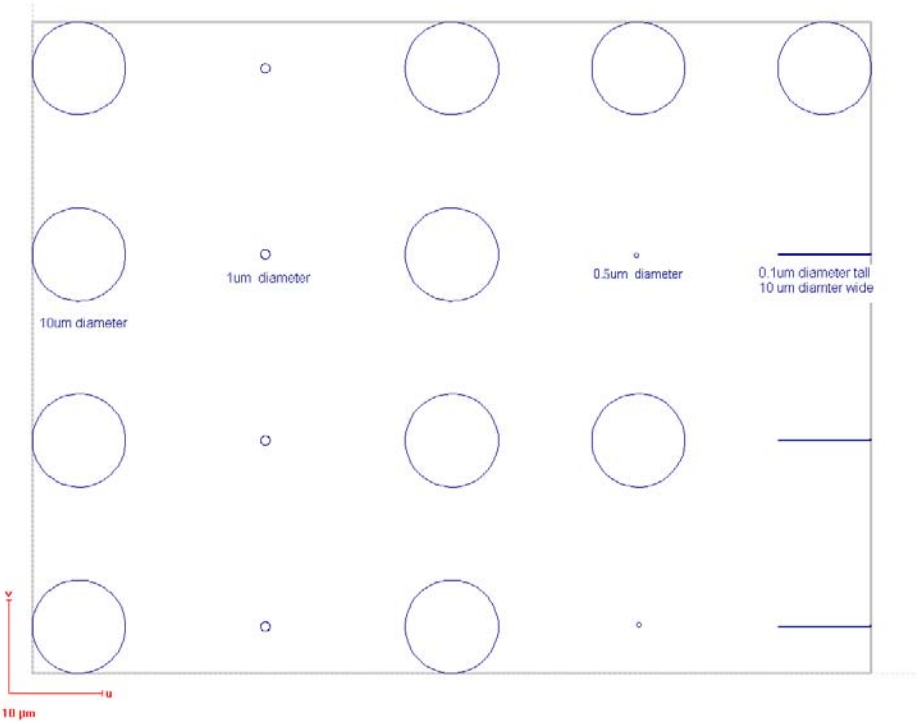

Figure 3-16 Zoom view of Cr pattern. This is the basic cell that is repeated in Figure 3-15

Following is the recipe applied in the e-beam lithography process.

1) Clean microscope slide (25×75×1.0mm) with Piranha solution.
2) Dehydrate sample for 5 min on 200ºC hotplate.
3) Spin PMMA 495 A6 as follows
    a. Spread 500rpm: acceleration=2 s, time=5 s
    b. Spin 4000rpm: acceleration=5 s, time=30 s
4) Bake at 200 ºC for 30 min
5) Spin PMMA 950 A2 as follows
    a. Spread 500rpm: acceleration=2 s, time=5 s
    b. Spin 4000rpm: acceleration=5 s, time=30 s
6) Bake at 200 ºC for 30 min

7) Expose sample in Raith using the following parameters:
    a. 10 kV acceleration
    b. 10μm aperture
    c. 50 μC/cm^2 area dose, 0.020μm step size
    d. Set dose factor to 1.2 (instead of 1.0) when writing
8) Develop sample as follows:
    a. 1:3 MIBK:IPA solution for 60 s (develop)
    b. IPA solution for 20 s (develop stop)
    c. DIW solution for >15 s (rinse)
9) Descum sample using the μEtch RIE with the following recipe:
    a. Pressure 67 mTorr
    b. 20% O2 flow
    c. 16.6% RF power
    d. 6 s
10) Deposit 80 nm of Cr onto sample using thermal evaporation
11) Sonicate sample in acetone for ~15 min, until all the Cr where resist was is gone

Chapter 4

Results and discussion

4.1 LIFT from continuous Cr film

4.1.1 Focal spot determination

In the LIFT process, the laser pulse has to be focused in order to get a small spot and high fluence. The unfocused beam was measured by the knife-edge technique. Figure 4-1 shows this technique. A blade is placed before a photo-detector. As the blade scans perpendicularly across the beam's axis of propagation, a photo-detector measures the intensity of the unmasked portion of the beam and the measured signal continuously decreases to zero. The signal is then differentiated to obtain the beam profile [94]. The laser intensity collected from the beam was plotted in Excel as a function of the knife edge position, shown in Figure 4-2. The following equation was obtained after 6^{th} order polynomial fit:

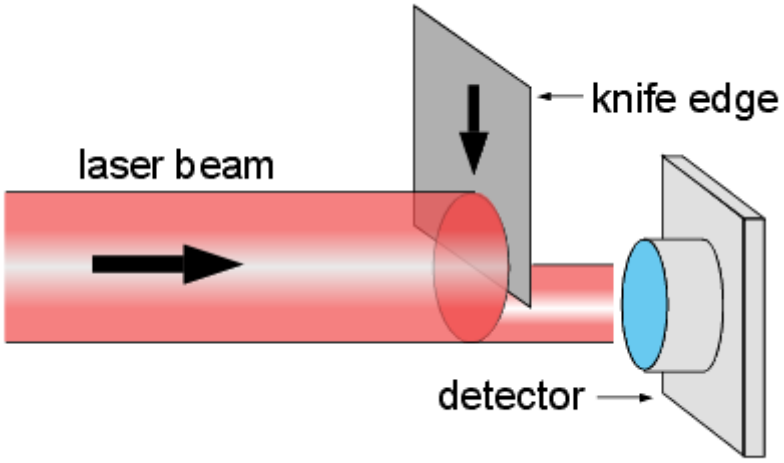

Figure 4-1 Knife edge technique

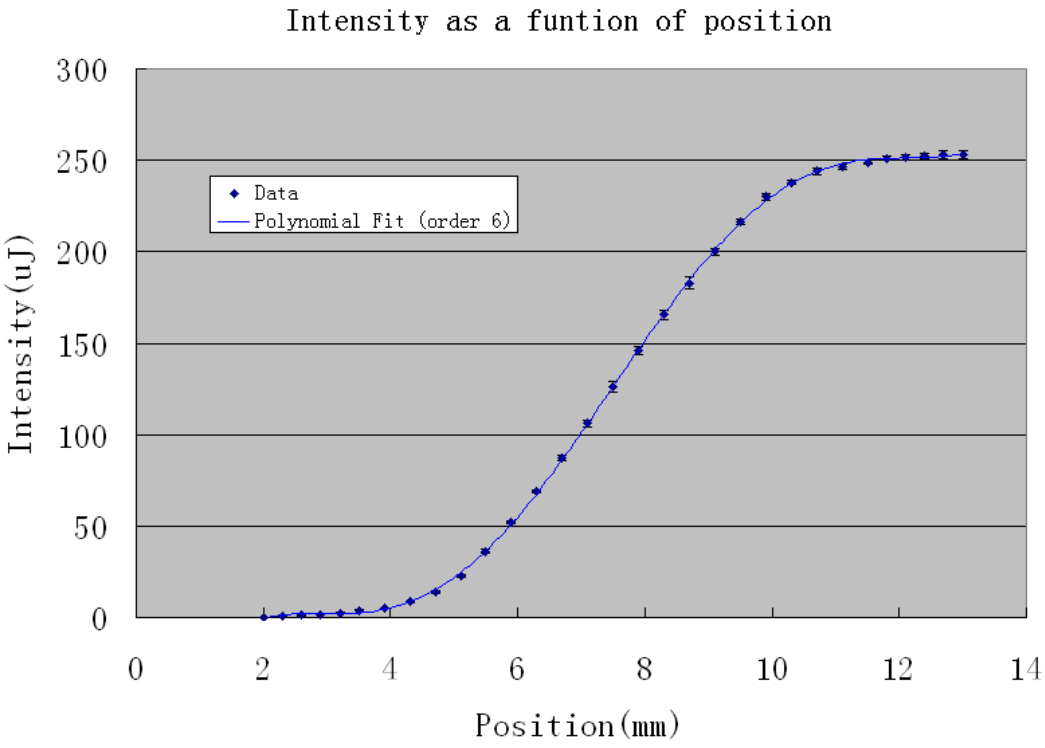

Figure 4-2 Laser intensity measured by knife edge technique as a function of position

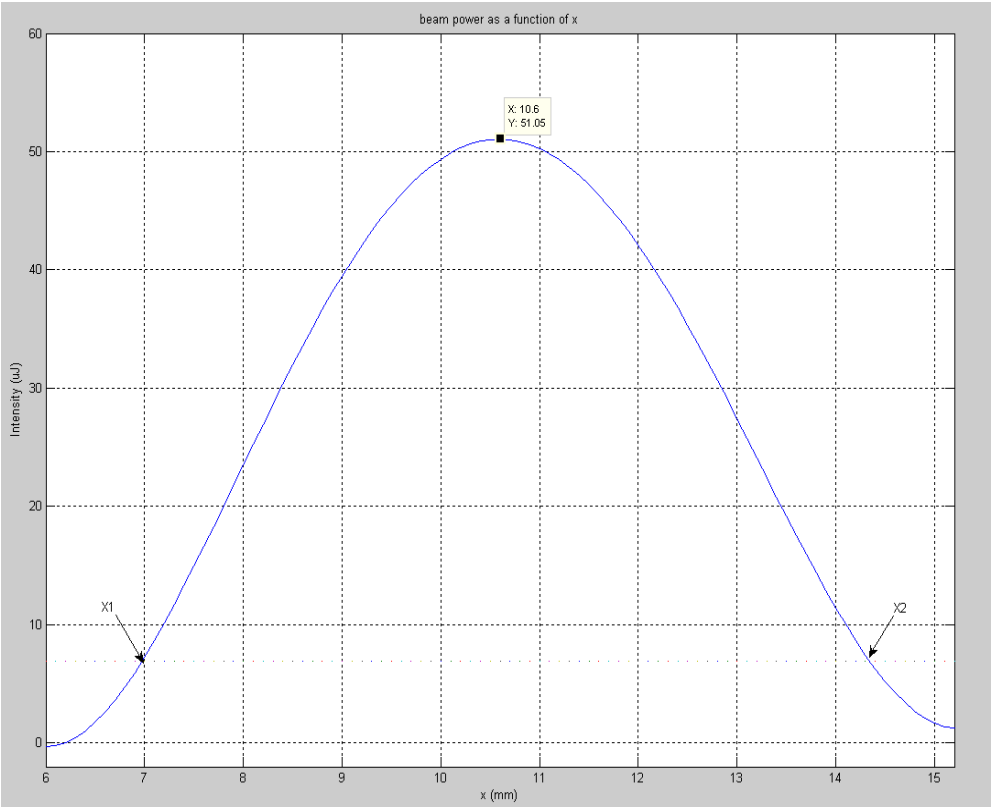

Figure 4-3 Gaussian fitting

$$y = -1710.04907 + 1055.11995\ x - 249.02877\ x^2 + 27.95501\ x^3 - 1.50497\ x^4 + 0.03435\ x^5 - 1.8216E\text{-}4\ x^6 \quad 4\text{-}1$$

Theoretically, this should be an airy function and the 6th order polynomial fit was chosen for convenience only. By differentiating eqn. 4-1, it became:

$$y = 1055.11995 - 2*249.02877\ x + 3*27.95501\ x^2 - 4*1.50497\ x^3 + 5*0.03435\ x^4 - 6*1.8216E\text{-}4\ x^5 \quad 4\text{-}2$$

Figure 4-3 was plotted in Matlab showing the unfocused Gaussian profile of the laser beam. x_1 and x_2 indicate the position of $1/e^2$ of the peak intensity value. The e^{-2} intensity beam waist of the unfocused laser beam was measured to be 7.4mm.

In our experiment, a 0.25 N.A. 10X microscope objective was used. Its focal length is around 16mm, the f-number f#=f/D=16/7.4=2.16. Since the wavelength of laser was 800nm, the theoretical focused spot radius for a perfect Gaussian beam would be $w_0 = (1.33/2)*f\#*\lambda = 0.665*2.16*0.8 \approx 1.2\mu m$.

The Gaussian Beam Limiting Technique (GBLT) was used for in situ measurements of pulsed Gaussian-beam focused on the donor film [72], as described in the previous chapter. Starting from the electric field distribution of a Gaussian beam spatial profile, an equation was obtained.

$$D^2 = 2w_0^2 \left\{ \ln\left(E_{pulse}\right) - \ln(E_{th}) \right\} \qquad 4\text{-}3$$

where D is the damage spot diameter, w_0 is the e^{-2} intensity beam waist radius, E_{pulse} is the pulse energy, and E_{th} is the ablation threshold energy. Using this equation, a semi-logarithmic plot of the squared damage diameters against the pulse energy can be obtained. The e^{-2} intensity beam waist radius can be obtained

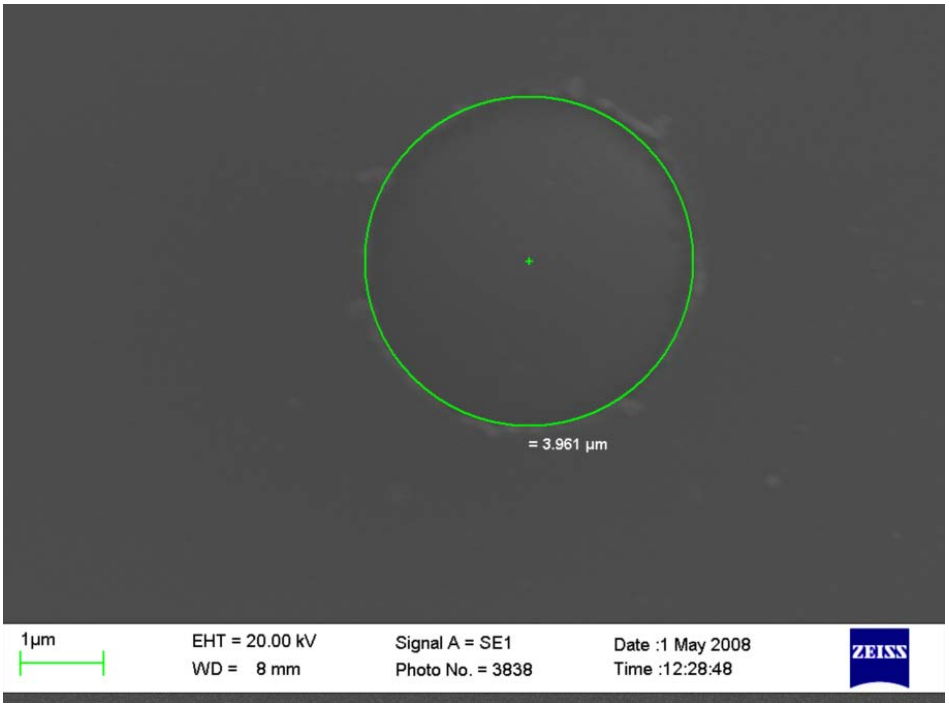

Figure 4-4 SEM image of ablation on the 80nm Cr film

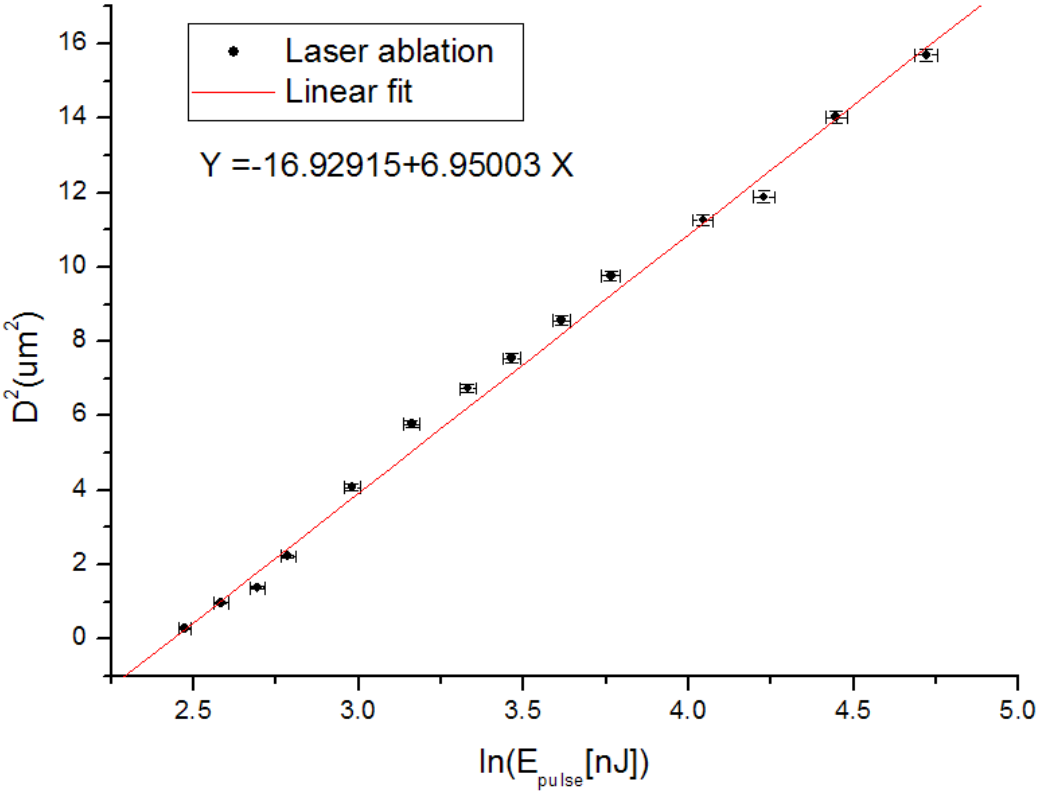

Figure 4-5 Semi-logarithmic plot by GBLT

from the slope of the polynomial fit. The energy threshold can also be obtained from the intersection of the fitted line and the horizontal axis. Figure 4-4 shows a sample of SEM image of ablated spot on the 80nm Cr film when laser energy was 112nJ. The laser beam was focused by the 10X microscope objective. The diameter of this ablated spot was around 4μm. The semi-logarithmic plot is given in Figure 4-5, where x axis is $\ln(E_{pulse})$ and y axis is D^2. After applying linear fit, the relationship Y=-16.92915+6.95003X was obtained. Comparing this with eqn. 4-3, it was found that $2w_0^2$ was equal to 6.95 μm^2, giving w_0 to be around 1.86μm. This is about 30% larger than the theoretical focal spot radius calculated before. This is not unreasonable given the laser beam and optical alignment in the experiment may not be perfect.

4.1.2 Ablation threshold measurement

Threshold behavior, as reported before for gold thin films [95] was also observed here. Two threshold fluences, namely ablation threshold fluence and transfer threshold fluence, may exist for LIFT. The ablation threshold fluence, at which the donor Cr film can be ablated, was found to be 0.21 J/cm^2 using eqn.4-3 as described in section 4.1.1. Figure 4-6 and Figure 4-7 show the ablation dots on the 80nm Cr film of donor substrate under different fluence. The sizes of the ablated dots became smaller as the fluences went down. When the fluence was as low as 0.219 J/cm^2, there were still holes that were ablated by single shot, presented in line 30. However, when the fluence dropped down to 0.203 J/cm^2, only multiple shots would create ablated hole on the donor film due to incubation

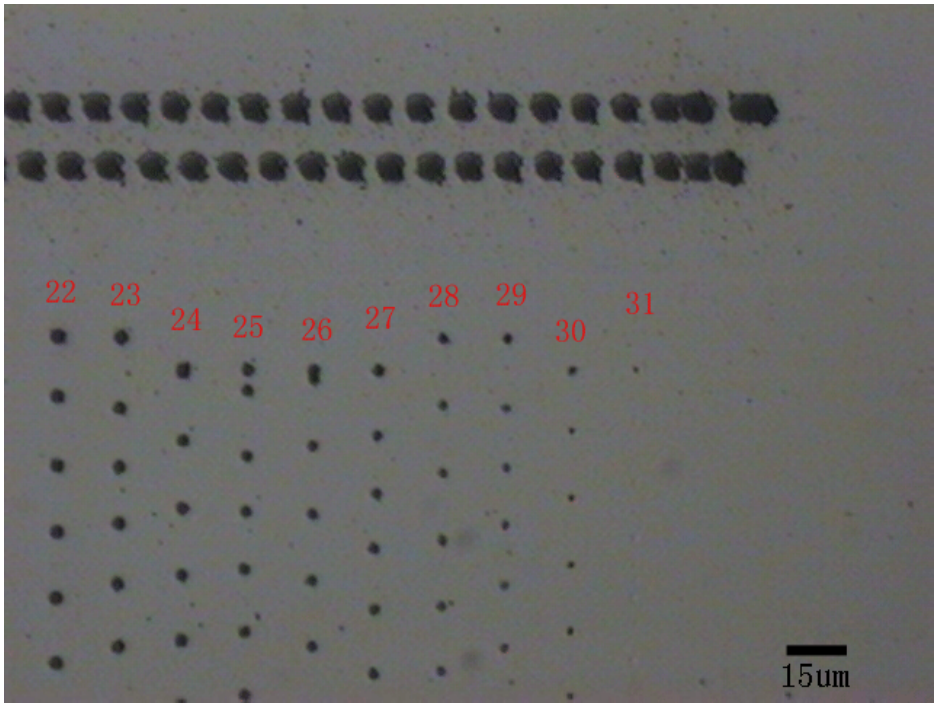

Figure 4-6 Ablated holes on continuous Cr film (optical microscope, 25X)

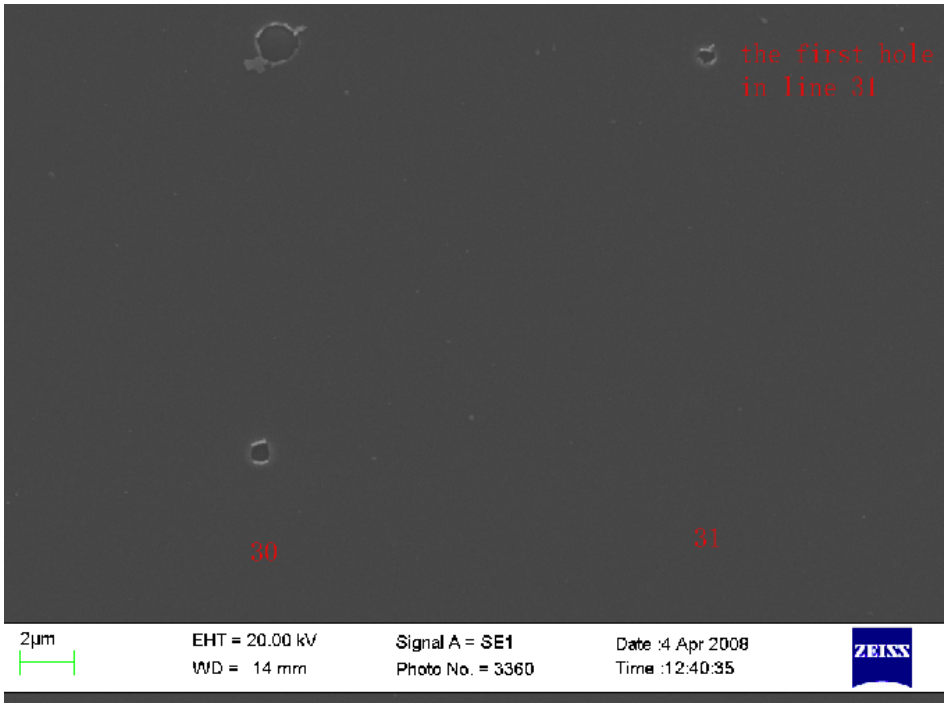

Figure 4-7 SEM image of ablated holes on continuous film (lines 30 and 31, the first hole in line 31 was due to accumulation of multiple shots and there is no ablation caused by single shot in line 31)

effect [96] and single shot did not lead to ablation (see line 31 on Figure 4-7). Thus, the ablation threshold is considered to be between 0.203 J/cm^2 and 0.219 J/cm^2, which is consistent with the around 0.21 J/cm^2 ablation threshold obtained using the GBLT.

4.1.3 Transfer threshold measurement

Transfer threshold is measured here by inspecting the transferred material on the acceptor substrate, which is presented in Figure 4-8. Image (a) shows the overall view of the pattern, where the 80nm Cr continuous film was transferred

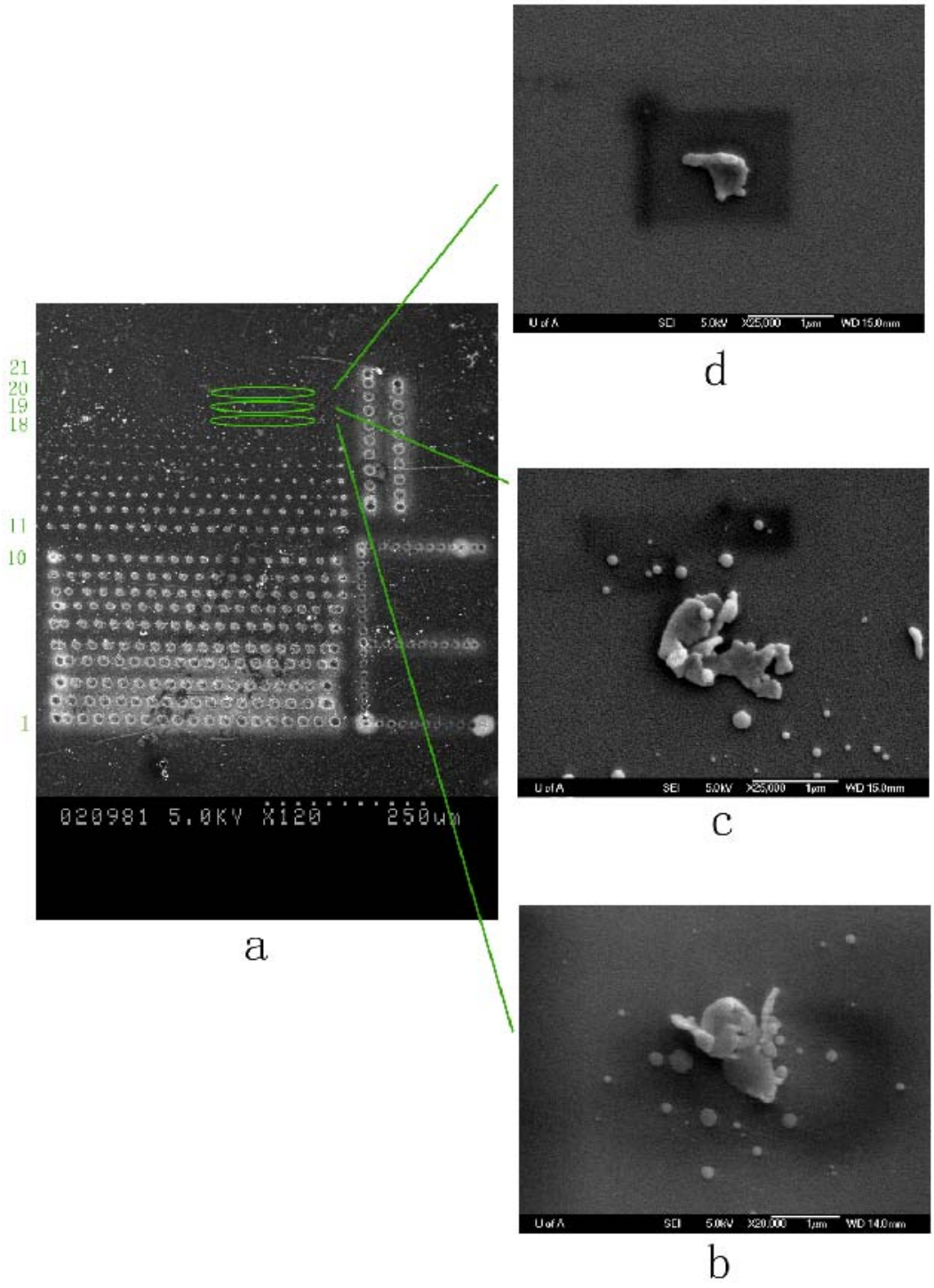

Figure 4-8 SEM images of transferred dots from 80nm continuous Cr film (a, whole pattern; b, F = 0.26 J/cm^2; c, F=0.24 J/cm^2; d, F=0.22 J/cm^2)

under different fluence, from 18 J/cm^2 gradually down to 0.213 J/cm^2. The dots on each line were transferred under the same fluence. For example, dots on line 1 were transferred under 18 J/cm^2, while dots on line 21 were transferred under 0.213 J/cm^2. The XYZ micro-positioning stage was moved at 80μm/s and the laser repetition rate was set to be 2 Hz. The transferred dot became smaller as the fluence decreased. When the fluence was at 0.22 J/cm^2, slightly above the ablation threshold, the transferred material became very small, occupying an area of around 700 nm and unlike those transferred at high fluences it was debris free (image (d)). However, when the fluence dropped down to 0.213 J/cm^2, just around the ablation threshold, there was no material successfully transferred on the acceptor substrate. Thus, the transfer threshold fluence was considered to be around 0.22 J/cm^2, which was slightly larger than that of ablation threshold.

It is expected the transfer threshold fluence should be higher than that of ablation threshold. The Cr material is transferred from the donor substrate onto the acceptor substrate when the focused laser pulse causes the formation of vapor at the film substrate interface and ejects a portion of the film in a rocket-like motion at high speed. As the fluence approaches the ablation threshold, at a certain point, the fluence becomes too low to produce enough thrust to peel off the Cr material and push it through the air gap onto the acceptor substrate. However, the fluence is still high enough to melt a tiny portion of Cr film. This melted material just accumulates around the ablated spot on the donor substrate, without being successfully transferred. Figure 4-9 shows the ablation of the Cr film when

fluence is 0.213 J/cm^2, around the ablation threshold.

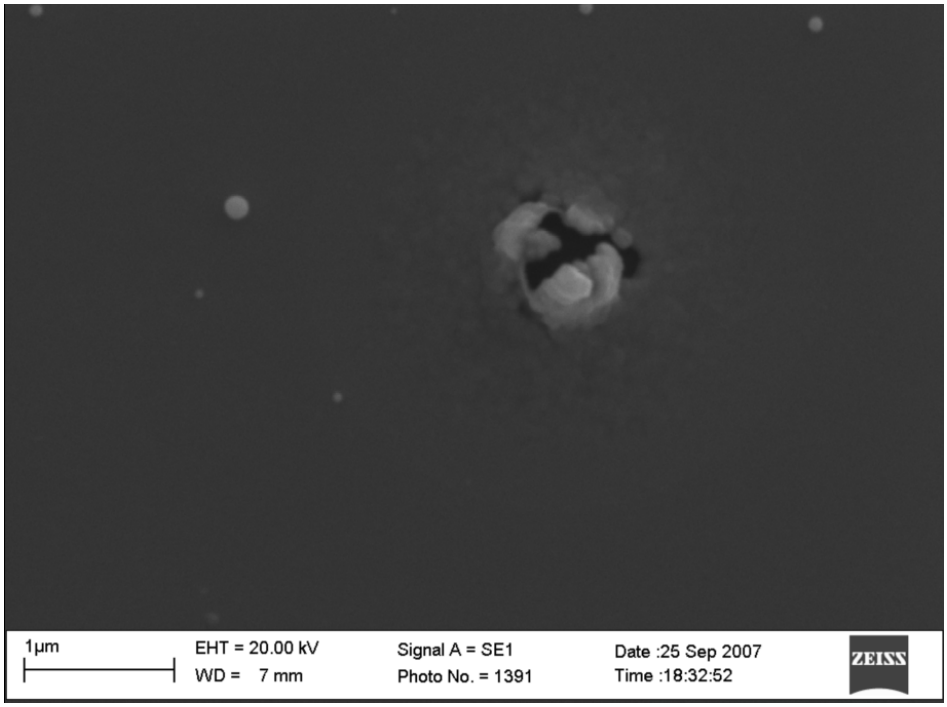

Figure 4-9 The ablation of 80nm continuous Cr film on donor substrate when fluence is 0.213 J/cm^2

4.1.4 Morphology of the transferred material

The transferred material presented different morphologies depending on the range of laser fluences applied. Firstly, at fluences near the transfer threshold, the majority of the spot was transferred as an intact spot with negligible debris around the transferred piece (Figure 4-10 a). Secondly, at fluences several times above the transfer threshold fluence, the material was transferred consisting of many patches with size on the order of a few hundred nm and significant amount of debris was also observed (Figure 4-10 b). As the fluences continued to increase to an order of

magnitude above the transfer fluence, ring-like transferred pattern was observed and the amount of debris further increased (Figure 4-10 c). It was suggested that at such high fluence the centre of the pattern is too hot to effectively bond to the acceptor substrate [97].

The adhesion of the transferred material from continuous film bonding to the acceptor substrate was studied by a scotch-tape test. A scotch-tape was first taped on the acceptor substrate having transferred material on it and it was then peeled off. It was found that after the scotch-tape was peeled off, the transferred material was still on the acceptor substrate.

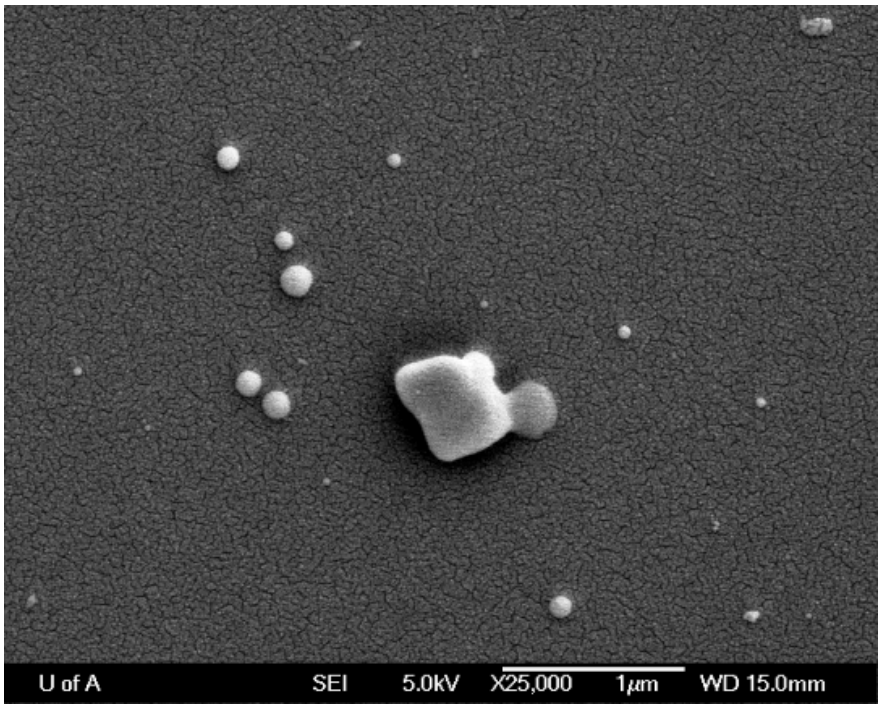

a

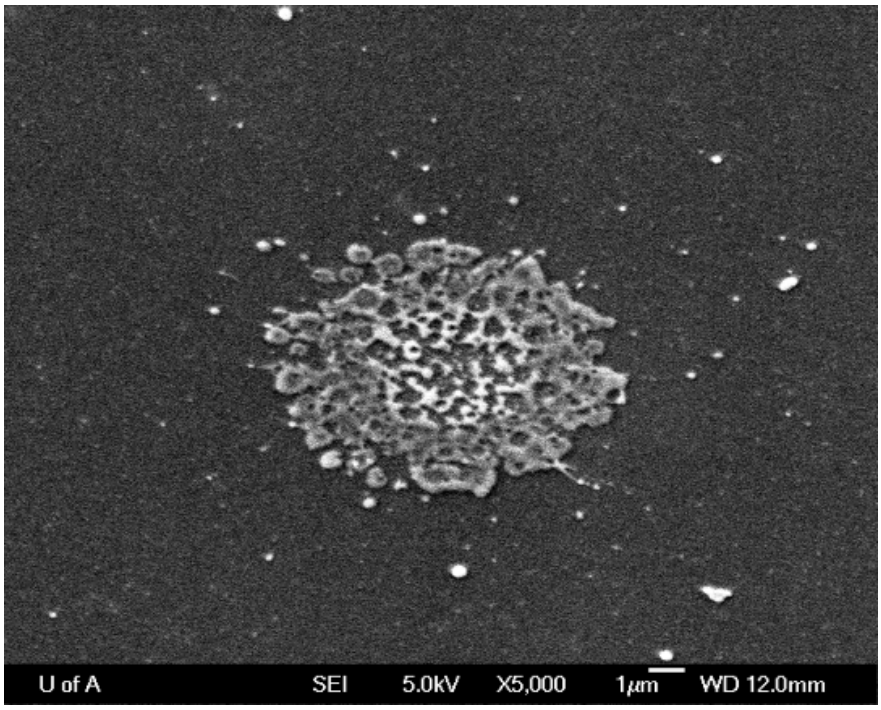

b

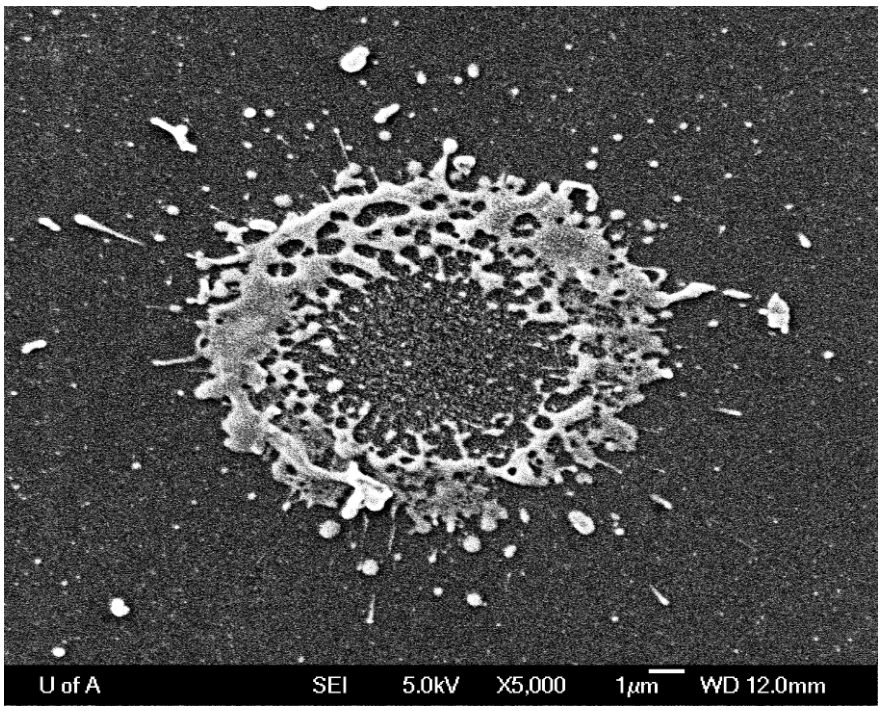

c

Figure 4-10 Comparison of different morphology of the transferred material at different fluence (a, F = 0.23 J/cm^2; b, F=2.0 J/cm^2; c, F=15.9 J/cm^2)

It is found that the sizes of transferred material from continuous Cr film depend on the fluences (Figure 4-11). The effective diameters of the disk-shaped transferred material rapidly increase from below 1 μm to ~7 μm for a range of fluences from ~0.22 J/cm^2 to ~2 J/cm^2. The increase in effective diameters of the transferred material for fluences from ~2 J/cm^2 to ~18 J/cm^2 was relatively small and the diameter was ~10μm at ~18 J/cm^2.

Though the material can be successfully transferred from continuous film, there are several disadvantages. At high fluences the transferred material becomes very broken up, is large in size and there are lots of debris around the transferred material. At very low fluences close to the transfer threshold, the size of the LIFT dots can be reduced to around 700 nm in our case. However, the size and shape of the transferred material would be different each time because the LIFT process is very sensitive to the fluctuation in laser fluence when it is close to the transfer threshold. Note the diameters of the LIFT dots decrease rapidly when the laser fluences are below 2 J/cm^2. From Figure 4-8 (b), (c) and (d), it is observed by changing the fluence in steps of only 0.02 J/cm^2, the resulted transferred dots were very different.

The reported smallest droplet that was deposited by LIFT from continuous film was around 300nm [56, 59]. In our experiment, the smallest LIFT dot from continuous Cr film was around 700nm, larger than those in refs 56 & 59. One possible reason is that the film they used was much thinner at 30nm. In their case the whole film would be melted and sub-micron droplets would form and be

ejected by the laser on the acceptor substrate. In our case, the film used was much thicker (80nm thick) and only a portion of the film would be melted and vaporized. This hot material would act as rocket fuel to propel the material onto the acceptor substrate. The differences of these two processes are shown schematically in Figure 4-12 [59]. This picture is in agreement with the numerical simulation results describe in the next section.

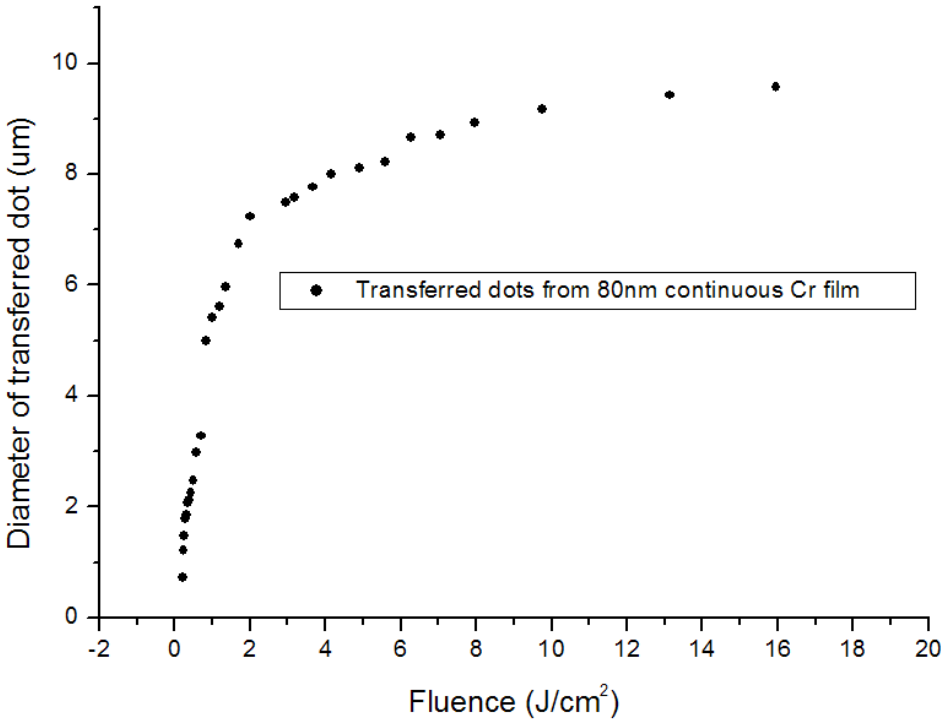

Figure 4-11 Diameters of transferred Cr dots versus fluences

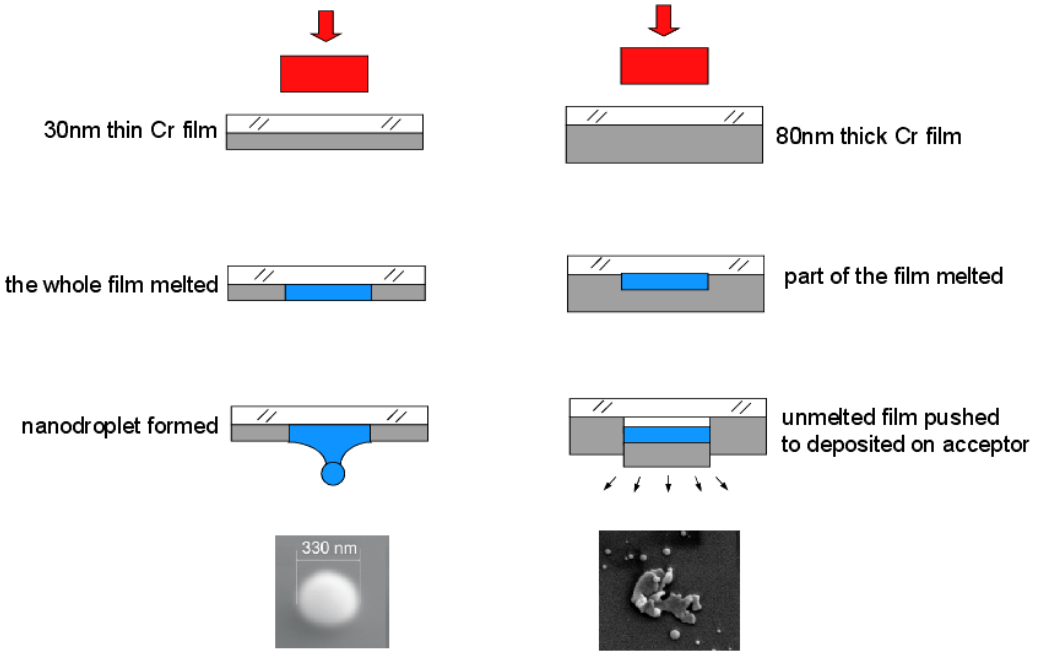

Figure 4-12 Schematic of LIFT from a 30nm thin Cr film (left) and 80nm thick Cr film (right) [59]

4.1.5 Two temperature model results

As described in Chapter 2, the two-temperature model (TTM) is commonly used to model the heat transfer inside a metal heated by a laser pulse. In this project, the two-temperature heat diffusion equation was solved in Matlab environment [98]. The parabolic two-step model and Gaussian pulse shape were selected. The conductivity was set to be plasma and the absorption was chosen to be normal. The parameters of Cr used in the program have been discussed in Chapter 2, which are listed in Table 4-1, where g is the electron-lattice coupling constant, C_i the lattice volumetric heat capacity, T_{melt} the melting temperature of Cr, T_{boil} the boiling temperature of Cr, γ the constant of electron heat capacity, κ_0

the constant of electron thermal conductivity, χ and η the plasma electron thermal conductivity parameters of Anisimov's model, T_F the Fermi temperature, τ_F relaxation time, R the normal incidence reflection. The index of refraction n, the extinction coefficient k, and the normal incidence reflection R as a function of photon energy E were obtained from CRC Handbook of Chemistry and Physics [71].

Metal	g(W/m^{3}K)	C_i(J/cm^{3}K)	T_{melt}(K)	T_{boil}(K)	γ(J/m^{3}K^2)	κ_0(W/mK)
Cr	4.2×10^{17}	3.24	2180	2944	194	94

Metal	χ(W/mK)	η	T_F(K)	τ_F(s)	R
Cr	300	0.20	8.01×10^4	3×10^{-15}	0.634

Table 4-1 The parameters of Cr used in TTM code [62] [68] [69] [70] [99]

Two-temperature model results are shown in Figure 4-13 and Figure 4-14. It is found that when the absorbed laser fluence Φ^{abs}_{pk} = 33mJ/cm^2, the lattice temperature at the surface of chrome reaches its maximum point at around 3.5 ps, which was equal to 2181.9K, close to the chrome's melting temperature (2180K), as shown in Figure 4-13. In the simulation, the absorbed fluences were used. Since the theoretical normal incidence reflection of chrome is 0.634, the actual incident fluences can be obtained by dividing by 0.366. With an absorbed fluence of 33 mJ/cm^2, the actual incident laser fluence was calculated to be 90.2 mJ/cm^2. This is

less than the ablation threshold from our experiment, because at this fluence, only a very thin layer on the interface reaches melting temperature, which can not produce enough thrust to propel a portion of 80nm Cr film away from the donor substrate. As a result, no ablation would occur, as shown in Figure 4-15 (a). When the absorbed fluence Φ^{abs}_{pk} = 77mJ/cm^2, giving the actual laser fluence to be 210.4 mJ/cm^2, the simulation result shows that the surface reaches its maximum temperature at around 5 ps, which is well above the boiling temperature and a layer portion of the film (~40 nm) reaches the melting temperature. In this case, enough thrust might be produced to propel a small portion of material away from the donor substrate, as more material is melted. Thus, the ablation occurs at the surface of the Cr film, as illustrated in Figure 4-15 (b). In real case, the actual reflectivity could be lower than the theoretical normal incidence reflection, giving a slightly higher absorptivity. Thus, the temperature at the surface might be even higher than the simulated results have shown. For the case with absorbed laser fluence of 77 mJ/cm^2, it is worth to point out that around 40 nm (larger than 30 nm but smaller than 80 nm) of the film was melted which is consistent with the picture that was described in the previous section.

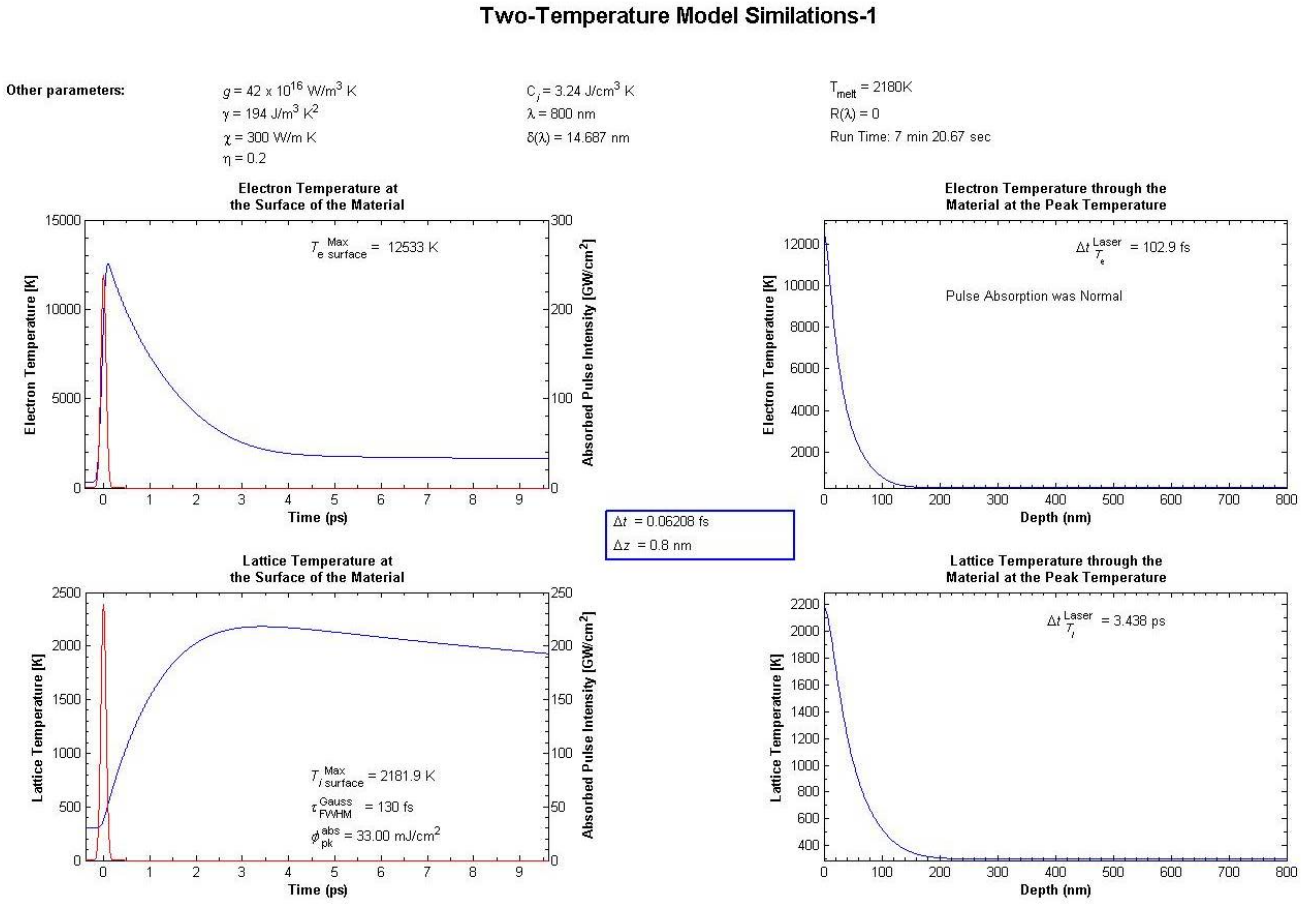

Figure 4-13 TTM programming result when the incident fluence $\Phi^{abs}_{pk} = 33 mJ/cm^2$

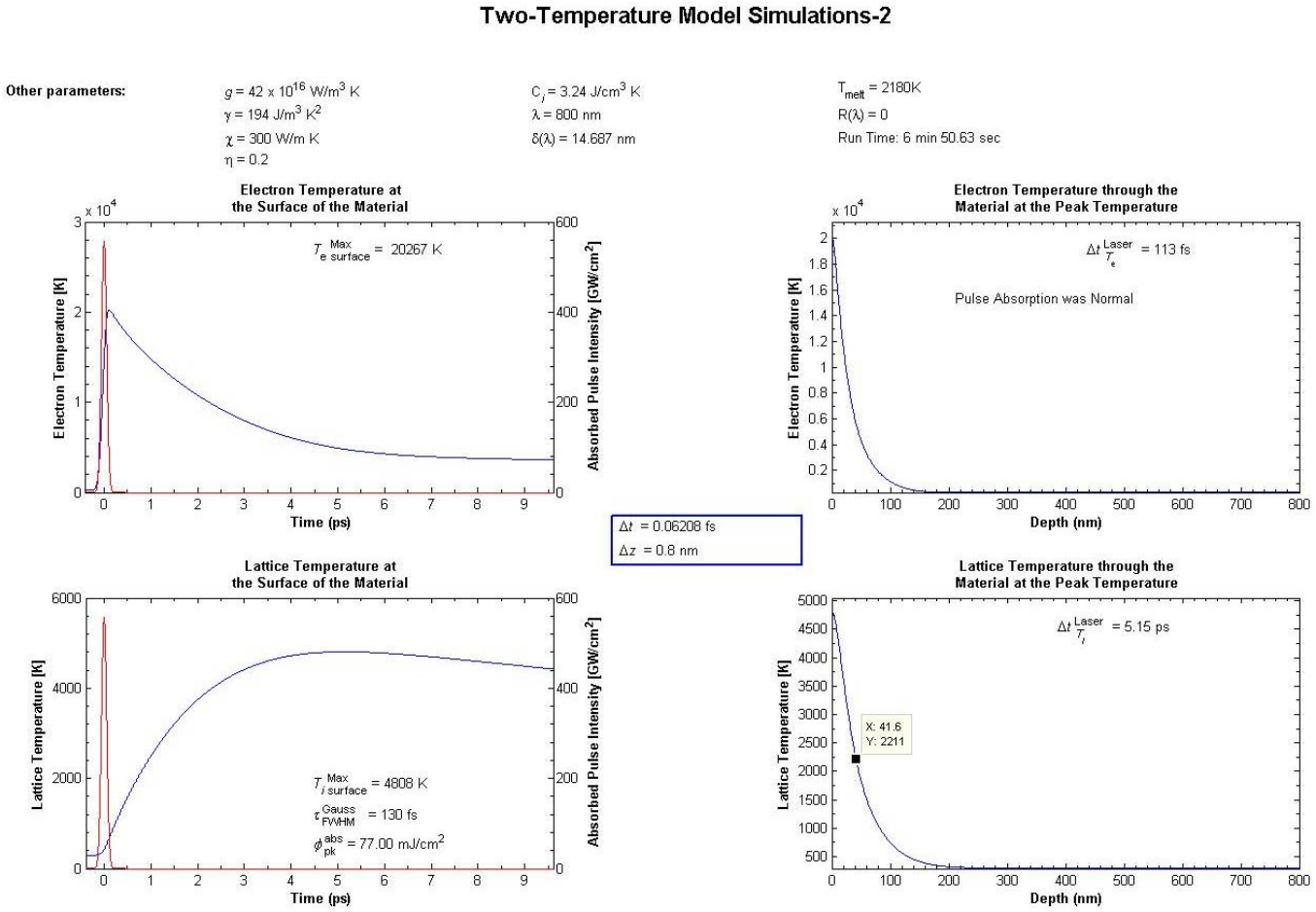

Figure 4-14 TTM programming result when the incident fluence $\Phi^{abs}_{pk} = 77 mJ/cm^2$

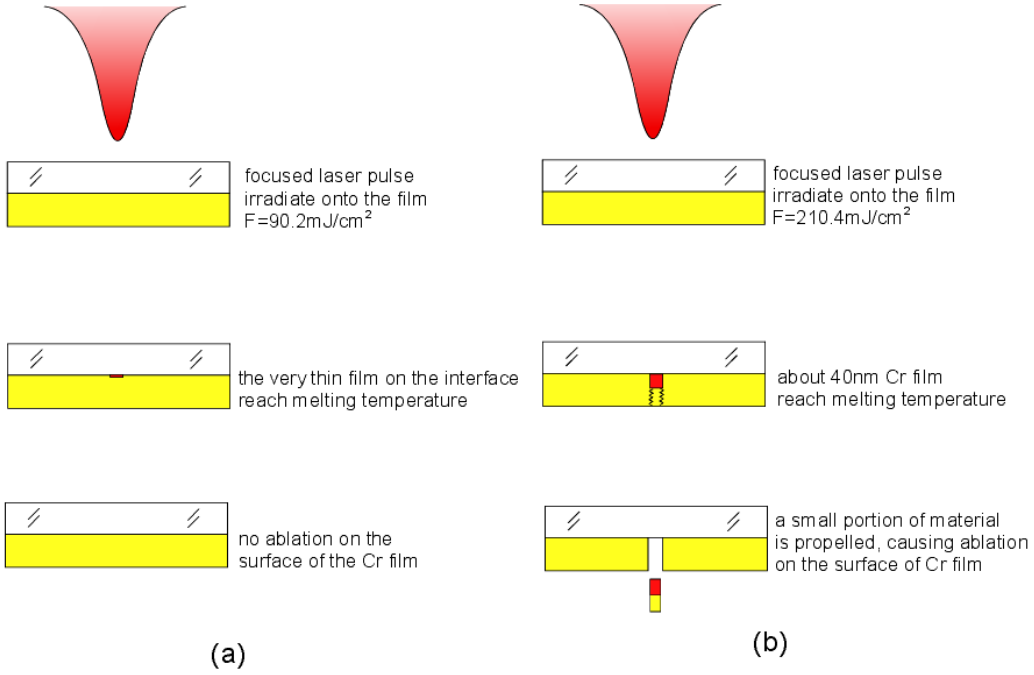

Figure 4-15 Illustration of ablation process at ablation threshold

4.2 LIFT from pre-patterned micro-sized Cr disk

4.2.1 Best focus condition

By using photolithography, alternative rows of 10 μm squares and 1.3 μm diameter Cr micro-disks were fabricated on the donor substrates (Figure 3-12). The laser beam was then focused on top of these disks to transfer them onto the acceptor substrate.

The best focus condition was first used to transfer the 1.3 μm disk and the optical microscopy image of these LIFTed micro-disks is shown in Figure 4-16. The morphology of LIFT micro-disks with different laser fluences was

investigated with SEM (Figure 4-17-1). At fluences ~2 J/cm^2 ten times above the threshold fluence, the micro-disks were broken up into many pieces with sizes on

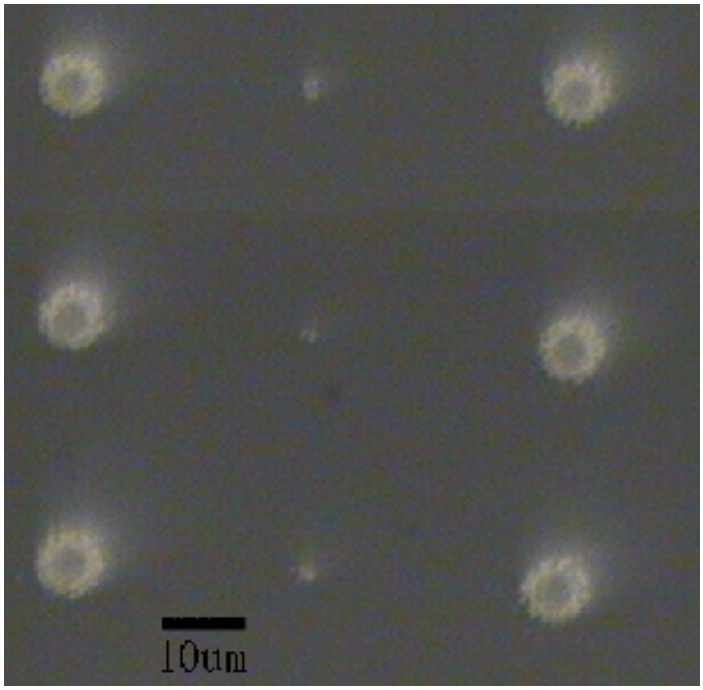

Figure 4-16 Optical microscopy image of LIFT micro-disks on acceptor substrate

the order of hundred nanometers. These pieces occupied an area of about 2 μm. Significant amount of debris was observed (Figure 4-17-1 a). At lower fluences ~1 J/cm^2 several times above the threshold fluence, the micro-disks were mostly intact but became slightly porous after the LIFT process. These LIFT micro-disks occupied an area of about 1.4 μm slightly larger than the size of the original donor pattern. Reduced amount of debris was also observed (Figure 4-17-1 b). At fluences ~0.6 J/cm^2, the material appeared to be melted and resolidified and then deposited onto the donor substrate and it appeared to be non-porous (Figure 4-17-1 c). As fluences went down to ~0.4 J/cm^2, the pre-patterned disk was

transferred in the form of several big pieces (Figure 4-17-1 d). As fluences further reduced down to ~0.3 J/cm^2, close to the ablation threshold, the micro-disks were slightly winkled but mainly remain intact after the LIFT process. These LIFT micro-disks occupied an area of about 1.2 μm slightly smaller than the size of the original donor pattern. Neglectable amounts of debris were observed in this case (Figure 4-17-1 e). As illustrated in Figure 4-17-2, the very thin micro-disks were traveling through air propelled by the vapor created by the laser pulse in a rocket-like motion. Since the 1.3μm pre-patterned disk has a similar size as the focal spot, the intensity profile of the Gaussian laser spot would lead to a non-uniform force profile on the disk and thus could cause the deformation of the thin molten micro-disk. Further studies are required to fully understand this phenomenon. As the fluence continued to decrease, only a small piece of material was observed to be transferred. This may be because at the fluences near threshold value, the ablation spot (defined by a circular region that has fluences equal or above the ablation fluence) would be smaller than 1.3 μm (see Table 4-2), the diameter of the microdisk target, thus only a portion of the micro-disk target would get transferred.

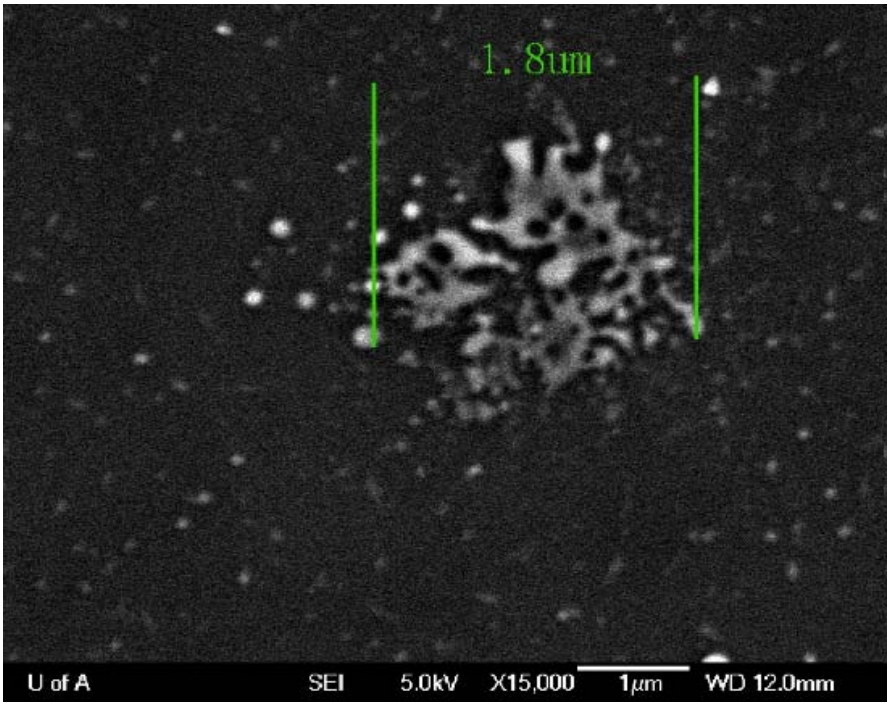
1.8um
U of A
SEI
5.0kV
X15,000
1μm
WD 12.0mm

a

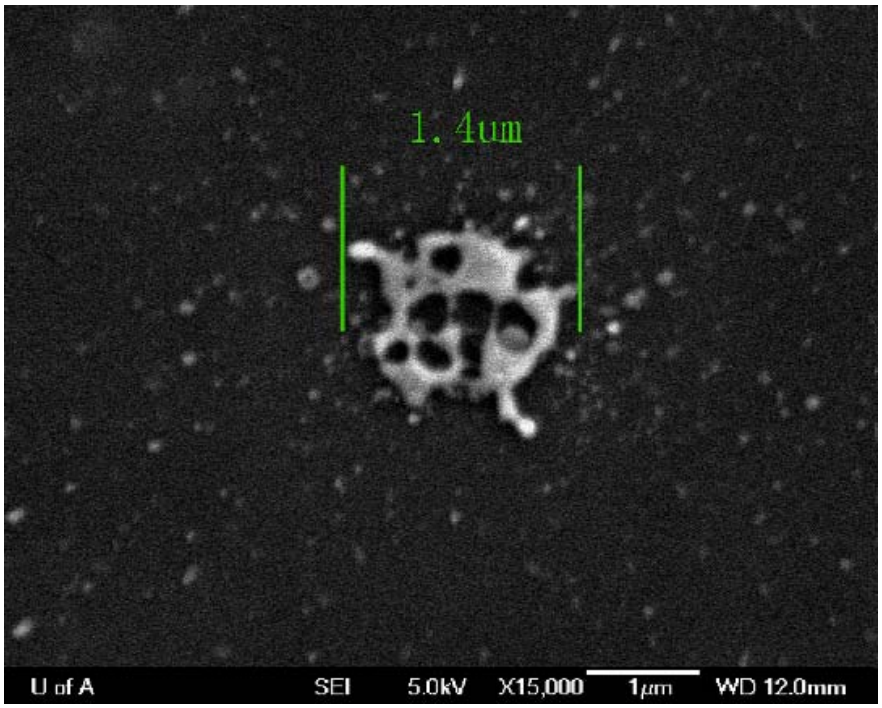
1.4um
U of A
SEI
5.0kV
X15,000
1μm
WD 12.0mm

b

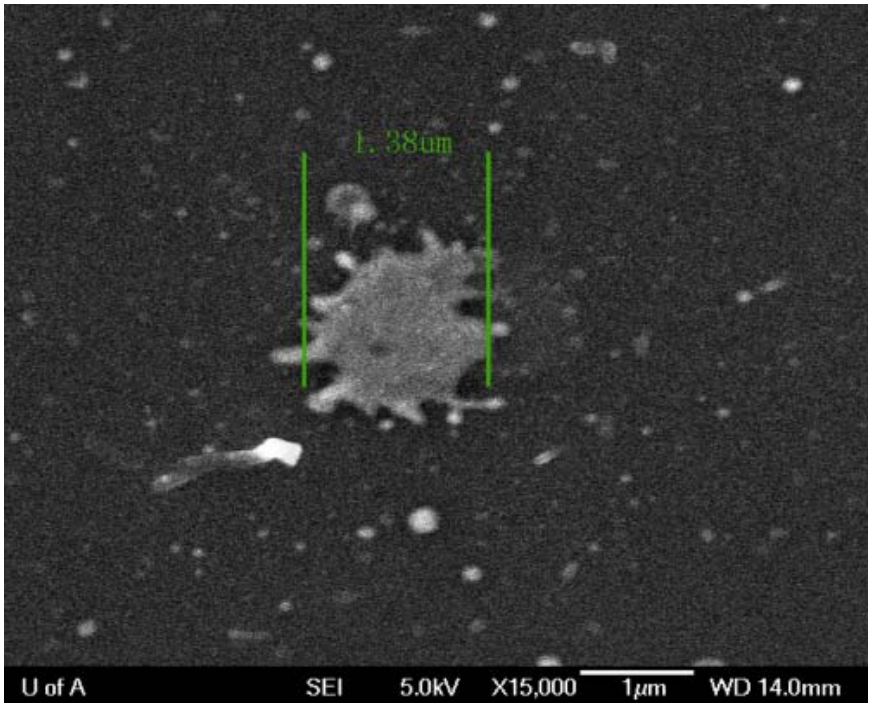
1.38um
U of A
SEI
5.0kV
X15,000
1μm
WD 14.0mm

c

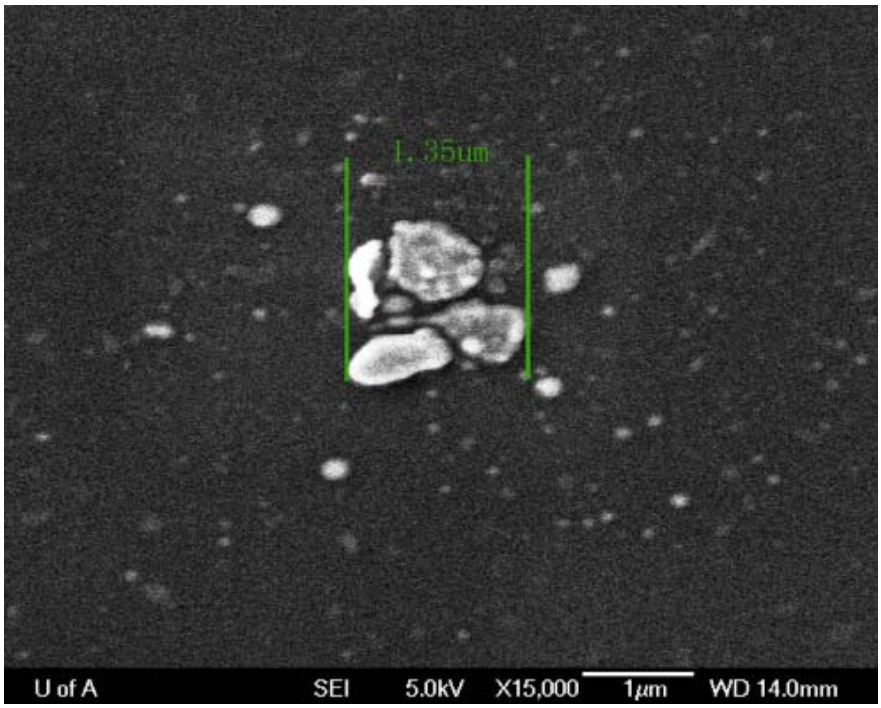
1.35um
U of A
SEI
5.0kV
X15,000
1μm
WD 14.0mm

d

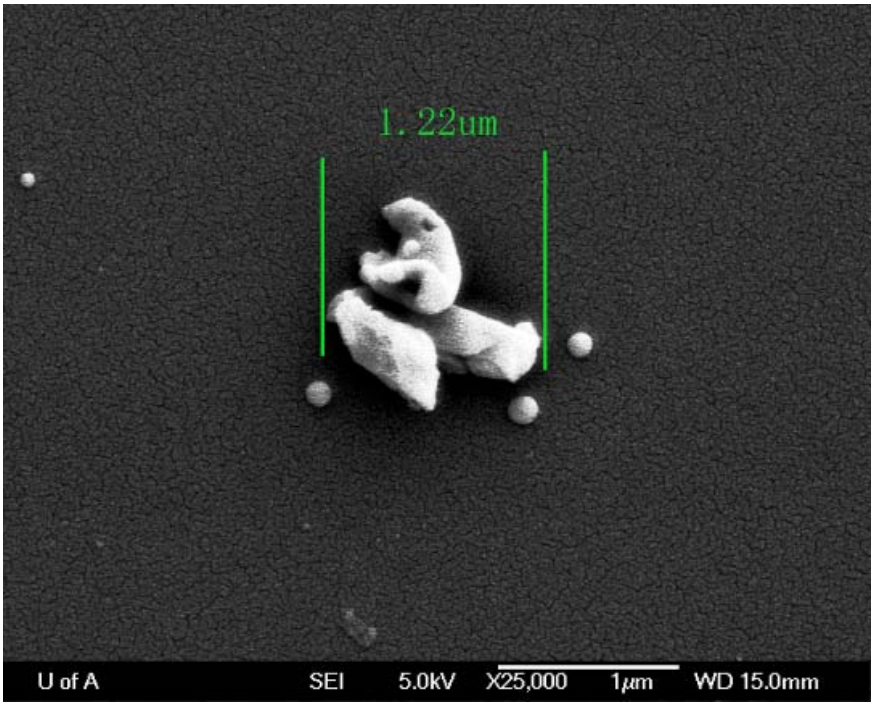

e

Figure 4-17-1 Transferred Cr micro-disks from pre-patterned donor (on focus) (a) F = 1.88 J/cm^2; (b) F = 0.84 J/cm^2; (c) F = 0.57 J/cm^2, (d) F = 0.39 J/cm^2, (e) F = 0.30 J/cm^2

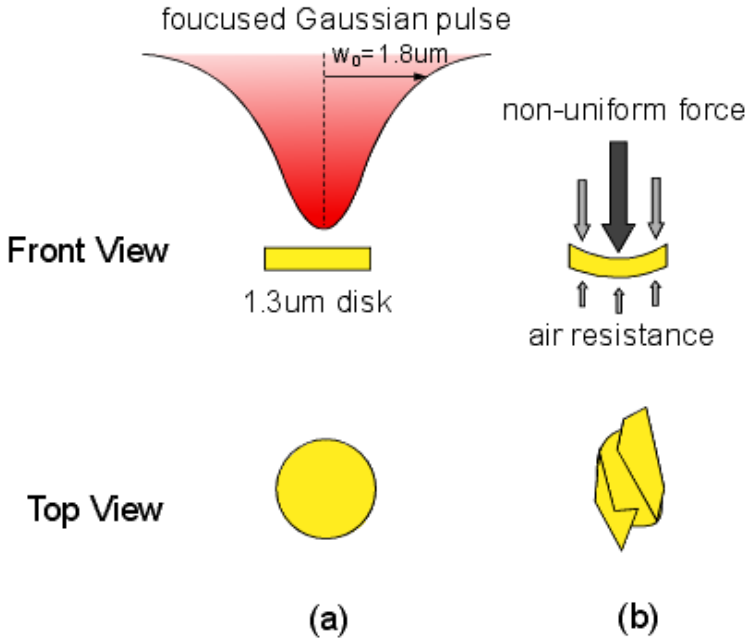

Figure 4-17-2 Illustration of the distorted transfer disk (a, the focused Gaussian laser pulse with w_0=1.8μm illuminates on the 1.3μm disk; b, the non-uniform force caused by the Gaussian pulse propels the disk and causes distortion)

The fraction of successful transfer was defined as number of disks being successfully transferred / number of disks being shot by pulsed laser. This number was examined for different fluence. It was found that the number decreased a lot when the fluence decreased from over 1 J/cm^2 to 0.3 J/cm^2, as shown in Table 4-3. The reduction of fraction of successful transfer may caused by two factors. One is the error occurred during the alignment processes, and the other is the ablation spot getting smaller at low fluence.

In our experiment, the 10×10 μm squares were fabricated as marks because they were big enough to be observed on the screen during the transfer process. The distance from the center of the 10 μm squares to the 1.3 μm disks was 30 μm. Thus, by pointing the laser pulse onto the center of 10 μm square and then move the XYZ stage by 30 μm, we can point the laser pulse onto the 1.3 μm disk. The errors of alignment consist of several facts. The center of the 10×10 μm squares was determined as half of the distance from the two edges. The inaccuracy in determining the exact position of the edge was estimated to be around a few hundred microns. Additional inaccuracies would include the 0.1 μm resolution (as indicated by the manual) of the XYZ micro-positioner and the backlash problem may further increase the inaccuracies as the XYZ micro-positioner was moved back and forth. We estimate our alignment could have an error on the order and this may account for the reduction of faction of successful transfer.

Besides, the ablation spot decreased as the fluence went down. When the fluence was at 0.3 J/cm2, the ablation spot was comparable to the 1.3μm

pre-patterned disk. Because of the errors in alignment it would have a poor chance for a low fluence laser beam spot to overlap with the target disk. On the other hand, the high fluence laser pulse which can produce a large ablation spot would have a better chance of overlapping with the target micro-disk. Even if the laser beam did not completely miss the target and cover only a portion of the micro-disk target this would transfer a portion of the target or cause deformation of the transferred disk. Figure 4-18-1 shows the SEM images of the donor substrate that was transferred by single shot and Figure 4-18-2 is the diagram illustrating the ablation phenomenon. When the fluence was high, those 1.3μm small disks could be transferred as a whole. In image (a) and (b), both disks A and B were transferred as the diameters of ablation laser spots on 10×10μm big marker were larger than 2μm. When the fluence decreased, the ablation spot became smaller, making it hard to transfer the whole micro-disk. In image (c) and (d), the 0.30 J/cm^2 single shots produced holes with diameters around 1.5μm. The 1.3μm small disk can still be transferred as a whole only when the laser was exactly aligned, making sure the laser spot cover the whole small pattern (disk C). Any small deviation will cause only a portion of the disk be transferred, leaving the other portion remaining on the donor substrate (disk D). When the fluence continued to decrease, the ablation spot was smaller than the 1.3μm pre-patterned disk and the disk can not be transferred as a whole (disk E).

Fluence(J/cm^2)	0.36	0.30	0.27	0.24	0.22
Diameter(μm)	2.02	1.49	1.18	0.98	0.53

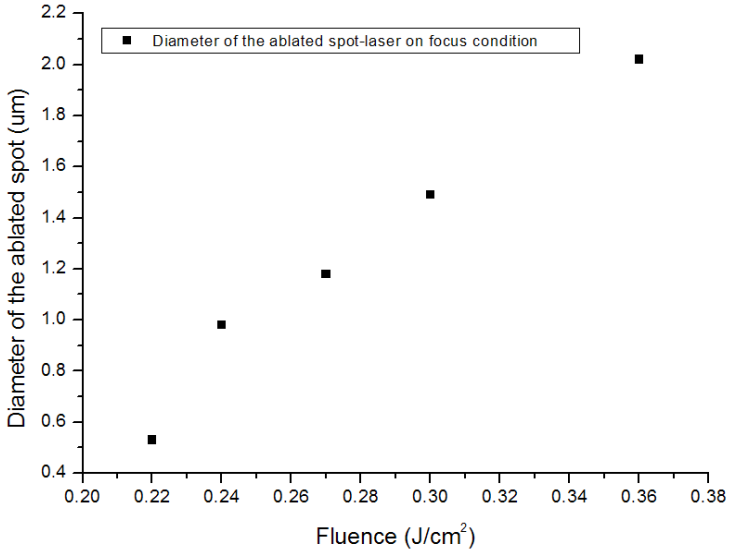

Table 4-2 The relation of diameter of ablated spot on continuous Cr film verses fluence under on focus condition

Fluence(J/cm^2)	1.88	0.84	0.57	0.39	0.30
Fraction of successful transfer	~ 1	~ 1	~ 0.8	~ 0.6	~ 0.1

Table 4-3 The fraction of successful transfer of 1.3μm disk under on focus condition

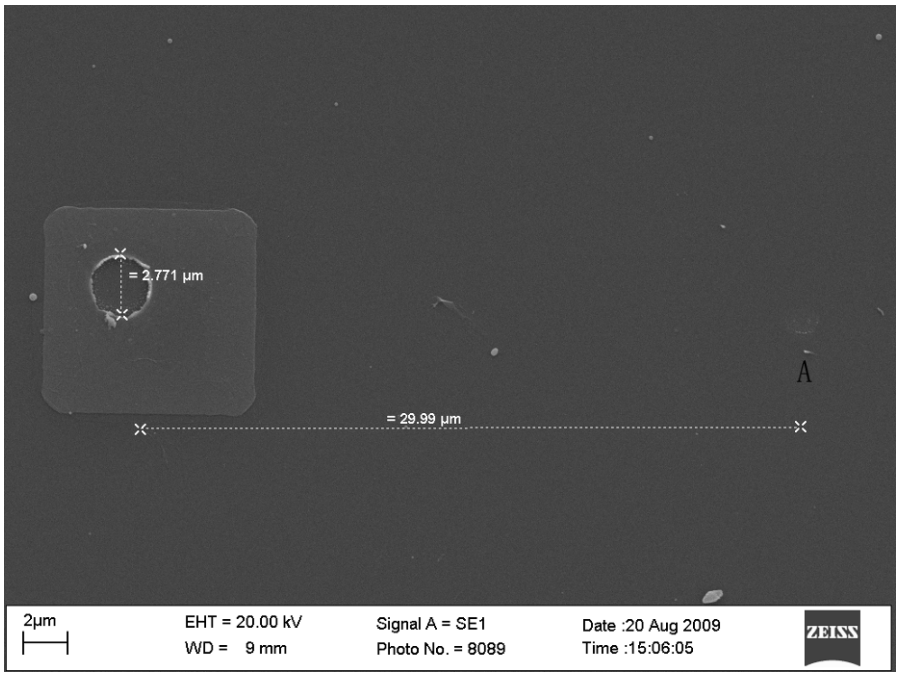

a

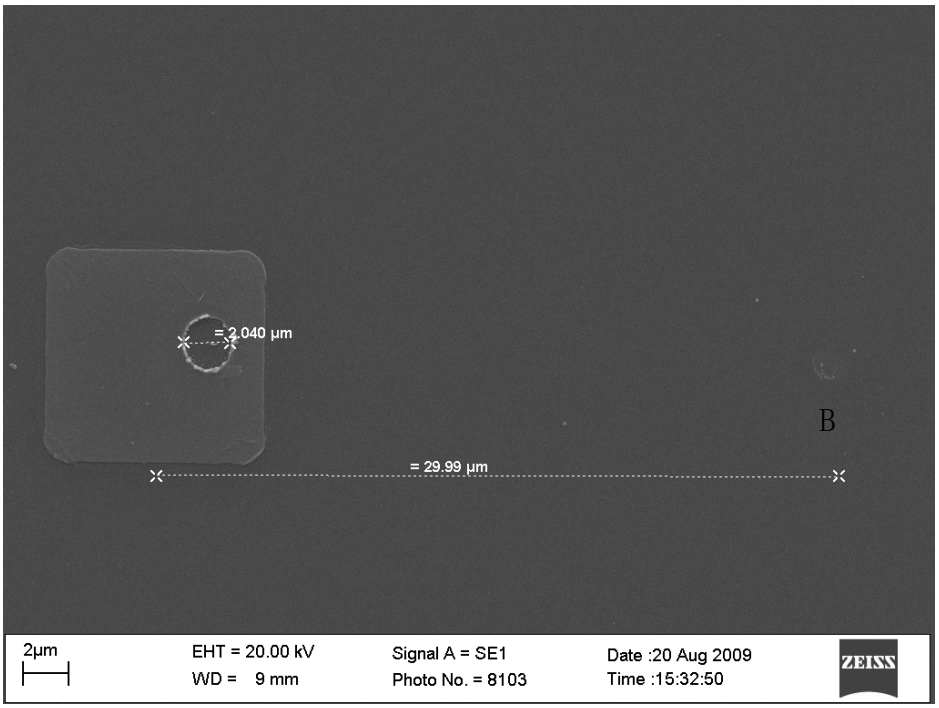
= 2.040 µm
B
= 29.99 µm
2µm
EHT = 20.00 kV
WD = 9 mm
Signal A = SE1
Photo No. = 8103
Date :20 Aug 2009
Time :15:32:50
ZEISS

b

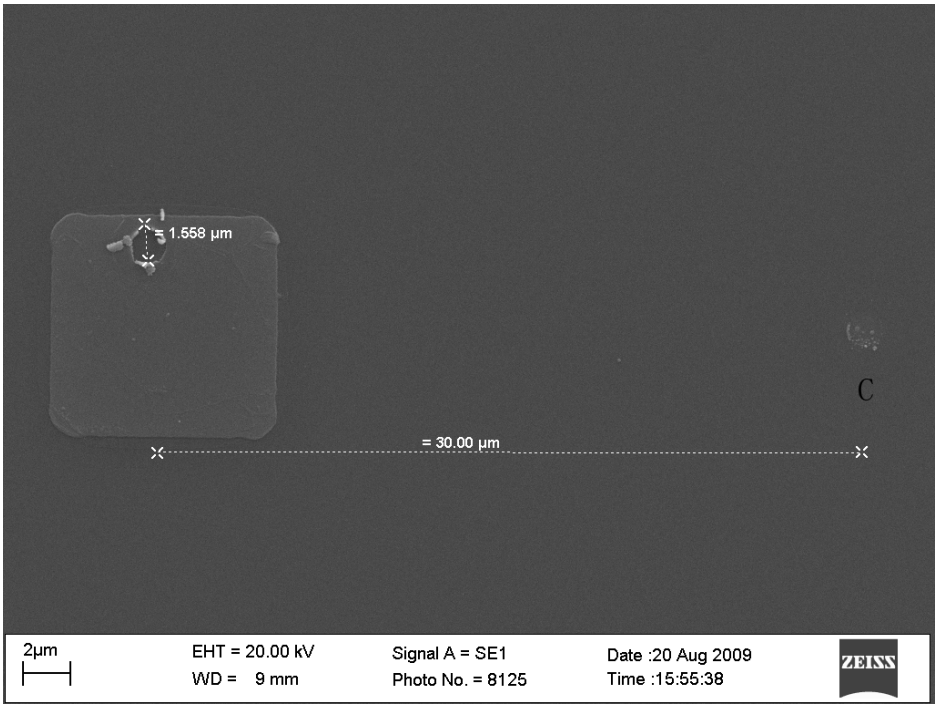
= 1.558 µm
C
= 30.00 µm
2µm
EHT = 20.00 kV
WD = 9 mm
Signal A = SE1
Photo No. = 8125
Date :20 Aug 2009
Time :15:55:38
ZEISS

c

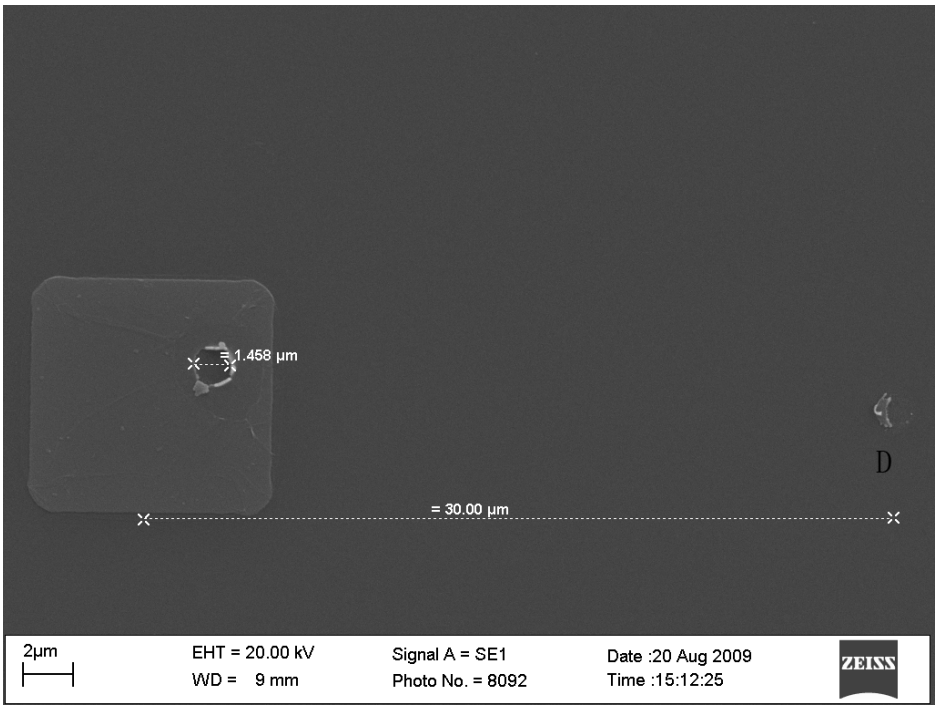

d

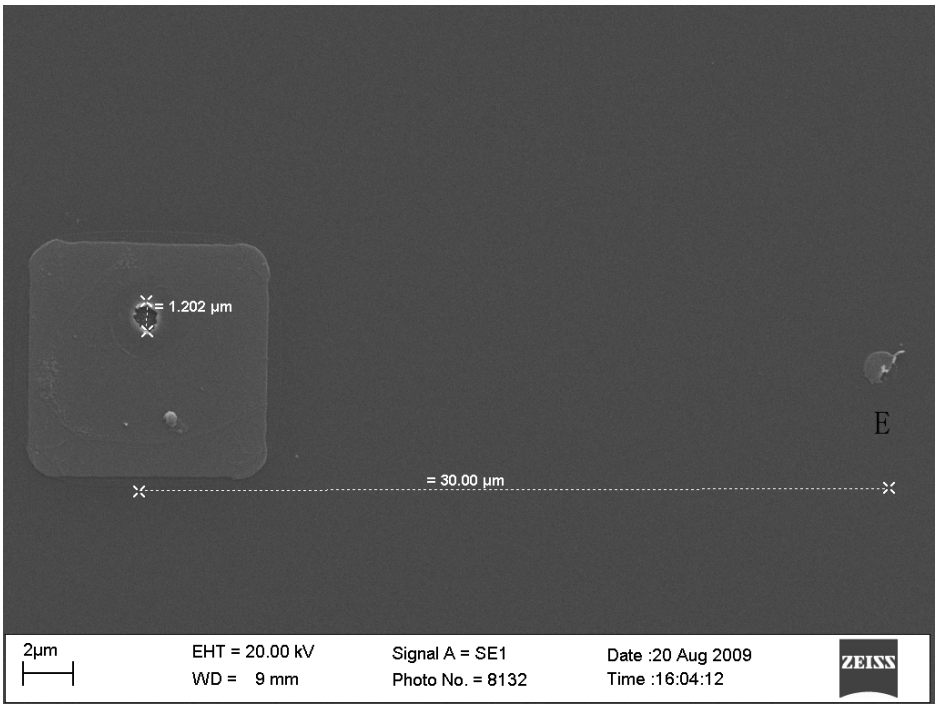

e

Figure 4-18-1 SEM image of donor substrate

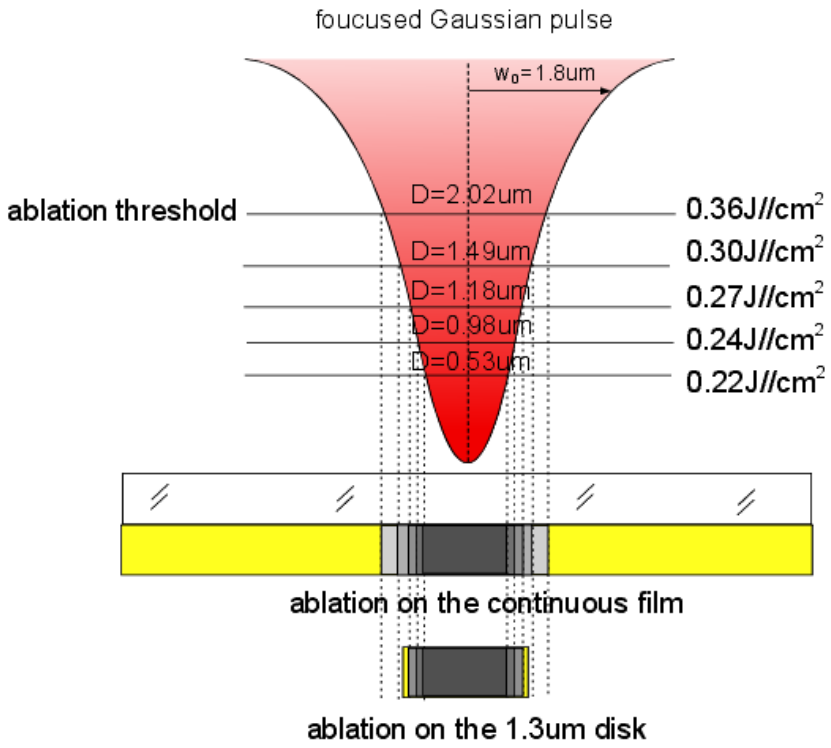

Figure 4-18-2 Illustration of ablation on 1.3μm disk (on focus). (As the fluence below 0.30 J/cm^2, the 1.3μm disk can not be transferred as a whole. Only part of it can be transferred.)

4.2.2 50μm off focus condition

It is clear from the previous discussion that a larger laser spot would be desired. In order to make a larger laser spot, LIFT under off focus condition has been conducted. In this experiment, the donor substrate was placed 50 μm off focus, producing a larger laser spot, so that it would cover the whole micro-disk target and thus transfer it as a whole. Figure 4-19 shows the semi-logarithmic plot by GBLT technique, from which the 50 μm off focused laser beam radius of 10X microscope objective at e^{-2} intensity was measured to be ~ 6.2 μm. Figure 4-20 shows the material being transferred at different fluences. The results at higher

fluences were very similar to those under best focus condition. When the fluence went down to ~ 0.26 J/cm^2, the transferred material retained the same shape as the micro-disk target. The hole in the center of the disk may be caused by a hot spot in the laser beam. When the fluence was at ~ 0.23 J/cm^2, the transferred material seems to be folded likely caused by a non-uniform push force profile. At this fluence the ablation spot has a diameter similar to that of the micro-disk target (see Table 4-4) and if the centers of the ablation spot and the micro-dick target did not overlap then this would result in a non-uniform push force profile and thus could cause the observed folding of the transferred material. Table 4-4 shows the diameter of ablation on continuous film and Figure 4-21 illustrates the 50μm off focused Gaussian pulse illuminating on 1.3μm disk. Table 4-5 shows the fraction of successful transfer numbers. It is found the fraction of successful transfer at low fluence is increased when compared to the best focus case.

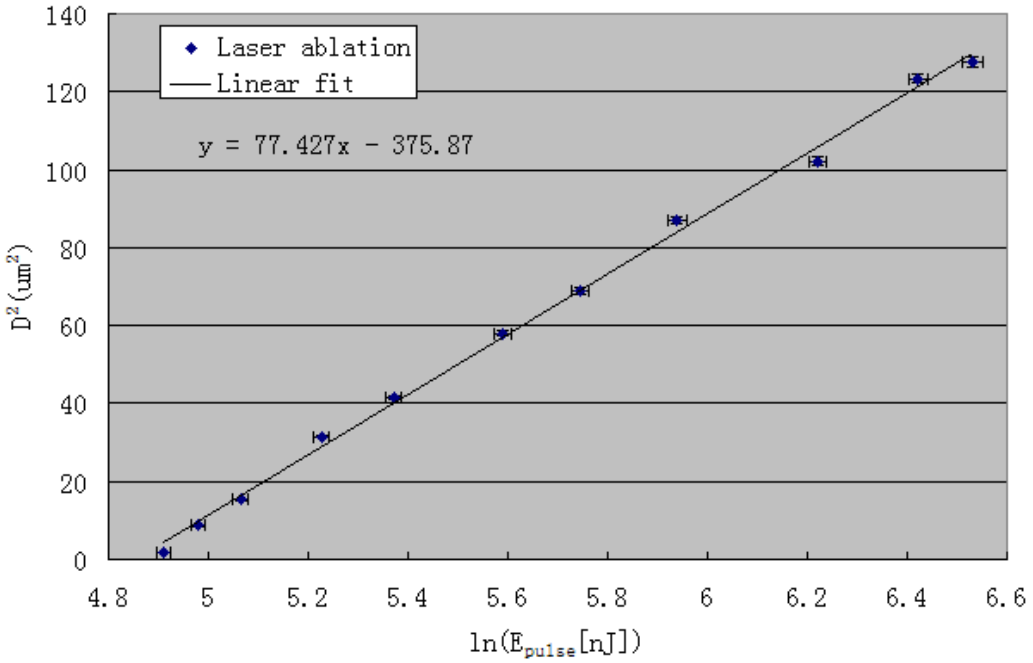

Figure 4-19 Semi-logarithmic plot by GBLT (50μm off focus)

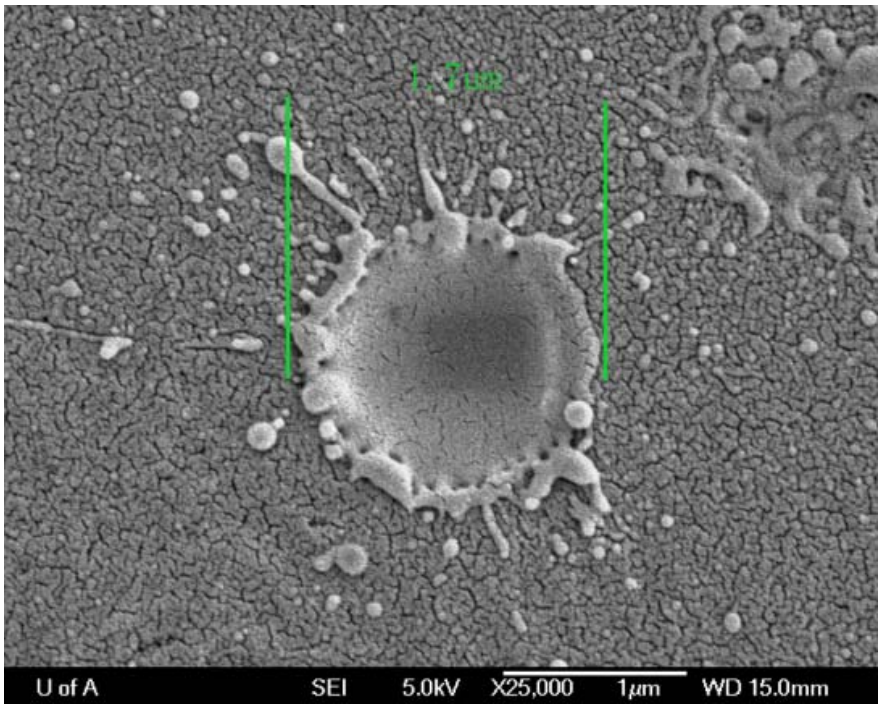

a

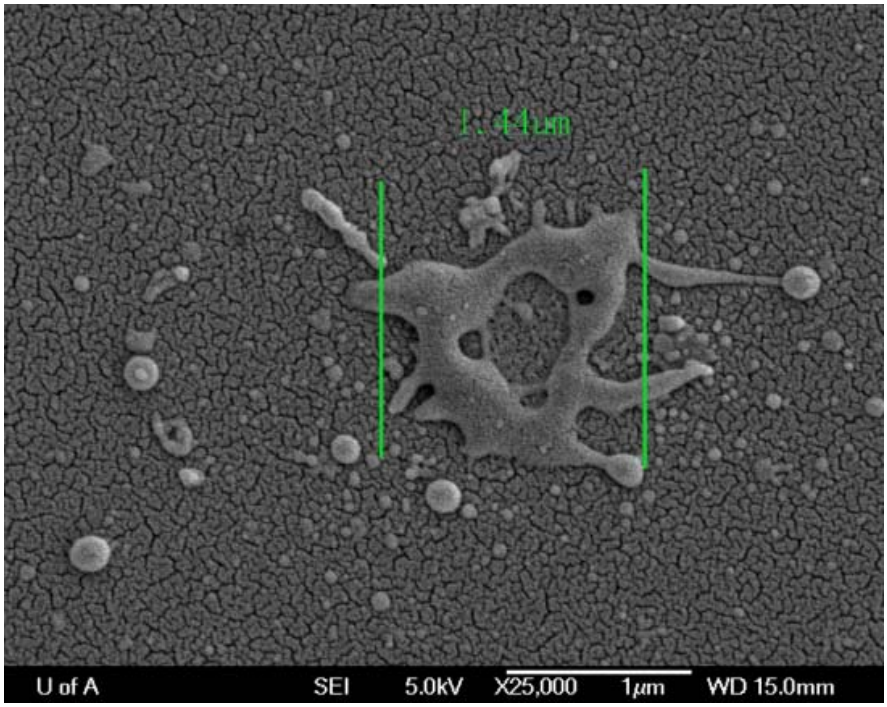
1.44um
U of A
SEI
5.0kV
X25,000
1μm
WD 15.0mm

b

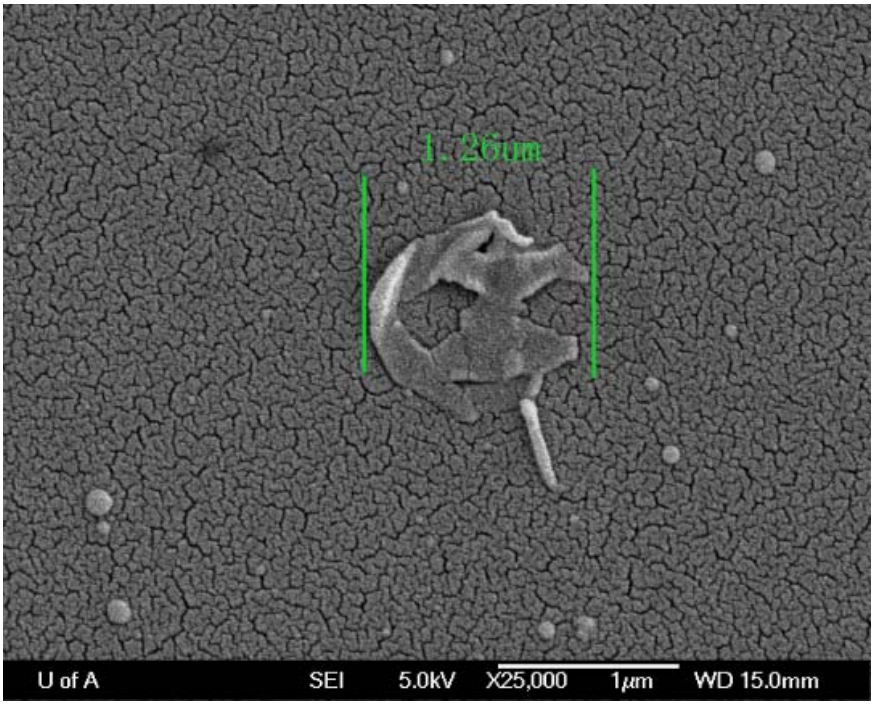
1.26um
U of A
SEI
5.0kV
X25,000
1μm
WD 15.0mm

c

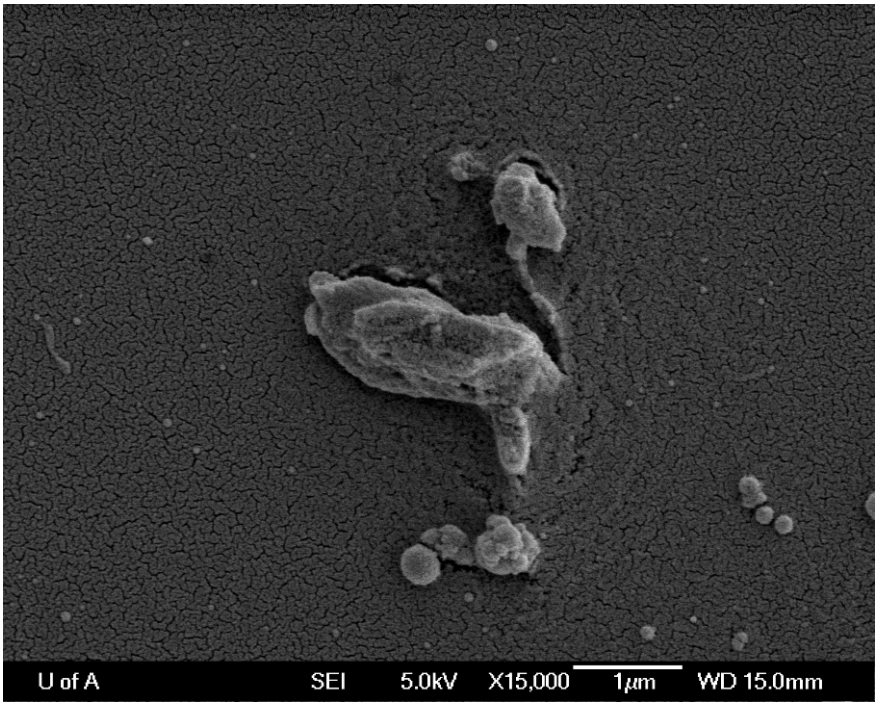

d

Figure 4-20 Transferred Cr micro-disks from pre-patterned donor (50 μm off focus) (a) F = 2.3 J/cm^2; (b) F = 0.8 J/cm^2; (c) F = 0.26 J/cm^2; (d) F=0.23 J/cm^2

Fluence(J/cm^2)	0.35	0.31	0.26	0.24	0.22
Diameter(μm)	6.43	5.61	3.92	2.94	1.34

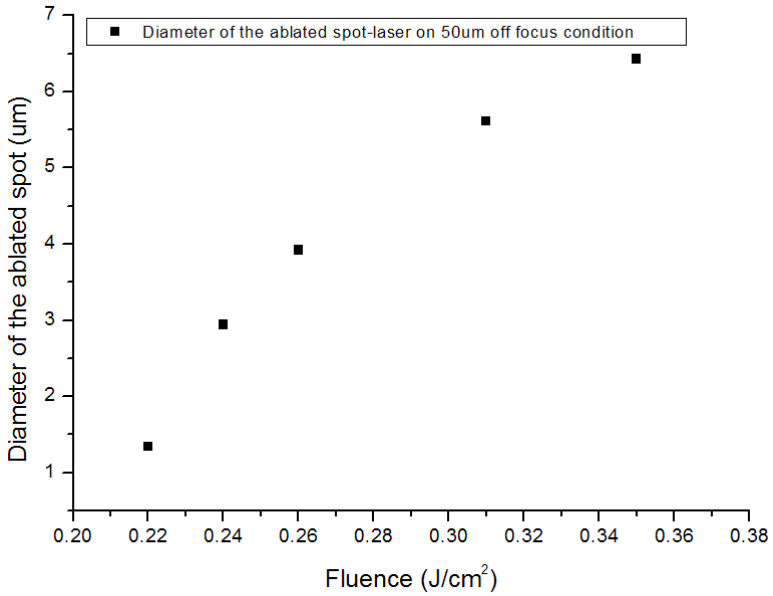

Table 4-4 The relation of diameter of ablated spot on continuous Cr film verses fluence under 50μm off focus condition

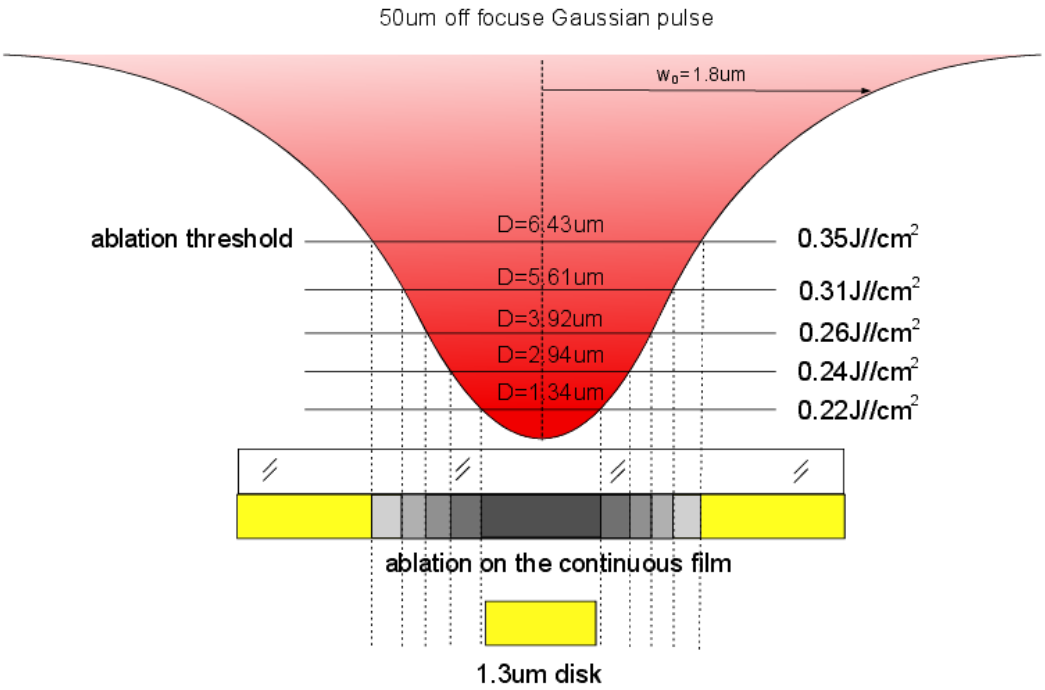

Figure 4-21 Illustration of 50μm off focused Gaussian pulse illuminating on 1.3μm disk

Fluence(J/cm^2)	2.3	0.8	0.26
Fraction of successful transfer	~ 1	~ 1	~ 0.6

Table 4-5 The fraction of successful transfer of 1.3μm disk at different fluence under 50μm off focus condition

4.2.3 Top-hat profile condition

At this point, it is clear a large non-uniform laser spot would help. To further improve the quality of the transferred disk and increase the fraction of successful transfer, a top hat profile laser spot was used. Figure 4-22 shows the schematic diagram for creating a top hat laser profile, where an aperture with radius of 0.5mm was placed in front of the 10X objective at P_1. Since the unfocused laser

beam diameter, D, at e^{-2} intensity was 7.7mm, only a small portion and approximately flat profile at the center was allowed to pass through the aperture. A top-hat laser profile with diameter of 10μm was expected to be formed at the image plate P_2. This laser spot was about ten times of the pre-patterned 1.3μm disk, making it easy to aim and shoot at the micro-disk target. The focal distance *f* was 16mm. D_1 and D_2 were calculated to be 1.616m and 160μm.

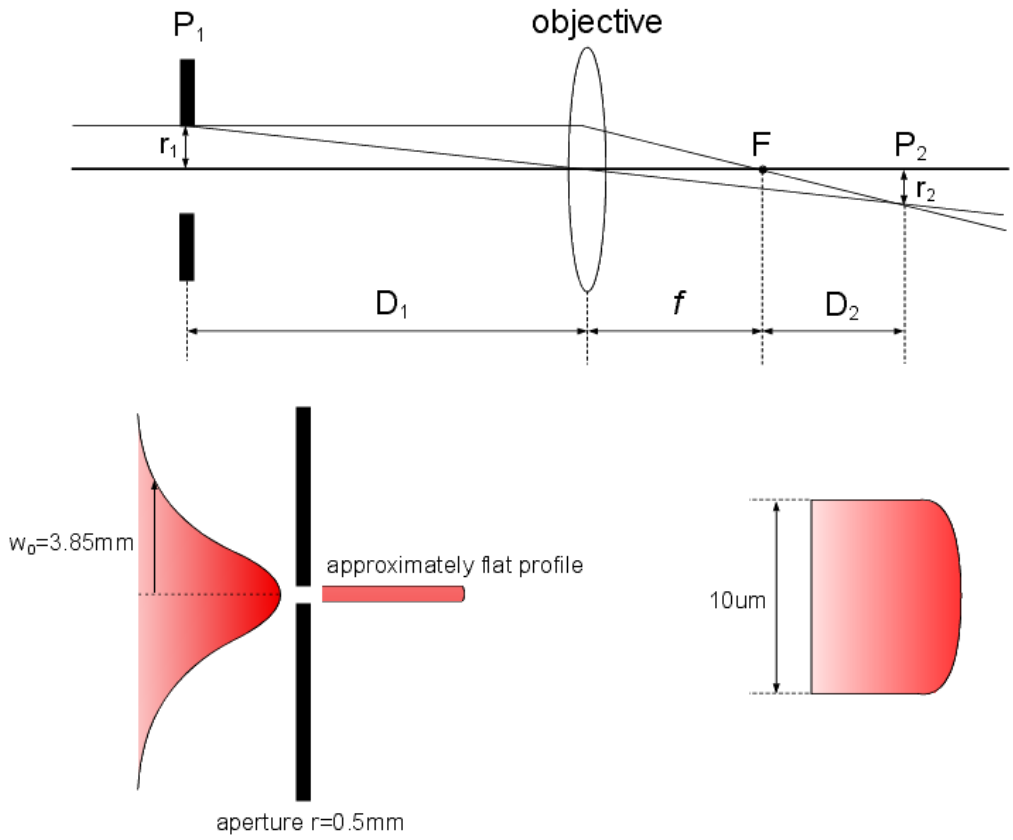

Figure 4-22 Schematic diagrams for creating top hat laser profile

Figure 4-23 shows the results from the LIFT experiments by using this top-hat laser profile. It was found that at 0.26 J/cm^2, the pre-patterned disk was transferred as a whole. This transferred disk was nicely intact, having a very similar profile as

the original micro-disk target and there was almost no debris around the transferred disk. When the fluence reduced to 0.24 J/cm^2, the transferred material became slightly rolled up. This is probably because at this lower fluence close to transfer threshold, fluctuation of laser profile could still cause non-uniform thrust, thus causing the edge of the disk to roll up. When the fluence decreased to 0.23 J/cm^2, this rolling up effect became more pronounced. Figure 4-24 graphically compares a perfect top-hat profile and the approximate top-hat profile used in our experiments. The truncation of a Gaussian beam could cause ripples in a Gaussian beam due to near-field Fresnel-Diffraction [100]. Figure 4-25 shows the ablated hole on 80nm continuous Cr film, where some portion was not ablated probably because of hot spot or non-uniform laser profile. Table 4-6 shows the fraction of successful transfer at lower fluence by top hat laser profile, which was significantly improved due to the bigger laser spot.

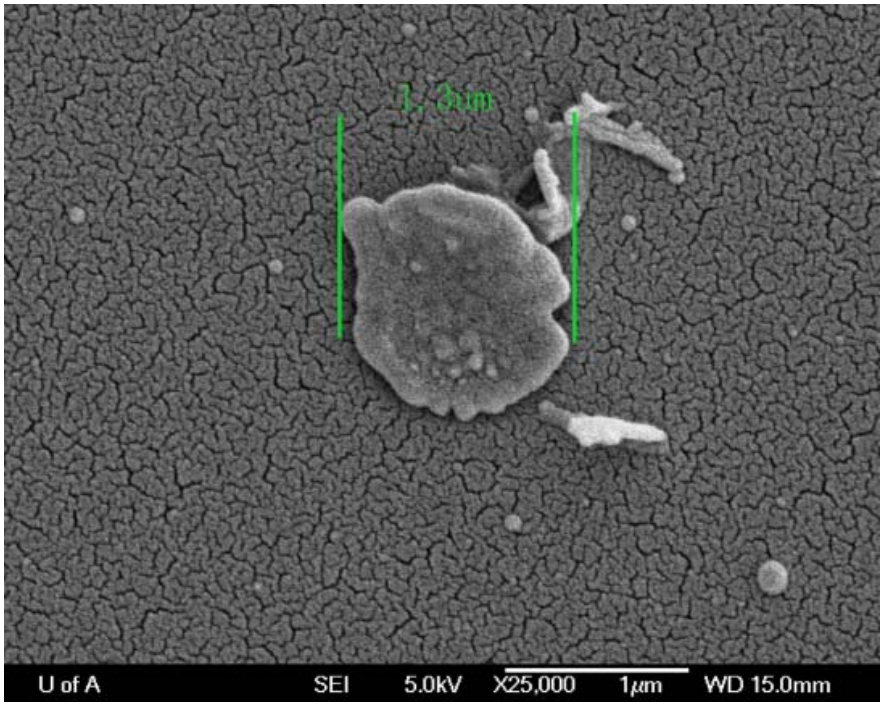
1.3um
U of A
SEI
5.0kV
X25,000
1μm
WD 15.0mm

a

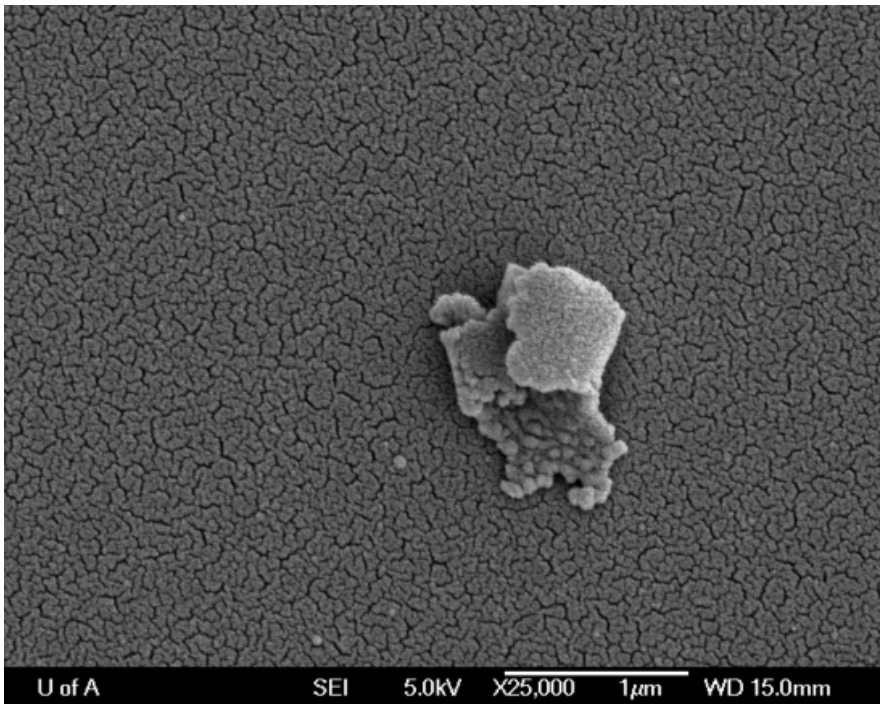
U of A
SEI
5.0kV
X25,000
1μm
WD 15.0mm

b

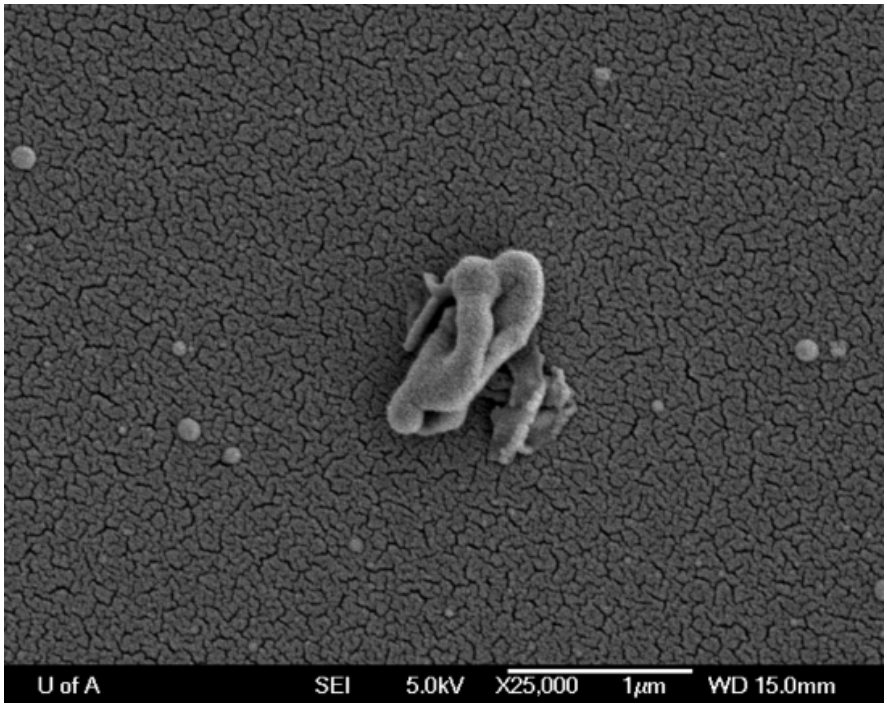

c

Figure 4-23 Transferred Cr micro-disks from pre-patterned donor (Top hat laser profile) (a) F = 0.26 J/cm^2; (b) F = 0.24 J/cm^2; (c) F = 0.23 J/cm^2

Figure 4-24 Illustration of a), a perfect top-hat profile and b), the approximate top-hat from truncating the Gaussian beam used in our experiments.

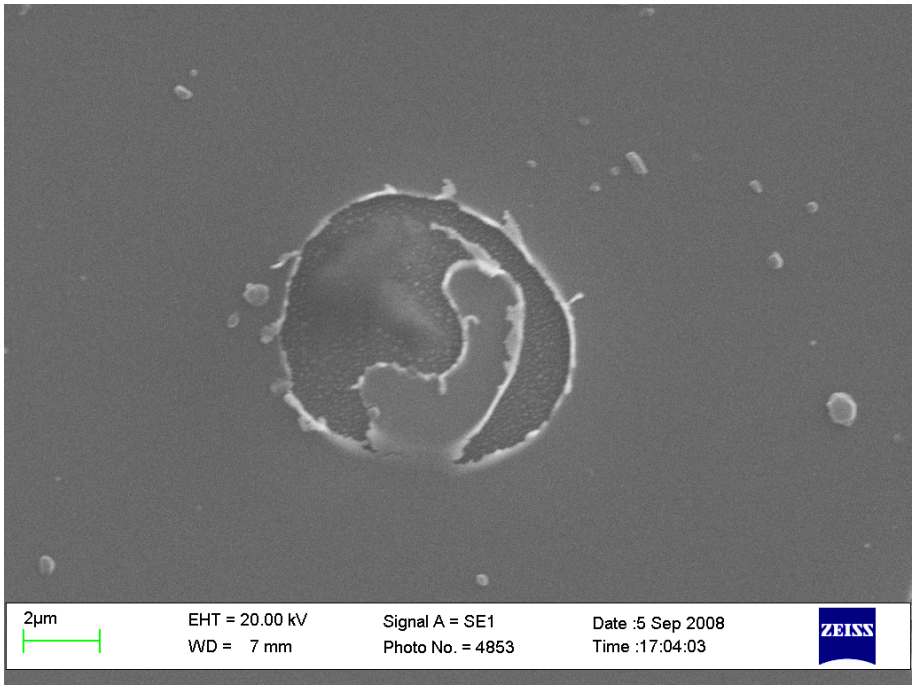

Figure 4-25 SEM image of the ablation on 80nm continuous Cr film cause by approximate top-hat profile (0.26 J/cm^2). Some portion was not ablated probably because of the non-uniform laser profile.

Fluence(J/cm^2)	0.26	0.24	0.23
Fraction of successful transfer	~ 0.9	~ 0.8	~ 0.6

Table 4-6 The fraction of successful transfer of 1.3µm disk at different fluence by top hat laser profile

4.3 LIFT from sub-micron diameter circular Cr disk

To further reduce the resolution limit of LIFT, even smaller disk targets should be used. By using e-beam lithography, alternative rows of 10 µm squares and 0.5 µm diameter Cr sub-micro disks were fabricated on the donor substrates. The laser spot at 50µm off focus was applied to transfer them onto the acceptor substrate. Figure 4-26 shows the SEM images of the transferred results. It was found that at

0.26 J/cm^2, the transferred disk was still intact and kept the same profile as the nano-disk target. At 0.24 J/cm^2, the edge of the transferred disk again became rolled up, but this effect was not as pronounced as that of the 1.3μm diameter Cr disk. One possible reason is that the thrust caused by 0.24J/cm^2 fluence was high enough to push the whole 500nm diameter Cr disk, which was smaller and thus with less mass than the 1.3μm diameter Cr disk. Another possible reason is that the change of aspect ratio of the target means the nano-disk target would behave more like a block of material as it travels through the air gap and more difficult for its edge to get rolled up. The transfer processes of the thin and thick disk are illustrated in Figure 4-27. Compared with the 1.3μm diameter Cr disk transferred under 50μm off focus condition, the fraction of successful transfer was increased too, because it is less likely for the big laser spot to miss the nano-disk target.

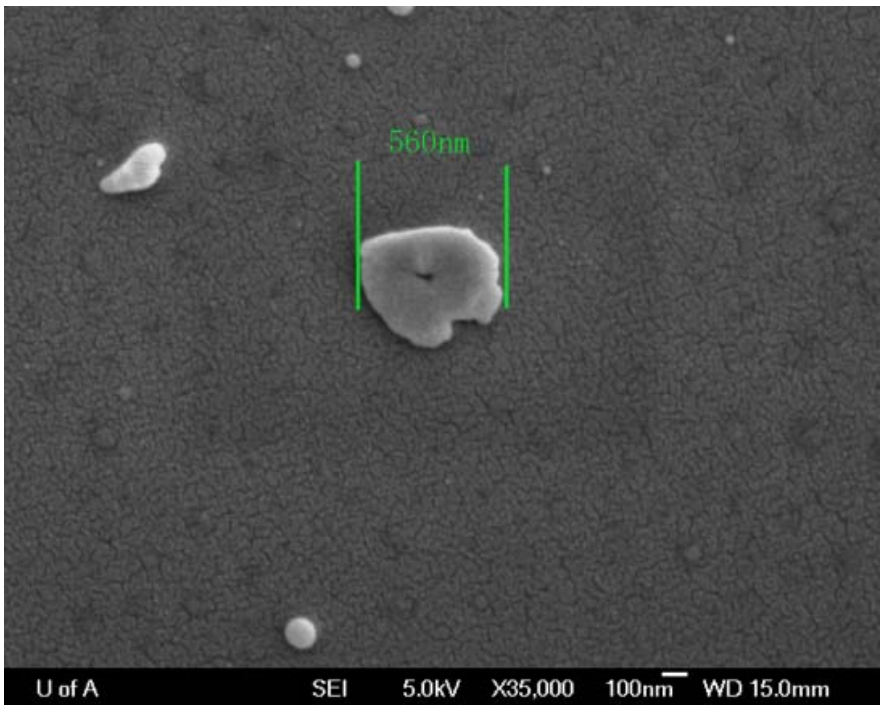

a

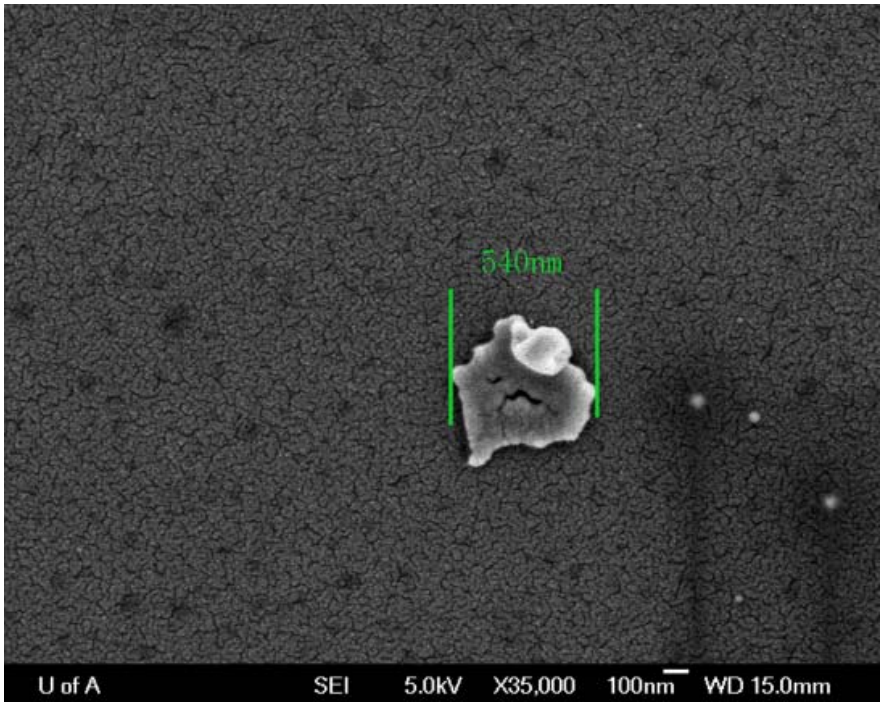

b

Figure 4-26 Transferred Cr sub-micro disks from pre-patterned donor (50µm off focus) (a) F = 0.27 J/cm^2; (b) F = 0.24 J/cm^2

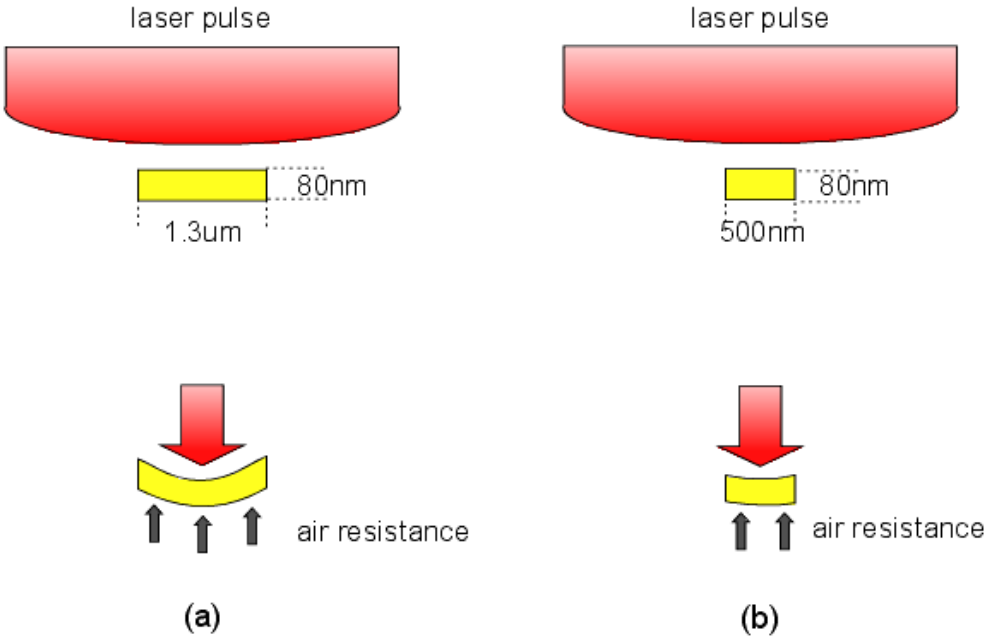

Figure 4-27 Comparison of transfer process of 1.3µm disk and 500nm disk (80nm thick)

Fluence(J/cm^2)	0.27	0.24	0.23
Fraction of successful transfer	~ 0.9	~ 0.7	~ 0.3

Table 4-7 The fraction of successful transfer of 500nm disk at different fluences under 50μm off focus condition

Chapter 5

Conclusion and future work

The laser induced forward transfer (LIFT) using donor substrates consisting of continuous film or pre-patterned disks arrays were investigated. In this research, 800nm, 130fs laser pulses with fluences from 0.2 J/cm^2 to 20 J/cm^2 were used for the LIFT process. By using donor substrates coated with 80nm thick continuous Cr film, Cr material in the form of disk-like shapes can be transferred in air and deposited onto the acceptor substrates by the LIFT technique. Two threshold fluences, ablation threshold and transfer threshold were observed for LIFT and they are 0.21 J/cm^2 and 0.22 J/cm^2 respectively. The transfer threshold is slightly higher because the material on the donor substrate needs to have sufficient thrust to push it through the air gap to deposit onto the acceptor substrate. The heat transfer process controlling the ablation mechanism was simulated by two-temperature model (TTM) and the ablation threshold obtained was consistent with the one from the experiments. It was observed that the morphology of the

transferred materials is very different as the fluences are decreased from around 20 J/cm^2 to below 1 J/cm^2, close to the transfer threshold. The effective diameters of the transferred material also varied from around 10μm to hundreds of nanometers as fluences are reduced. The diameter of the smallest LIFT disks in our studies is around 700nm.

Laser Induced Forward Transfer using donor substrates consisting of pre-patterned Cr micro-disk arrays has been investigated using laser beams with various spatial profiles. The 1.3μm pre-patterned disks can be transferred by the focused laser spot, but the fraction of successful transfer was low and quality of transferred material was not desirable. At low fluences, the Gaussian profile of the laser beam produced an ablation spot (a circle with its boundary is at the ablation threshold) smaller than 1.3μm, the diameter of the pre-patterned disks, as a result, only a portion of the pre-patterned disk would be transferred. In addition the fraction of successful transfer was low probably because the laser beam missed or partly missed the micro-disk target because of laser pointing errors. To transfer the whole pre-patterned disk and to increase the chance of hitting the target, higher fluences are needed, which resulted in debris around the LIFT dots. One practical way to overcome the pointing errors of the laser is to use a larger laser beam spot. When 50μm off focus condition was applied, the fraction of successful transfer was increased and quality of transferred material was improved. The results further improved, when a top-hat laser profile with diameter of 10μm was applied, at fluence slightly above the transfer threshold the transferred disks were mostly

intact, having sizes and shapes very similar to the original pre-transferred disks and there was almost no debris around the transferred disks. The fraction of successful transfer also greatly increased. To push further the resolution limit of LIFT, donor substrates consist of pre-patterned 0.5 μm diameter Cr disk arrays were used. In this case it was observed that the 50μm out of focused condition would be sufficient in allowing a good transfer. At low fluence slightly larger than the transfer threshold, the disks survived the LIFT process as a whole and produce a nicely intact pattern on the donor substrate. The current thesis research represents only the very first step of attempting to extend the LIFT technique to the nano-scale regime. On-going studies using donor substrates consisting of pre-patterned disks with diameter of 100nm and under are currently being carried out by our research group. In order to apply this nano-LIFT technique developed in this thesis research for repairing, modifying and prototyping nano-devices, clearly much more research remains to be done.

References

[1] C.B. Arnold and A. Piqué, "Laser direct-write of complex materials," *MRS Bulletin*, 32, (2007) 32.

[2] S. Klein, T. Stratoudaki, Y. Marakis, V. Zafiropulos, K. Dickmann, "Comparative study of different wavelengths from IR to UV applied to clean sandstone," *Appl Surf Sci.*, 157, (2000) 1.

[3] J. Feinleib, J. deNeufville, S.C. Moss, and S.R. Ovshinsky, "Properties of (Se,S)-based chalcogenide glass films, and an application to a holographic supermicrofiche," *Appl. Phys. Lett*., 18, (1971) 254.

[4] R.M Osgood and T.F. Deutsch, "Laser-induced chemistry for microelectronics," *Sciencs*, 227, (1985) 709.

[5] I.P. Herman, "Laser-assisted deposition of thin films from gas-phase and surface-absorbed molecules," *Chem. Rev.*, 89, (1989) 1323.

[6] T. Hitosugi and T. Mizuno, "Femtosecond-laser-assisted chemical vapor deposition of Cr metal," *Jpn. J. Appl, Phys.*, 44, (2005) L596.

[7] A. Piqué, R.C.Y. Auyeung, H. Kim, K.M. Metkus and S.A. Mathews, "Digital microfabrication by laser decal transfer," *JLMN-Journal of Laser Micro/Nanoengineering*, 3, (2008) 163.

[8] Bohandy et al, "Metal deposition from a supported metal film using an excimer laser," *J. Appl. Phys.*, 60, (1986) 1538.

[9] J. Bohandy, B.F. Kim, F.J. Adrian and A.N. Jette. "Metal deposition at 532 nm using a laser transfer technique," *J. Appl. Phys.*, 63, (1988) 1158.

[10] R.M. Osgood, Jr., "Laser microchemistry and its application to electron-device fabrication," *Annu. Rev. Phys. Chem.*, 31, (1983) 77.

[11] D.J. Ehrlich and J.Y. Tsao, "VLSI Electronics: Microstructure Science (Academic Press, New York)," vol. 7, (1983) 129.

[12] F.A. Houle, C.R. Jones, T. Baum, C. Pico, and C.A. Kovac, "Laser chemical vapor deposition of copper," *Appl. Phys. Lett.*, 46, (1985) 204.

[13] R.F. Karlicek, V.M. Donnelly, and G.J. Collins, "Laser-induced metal deposition," *J. Appl. Phys.*, 53, (1982) 1084.

[14] M.E. Gross, G.J. Fisanick, P.K. Gallagher, K.J. Schnoes, and M.D. Fennell, "Laser-initiated deposition reactions-Microchemistry in organogold polymer films," *Appl. Phys. Lett.*, 47, (1985) 923.

[15] H.H. Gilgen, T. Cacouris, P.S. Shaw, R.R. Krchnavek, and R.M. Osgood, "Direct writing of metal conductors with near-UV light," *Appl. Phys. B*, 42, (1987) 55.

[16] D.E. Alexander, G.S. Was and F.J. Mayer, "Laser-driven micro-explosive bonding of aluminum films to copper and silicon," *J. Mater, Sci.*, 23, (1988) 2181.

[17] R.J. Baseman, N.M. Froberg, J.C. Andreshak and Z. Schlesinger, "Minimum fluence for laser blow-off of thin gold films at 248 and 532 nm," *App. Phys. Lett.*, 56, (1990) 1412.

[18] S. Latsch, H. Hiraoka, W. Nieveen, J. Bargon, "Interface study on laser-induced material transfer from polymer and quartz surfaces," *App. Surf. Sci.*, 81, (1994) 183.

[19] C. Germain, L. Charron, L. Lilge, Y.Y. Tsui, "Electrodes for microfluidic devices produced by laser induced forward transfer," *Appl. Surf. Sci.*, 253, (2007) 8328.

[20] Z. Toth, T. Szorenyi, A.L. Toth, "Ar laser induced forward transfer (LIFT): a novel method for micrometer size surface patterning," *App. Surf. Sci.*, 69, (1993) 317.

[21] Z. Kantor, Z. Toth, T. Szorenyi, "Metal pattern deposition by laser-induced forward transfer," *App. Surf. Sci.*, 86, (1995) 196.

[22] I. Zergioti, S. Mailis, N.A. Vainos, P. Papakonstantinou, C. Kalpouzos, C.P. Grigoropoulos, and C. Fotakis, "Microdeposition of metal and oxide structures using ultrashort laser pulses," *Appl. Phys. A*, 66, (1998) 579.

[23] F.J. Adrian, J. Bohandy, B.F. Kim, A.N. Jette and P. Thompson, "A study of the mechanism of metal deposition by laser induced forward transfer process," *J. Vac. Sci. Technol. B*, 5, (1987) 1490.

[24] J.A. Greer and T.E. Parker, "Laser-induced forward transfer of metal oxides to trim the frequency of surface acoustic wave resonator devices," *Proc. SPIE*, 998, (1988) 113.

[25] E. Fogarassy, C. Fuchs, F. Kerherve, G. Hauchecorne, and J. Perriere, "Laser-induced forward transfer of high-T_c YBaCuO and BiSrCaCuO superconducting thin films," *J. Appl. Phys.*, 66, (1989) 457.

[26] V. Dinca, E. Kasotakis, J. Catherine, A. Mourka, A. Mitraki, A. Popescu, M. Kinescu, M. Farsari, C. Fotakis, "Development of peptide-based patterns by laser transfer," *App. Surf. Sci.*, 254, (2007) 1160.

[27] J.A. Barron, H.D. Young, D.D. Dlott, M.M. Darfler, D.B. Krizman, B.R. Ringeisen, "Printing of protein microarrays via a capillary-free fluid jetting mechanism," *Proteomics*, 5, (2005) 4138.

[28] J.A. Barron, R. Rosen, J. Jones-Meehan, B.J. Spargo, S. Belkin, B.R. Ringeisen, "Biological laser printing of genetically modified *Escherichia coli* for biosensor applications," *Biosens. Bioelectron.*, 20, (2004) 246.

[29] A. Doraiswamy, R.J. Narayan, T. Lippert, L. Urech, A. Wokaun, M. Nagel, B. Hopp, M. Dinescu, R. Modi, R.C.Y. Auyeung, D.B. Chrisey, "Excimer laser forward transfer of mammalian cells using a novel triazene absorbing layer," *App. Suf. Sci.*, 252, (2006) 4743.

[30] A. Karaiskou, I. Zergioti, C. Fotakis, M. Kapsetaki, D. Kafetzopoulos, "Microfabrication of biomaterials by the sub-ps laser-induced forward transfer process," *App. Surf. Sci.*, 208-209, (2003) 245.

[31] I. Zergioti, S. Mailis, N.A. Vainos, C. Fotakis, S. Chen, C.P. Grigoropoulos, "Microdeposition of metals by femtosecond excimer laser," *App. Surf. Sci.*, 127-129, (1998) 601.

[32] I. Zergioti, S. Mailis, N.A. Vainos, A. Ikiades, C.P. Grigoropoulos, C. Fotakis, "Microprinting and microetching of diffractive structures using ultrashort laser pulses," *App. Surf. Sci.*, 138-139, (1999) 82.

[33] I. Zergioti, D.G. Papazoglou, A. Karaiskou, C. Fotakis, E. Gamaly, A. Rode, "A comparative schlieren imaging study between ns and sub-ps laser forward transfer of Cr," *App. Surf. Sci.*, 208-209, (2003) 177.

[34] D. von der Linde, K. Sokolowski, J. Bialkowski, "Laser-solid interaction in the femtosecond time regime," *App. Surf. Sci.*, 109-110, (1997) 1.

[35] E.G. Gamaly, A.V. Rode, B. Luther-Davies, "Ultrafast ablation with high-pulse-rate laser. Part I: Theoretical consideration," *J. Appl. Phys.*, 85, (1999) 4213.

[36] D.E. Hare, J. Franken, D.D. Dlott, "Coherent Raman measurements of polymer thin-film pressure and temperature during picosecond laser ablation," *J. Appl. Phys.*, 77, (1995) 5950.

[37] W.A. Tolbert, I.-Y.S. Lee, M.M. Doxtader, E.W. Ellis, and D.D. Dlott, "High-speed color imaging by laser ablation transfer with a dynamic release layer: fundamental mechanisms," *J. Imaging. Sci. Tech.*, 37, (1993) 411.

[38] J.M. Fitz-Gerald, A. Piqué, D.B. Chrisey, P.D. Rack, M. Zeleznik, R.C.Y. Auyeung, and S. Lakeou, "Laser direct writing of phosphor screens for high-definition displays," *Appl. Phys. Lett.*, 76, (2000) 1386.

[39] J.M. Fernández-Pradas, M. Colina, P. Serra, J. Domínguez, J.L. Morenza, "Laser-induced forward transfer of biomolecules," *Thin Sol. Films*, 453-454, (2004) 27.

[40] P. Serra, J.M. Fernández-Pradas, F.X. Berthet, M. Colina, J. Elvira, J.L. Morenza, "Laser direct writing of biomolecule microarrays," *Appl. Phys. A,* 79, (2004) 949.

[41] M. Duocastella, J.M. Fernández-Pradas, P. Serra, J.L. Morenza, "Laser-induced forward transfer of liquids for miniaturized biosensors preparation," *JLMN-Journal of Laser Micro/nanoengineering*, 3, (2008) 1.

[42] D.B. Chrisey, A. Piqué, J. Fitz-Gerald, R.C.Y. Auyeung, R.A. McGill, H.D. Wu, M. Duignan, "New approach to laser direct writing active and passive mesoscopic circuit elements," *App. Surf. Sci.*, 154-155, (2000) 593.

[43] D.B. Chrisey, A. Piqué, R. Modi, H.D. Wu, R.C.Y. Auyeung, H.D. Young, "Direct writing of conformal mesoscopic electronic devices by MAPLE DW," *App. Surf. Sci.*, 168, (2000) 345.

[44] A. Piqué, D.B. Chrisey, J.M. Fitz-Gerald, R.A. McGill, R.C.Y. Auyeung, H.D. Wu, S. Lakeou, Viet Nguyen, R. Chung, M. Duignan, "Direct writing of electronic and sensor materials using a laser transfer technique," *J. Mater. Res.*, 15, (2000) 1872.

[45] A. Piqué, C.B. Arnold, R.C. Wartena, B. Pratap, B. Shashishekar, K.E. Swider-Lyons, D.W. Weir, and R.A. Kant, "Laser direct-write of miniature sensor and microbattery systems," *RIKEN Review*, 50, (2003) 57.

[46] A. Piqué, R.C.Y. Auyeung, K.M. Metkus, H. Kim, S. Mathews, T. Bailey, X. Chen and L.J. Young, "Laser decal transfer of electronic materials with thin film characteristics," *SPIE Proc.*, 6879, (2008) 687911-1.

[47] A. Piqué, R.C.Y. Auyeung, H. Kim, K.M. Metkus, S.A. Mathews, "Digital microfabrication by laser decal transfer," *JLMN-Journal of Laser Micro/Nanoengineering*, 3, (2008) 163.

[48] C.B. Arnold, T.E. Sutto, H. Kim, A. Piqué, "Direct-write laser processing creates tiny electrochemical systems," *Laser Focus World*, 5, (2004) S9.

[49] R.C.Y. Auyeung, M.W. Nurnberger, D.J. Wendland, A. Piqué, C.B. Arnold, A.R. Abbott, L.C. Schuette, "Laser fabrication of GPS conformal antennas," *SPIE Proc.*, 5339, (2004) 292.

[50] H. Kim, A. Piqué, G.P. Kushto, R.C.Y. Auyeung, S.H. Lee, C. B. Arnold, Z.H. Kafafi, "Dye-sensitized solar cells using laser processing techniques," *SPIE Proc.*, 5339, (2004) 348.

[51] A. Piqué, B. Pratap, S.A. Mathews, B.J. Karns, R.C.Y. Auyeung, M. Kasser, M. Ollinger, H. Kim, S. Lakeou, C.B. Arnold, "Laser direct-write of embedded electronic components and circuits," *SPIE Proc.*, 5713, (2005) 223.

[52] A Piqué, S.A. Mathews. B. Pratap, R.C.Y. Auyeung, B.J. Karns, S. Lakeou, "Embedding electronic circuits by laser direct-write," *J. Microelectron. Eng.*, 83, (2006) 2527.

[53] I.-Y.S. Lee, W.A. Tolbert, D.D. Dlott, M.M. Doxtader, D.M. Foley, D.R. Arnold, E.W. Ellis, "Dynamics of laser ablation transfer imaging investigated by ultrafast microscopy," *J. Imag. Sci. Tech.*, 36, (1992) 180.

[54] D. Young, R.C.Y. Auyeung, A, Piqué, D.B. Chrisey, D. Dlott, "Time-resolved optical microscopy of a laser-based forward transfer process," *Appl. Phys. Lett.*, 78, (2001).

[55] Y. Nakata, T. Okada, "Time-resolved microscopic imaging of the laser-induced forward transfer process," *Appl. Phys. A*, 69, (1999) 275.

[56] David P. Banks, Christos Grivas, John D. Mills, and Roberta W. Eason, "Nanodroplets deposited in microarrays by femotosecond Ti:sapphire laser-induced forward transfer," *Appl. Phys. Lett.*, 89, (2006) 193107.

[57] N. Bloembergen, "Laser-induced electric breakdown in solids," *IEEE J. Quantum Electron.*, QE-10, (1974) 375.

[58] P. B. Corkum, F. Brunel, and N. K. Sherman, "Thermal response of metals to ultrashort –pulse laser excitation," *Phys. Rev. Lett.*, 61, (1988) 2886.

[59] David P. Banks, Christos Grivas, Ioanna Zergioti, and Roberta W. Eason, "Ballistic laser-assisted solid transfer (BLAST) from a thin film precursor," *Optics Express*, Vol. 16, No. 5, (2008) 3249.

[60] X. Liu, D. Du, and G. Mourou, "Laser ablation and micromachining with ultrashort laser pulses," *IEEE Journal of Quantum Electronics*, 35, (1997) 1706.

[61] B.N. Chichkov, C. Momma, S. Nolte, F. von Alvensleben, A. Tunnermann, "Femtosecond, picosecond and nanosecond laser ablation of solids," *Appl. Phys. A*, 63, (1996) 109.

[62] N. A. Ashcroft and N. D. Mermin, "Solid State Physics," 1st ed. New York: Holt Rinehart and Winston, (1976).

[63] S. I. Anisimov and B. Rethfeld, "On the theory of ultrashort laser pulse interaction with a metal," *Proc. SPIE*, 3093, (1997) 192.

[64] D. Strickland and G. Mourou, "Compression of amplified chirped optical pulses," *Opt. Commun.*, 55, (1985) 447.

[65] P. Maine, D. Strickland, P. Bado, M. Pessot, and G. Mourou, "Generation of ultrahigh peak power pulses by chirped pulse amplification," *IEEE J. Quantum Electron.*, 24, (1988) 398.

[66] M. Perry, "Multilayer dielectric gratings: Increasing the power of light," *Science & Technology Review*, September (1995) 24.

[67] P. F. Moulton, "Spectroscopic and laser characteristic of Ti:Al_2O_3," *J. Opt. Soc. Am. B*, 3, (1986) 125.

[68] C. Kittel, "Introduction to Solid State Physics," 7th ed. New York: Wiley, (1996).

[69] J. Kim, S. Na, "Metal thin film ablation with femtosecond pulsed laser," *Opt. Laser Technol.*, 39, (2007) 1443.

[70] Z. Han, C. Zhou, E. Dai, J. Xie, "Ultrafast double pulses ablation of Cr film on glass," *Opt. Commun.*, 281, (2008) 4723.

[71] D. R. Lide, “CRC handbook of chemistry and physics [electronic resource],” 84th ed. Binghamton: Knovel, (2004).

[72] J.M. Liu, “Simple technique for measurements of pulsed Gaussian-beam spot sizes,” *Optics Letters*, 7, (1982) 196.

[73] Peter Sigmund, “Theory of Sputtering,” *Physical Review*, 184, (1969) 383.

[74] Leon Maissel, “The Deposition of Thin Films by Cathode Sputtering,” *Physics of Thin Films*, 3.

[75] W.D. Westwood, “Reactive Sputtering,” *Physics of Thin Films*, 14, (1989) 1-79.

[76] R.R. Parsons, “Sputter Deposition Processes,” *Thin Film Processes II*, Chapter II-4 (1991).

[77] Opensource Handbook of Nanoscience and Nanotechnology, Wikibooks, http://en.wikibooks.org/wiki/Microtechnology/Additive_Processes

[78] W.D. Westwood, “Planar Magnetron Sputtering,” *Progress in Surface Science*, 7, (1976) 71.

[79] P.J. Kelly, R.D. Arnell, “Magnetron sputtering: a review of recent developments and applications,” *Vacuum*, 56, (2000) 459-172.

[80] L. F. Thompson, C. G. Willson, and M. J. Bowden, “Introduction to Microlithography,” *American Chemical Society*, Washington, DC, (1983).

[81] W. M. Moreau, “Semiconductor Lithography,” *Plenum Publishing Co.*, New York, (1988).

[82] Hwaiyu Geng, “Semiconductor manufacturing handbook,” *McGraw-Hill*, New York, (2005).

[83] R. N. Singh, A. E. Rosenbluth, G. L.-T. Chiu, and J. S. Wilczynski, “High-numerical-aperture optical designs,” *IBM Journal of Research and Development*, 41, (1997) 39.

[84] G. L.-T. Chiu and J. M. Shaw, “Optical lithography: Introduction,” *IBM Journal of Research and Development*, 41, (1997) 3.

[85] J. S. Wilczynski, "Optical Step and Repeat Camera with Dark Field Automatic Alignment," *J. Vac. Sci. Technol.*, 16**,** (1979) 1929.

[86] M. Rothschild, R. B. Goodman, M. A. Hartney, M. W. Horn, R. R. Kunz, J. H. C. Sedlacek, and D. C. Shaver, "Photolithography at 193 nm," *J. Vac. Sci. Technol. B*, 10**,** (1992) 2989.

[87] M. Hibbs, R. R. Kunz, and M. Rothschild, "193-nm Lithography at MIT Lincoln Lab," *Solid State Technol.*, 38**,** (1995) 69.

[88] Mordechai Rothschild, Mark W. Horn, Craig L. Keast, Roderick R. Kunz, Vladimir Liberman, Susan C. Palmateer, Scott P. Doran, Anthony R. Forte, Russel B. Goodman, Jan H.C. Sedlacek, Raymond S. Uttaro, Dan Corliss, and Andrew Grenville, "Photolithography at 193 nm," *The Lincoln Laboratory Journal*, 10 , (1997) 19.

[89] A. Takanashi, T. Harada, M. Akeyama, Y. Kondo, T. Karosaki, S. Kuniyuoshi, S. Hosaka, and Y. Kawamura, U.S. Patent No. 4,480,910 (1984).

[90] W. Tabarelli and E. W. Lobach, U.S. Patent No. 4,509,852 (1985).

[91] M. Rothschild, T. M. Bloomstein, R. R. Kunz, V. Liberman, M. Switkes, S. T. Palmacci, J. H. C. Sedlacek, and D. Hardy, "Liquid Immersion Lithography: Why, How and When," *J. Vac. Sci. Technol. B*, 22, (2004) 2877.

[92] Yoshio Nishi and Robert Doering, "Handbook of Semiconductor Manufacturing Technology," *Marcel Dekker Inc.*, (2000).

[93] MSDS Sheet in NanoFab, University of Alberta.

[94] Picture courtesy of Melles Griot. *Laser Beam Measurements.* Retrieved March 31, 2003 from the World Wide Web. http://206.135.73.102/tut_beam_prof.asp

[95] C. Germain, Y.Y. Tsui, "Femtosecond laser induced forward transfer of materials," *Proc. Int. Conf. MEMES, NANO and Smart Systems, Banff*, (2003) 44.

[96] S. E. Kirkwood, A.C. van Popta, Y,Y, Tsui and R. Fedosejevs, “Single and multiple shot near-infrared femtosecond laser pulse ablation thresholds of copper,” *Applied Physics A*, 81, (2005) 729 – 735.

[97] P. Papakonstantinou, N.A. Vainos, C. Fotakis, “Microfabrication by UV femtosecond laser ablation of Pt, Cr and indium oxide thin fimls” *Appl. Surf. Sci.*, 151, (1999) 159.

[98] S. E. Kirkwood, “Charcterization of metal and semiconductor Nanomilling at near threshold intensities using femtosecond laser pulses,” University of Alberta PhD thesis (2007)

[99] T.Q. Qiu and C.L. Tien, “Heat transfer mechanisms during short-pulse laser heating of metals,” *Journal of Heat Transfer*, 115, (1993) 835.

[100] A. E. Siegman, “Lasers,” Chapter 17 in 1986 edition published by University Science Books.